

# HYDRODYNAMIC MODELING OF MASSIVE STAR INTERIORS

by

Casey A. Meakin

---

A Dissertation Submitted to the Faculty of the  
DEPARTMENT OF ASTRONOMY  
In Partial Fulfillment of the Requirements  
For the Degree of  
DOCTOR OF PHILOSOPHY  
In the Graduate College  
THE UNIVERSITY OF ARIZONA

2006

THE UNIVERSITY OF ARIZONA  
GRADUATE COLLEGE

As members of the Dissertation Committee, we certify that we have read the  
dissertation

prepared by Casey A. Meakin

entitled Hydrodynamic Modeling of Massive Star Interiors

and recommend that it be accepted as fulfilling the dissertation requirement for the  
Degree of Doctor of Philosophy

\_\_\_\_\_  
David Arnett

Date: November 27, 2006

\_\_\_\_\_  
Donald W. McCarthy

Date: November 27, 2006

\_\_\_\_\_  
Edward W. Olszewski

Date: November 27, 2006

\_\_\_\_\_  
James W. Liebert

Date: November 27, 2006

\_\_\_\_\_  
Philip A. Pinto

Date: November 27, 2006

Final approval and acceptance of this dissertation is contingent upon the candidate's  
submission of the final copies of the dissertation to the Graduate College.

I hereby certify that I have read this dissertation prepared under my direction and  
recommend that it be accepted as fulfilling the dissertation requirement.

\_\_\_\_\_  
Dissertation Director: David Arnett

Date: November 27, 2006

## STATEMENT BY AUTHOR

This dissertation has been submitted in partial fulfillment of requirements for an advanced degree at The University of Arizona and is deposited in the University Library to be made available to borrowers under rules of the Library.

Brief quotations from this dissertation are allowable without special permission, provided that accurate acknowledgment of source is made. Requests for permission for extended quotation from or reproduction of this manuscript in whole or in part may be granted by the head of the major department or the Dean of the Graduate College when in his or her judgment the proposed use of the material is in the interests of scholarship. In all other instances, however, permission must be obtained from the author.

SIGNED: Casey Adam Meakin

## ACKNOWLEDGMENTS

I must thank Peter Strittmatter, director of Steward Observatory, for encouraging me to complete a PhD when I was struck by serious doubts early in my graduate school career. David Arnett is also largely responsible for my decision to stay. His refreshingly original approach to astrophysics is inspiring and he has been a fabulous mentor, making himself very accessible during my three year tutelage. I thank my thesis committee for cajoling from me the self discipline necessary to write up this dissertation, and without whom I may have succumb for too long the reckless abandon of research solely for my own selfish interest. For acquiring the requisite level of professionalism needed to finish I am indebted to Philip Pinto, James Liebert, Don McCarthy, and especially my fellow Windsorian Edward Olszewski. I would also like to thank Adam Burrows for a great deal of informative conversation and ongoing sermons on the art of fastidiousness. I thank the computer support at Steward Observatory, including Jeff Fookson, Neil Lauver, and Alan Koski for keeping the local Beowulf computing clusters, Grendel and Mendeleyev, mostly up and running.

Outside of work, I have enjoyed over the last few years uninhibited banter over many beers with Desika "Nopey" Narayanan, Brandon Kelly, "Genghis Jon" Trump, Aleks Diamon-Stanic, Jared Gabor, R. Shane Bussman, Stephanie Jeneut, Stephanie Cortes, Amy Stutz, Annie Kelly, Maggie Keck, Stephan Herbert-Fort, Ashwin Bijanki, Martin Prescher, Philip Strack, and all of the others who have crowded around the table searching for some meaning beyond the ordinary routine of life. I have also learned many life lessons by brushing up against the exemplary lifestyles of Luke Griffin and Evangelli Envangelopolous. I am grateful for the thoughtful and caring company of Chien Peng during our time of overlap in Arizona, and the other remote destinations we happened to find ourselves together. I feel special gratitude towards my friend and fellow astrophysicist Christian D. Ott whose path I hope to cross more often in the future. I may be guilty of introducing him to the writings of Charles Bukowski, but he alone is responsible for emulating him. "If Charles Bukowski was a scientist." I am also thankful for the company of my academic peers over the years, including Jeremy Bailin, Margaret Turnbull, Amaya Moro-Martin, Christopher Groppi, Eric Mama-jek, Jackie Monkiewicz, Andrea Leistra, Patrick Young, Wilson Liu, Janice Lee. I must also thank Tom and Kelly Silliman, and Carolyn Merritt, without whom my dissertation may have been completed a few years earlier.

I owe too much to list here to Ивелина Момчева for her companionship, and being generally a great friend. Аз обичам те.

## DEDICATION

To the memory of my father,

*Stephen Allen Meakin*  
(1949-1997)

and my grandfather,

*Alfred Marian Marchlewski*  
(1917-1991)

## TABLE OF CONTENTS

LIST OF FIGURES . . . . .	8
LIST OF TABLES . . . . .	16
ABSTRACT . . . . .	17
Chapter 1 INTRODUCTION . . . . .	18
1.1 The Aim and Structure of the Present Work . . . . .	27
Chapter 2 ACTIVE CARBON AND OXYGEN SHELL BURNING . . . . .	32
2.1 Introduction . . . . .	32
2.2 A Double Shell: Active Oxygen and Carbon Burning . . . . .	32
2.3 Results . . . . .	33
2.4 Discussion . . . . .	42
Chapter 3 ANELASTIC AND COMPRESSIBLE MODELS OF OXYGEN BURNING . . . . .	45
3.1 Introduction . . . . .	45
3.2 Model Comparison . . . . .	47
3.2.1 The Initial Models and Simulation Parameters . . . . .	47
3.2.2 Flow Properties: Anelastic Model . . . . .	49
3.2.3 Flow Properties: Compressible Models . . . . .	50
3.3 Conclusions . . . . .	60
Chapter 4 TURBULENT CONVECTION IN STELLAR INTERIORS . . . . .	67
4.1 Introduction . . . . .	67
4.2 Turbulent Entrainment . . . . .	68
4.3 The Numerical Tools . . . . .	71
4.3.1 1D Stellar Evolution . . . . .	71
4.3.2 Multi-Dimensional Reactive Hydrodynamics with PROMPI . . . . .	72
4.4 Oxygen Shell Burning . . . . .	74
4.4.1 The Correct Mixing Boundary . . . . .	77
4.4.2 Time Evolution . . . . .	79
4.4.3 Quasi-Steady Oxygen Shell Burning Convection . . . . .	80
4.4.4 Stable Layer Dynamics During Shell Burning . . . . .	81
4.5 Core Convection . . . . .	83
4.5.1 Quasi-Steady Core Convection . . . . .	86
4.5.2 The Stable Layer Dynamics Overlying the Convective Core . . . . .	88
4.6 Simulations and Mixing Length Theory . . . . .	89
4.6.1 Mixing Length Theory Picture . . . . .	89

4.6.2	The Enthalpy Flux, Background Stratification, and Temperature and Velocity Fluctuations . . . . .	92
4.6.3	Correlation Length Scales . . . . .	96
4.6.4	The Kinetic Energy Flux, Flow Asymmetry, and Moving Beyond the Mixing Length Theory . . . . .	98
4.6.5	Related Studies . . . . .	100
4.7	Mixing At Convective Boundaries . . . . .	102
4.7.1	Quantifying the Boundary Layer Mixing Rates . . . . .	103
4.7.2	The Entrainment Energetics . . . . .	105
4.7.3	Whence $q$ ? . . . . .	109
4.7.4	An “Empirical” Entrainment Law . . . . .	110
4.7.5	A Dynamic Convection Zone Boundary Condition . . . . .	111
4.7.6	Spatial Scales, Numerical Resolution, and Entrainment . . . . .	113
4.8	Summary And Conclusions . . . . .	115
Chapter 5	CONCLUDING REMARKS . . . . .	146
5.1	Related Efforts . . . . .	148
Appendix A	TURBULENT ENERGY EQUATION . . . . .	151
A.1	Total Energy . . . . .	151
A.2	Kinetic Energy . . . . .	152
Appendix B	CORRELATION LENGTH SCALES . . . . .	154
Appendix C	NON-RADIAL WAVE EQUATION . . . . .	156
C.1	Non-Radial Wave Equation . . . . .	156
C.1.1	Dependence on Computational Domain . . . . .	160
C.2	Eigenmode Solutions . . . . .	161
Appendix D	COMPUTATIONAL COSTS . . . . .	162
REFERENCES	. . . . .	164

## LIST OF FIGURES

- 2.1 The  $23M_{\odot}$  TYCHO model used as initial conditions for the hydrodynamic simulation is shown here. (*top*) Density and temperature profiles are shown illustrating the large number of scale heights simulated as well as the complex entropy structure due to the burning shells. (*middle*) The mixing length velocities are shown and delineate the extents of the carbon and oxygen burning convection zones. The dashed vertical lines mark the boundaries of the simulation domain. (*bottom*) The onion skin compositional layering of the model is shown here for the four most abundant species. . . . 34
- 2.2 The magnitude of the flow velocity (*top*) and the net energy generation rate,  $\epsilon_{net} = \epsilon_{nuc} + \epsilon_{\nu}$  (*bottom*), is shown for a snapshot of the simulation which includes both an oxygen and carbon burning convection zone. The carbon burning convective shell extends to a radius of  $\sim 4.5 \times 10^9$  cm while the figure is truncated at a radius of  $\sim 2.9 \times 10^9$  cm for clarity. A weak silicon-burning convection zone develops at the inner edge of the grid due to a small boundary-zone entropy error which accumulates during the course of the calculation. . . . . 37
- 2.3 (*top*) Nonspherical density and temperature perturbations (root mean square fluctuation about the angular mean divided by the angular mean) are shown for the inner  $1.2 \times 10^9$  cm of the simulation domain. (*bottom*) In this propagation diagram (showing oscillation frequency versus stellar radius) the gravity wave and ( $l=4$ ) acoustic wave propagation zones are indicated by the horizontal and cross-hatched shading, respectively. The gravity wave cavity is bounded above by the buoyancy frequency (solid line), while the acoustic cavity is bounded below by the Lamb frequency (dashed line). . . . 38



- 2.4 (*left*) The frequency power spectrum of the  $l=4$  component of the radial velocity ( $v_x$ ) is shown as a function of radius. The dashed horizontal lines indicate the frequencies of two waves with significant power that are compared to linear theory in the adjacent panel. (*right*) Two  $l=4$  wave forms are shown. The wave forms extracted from the simulation data (dotted line) and calculated with linear theory (solid line) are shown for comparison. For each mode the horizontal ( $v_y$ ) and radial velocity ( $v_x$ ) components are presented in units of  $\text{cm s}^{-1}$ . The shaded areas correspond to stably stratified regions. Both of these modes have some p- and g-mode character. The mode in the bottom panel is predominately of g-mode character, while the mode in the top panel is more clearly of mixed type. . . . . 39
- 3.1 Spatial distribution of density fluctuations are shown for (left) a slice through the 3D compressible model and (right) the 2D compressible model. In both models the flow is composed of two distinct regimes, including the convective flow in the center which is bounded above and below by stably stratified layers which are host to internal waves. The scale on the 2D model has been truncated to same limits as the 3D model for comparison, but extreme values exceed the scale limits by a factor of  $\sim 2$ . The 3D model has been tiled twice in angle for clarity. . . . . 50
- 3.2 (left) Density fluctuations for 3D compressible model: The time average of the maximum density fluctuation is shown as the thick line, with the extreme values for the averaging period (two convective turnovers) shown as the shaded region. Within the body of the convection zone the average fluctuations are quite low  $\sim 0.25\%$ . The largest fluctuation (the spike at  $r \approx 0.43 \times 10^9 \text{ cm}$ ) is  $\sim 11\%$  (exceeding the plot limits), while the secondary maximum ( $r \approx 0.85 \times 10^9 \text{ cm}$ ) reaches  $\sim 3.5\%$ . These fluctuations occur in the radiative regions that enclose the convection zone (outside the computational domain of Kuhlen, Woosley, & Glatzmaier (2003)). (right) Mach number for the 3D compressible model: shown is the instantaneous value of the maximum Mach number at a given radius (thick line), and the rms Mach number (thin line). . . . . 52

- 3.3 (left) Pressure fluctuations in 3D compressible model: The time averaged horizontal RMS pressure fluctuations are shown as the thick line, with the envelope of extreme values over two convective turnovers indicated by the shaded region. The radial ram pressure of the turbulent convection,  $\rho v_r^2$ , is shown as the thin line. The curves cross at the convective boundaries where the turbulent pressure is balance by the pressure fluctuation induced by internal waves in the adjoining stably stratified layers. (right) The magnitude of the buoyancy frequency is shown in units of rad/s. Also shown by the dashed line is the buoyancy frequency normalized by the gravity which, through Equation 3.6, sets the scale of the density fluctuations at the convective boundaries (compare with Figure 3.2(left)). . . . . 57
- 3.4 (top) Entropy profile of 3D compressible model. (bottom) Entropy fluctuations for 3D compressible model: The two solid lines indicate the maximum and minimum fluctuation for a given radius over the course of two convective turnovers. The annotations indicate fluctuations due to low entropy material entrained at the lower boundary and high entropy material entrained at the upper boundary. . . . . 64
- 3.5 Spatial distribution of the oxygen mass fraction is shown for (left panels) the 3D compressible model and (right panels) the 2D compressible model. The spatial distribution is shown in the top row, and the time averaged RMS horizontal fluctuations are shown in the bottom row with the shaded region indicating extreme values of the fluctuations over two convective turnovers. . . . . 65
- 4.1 Diagram illustrating the salient features of the density and velocity field for the turbulent entrainment problem. Three layers are present: a turbulent convection zone is separated from an overlying stably stratified region by a boundary layer of thickness  $h$  and buoyancy jump  $\Delta b \sim N^2 h$ . The turbulence near the interface is characterized by integral scale and RMS velocity  $\mathcal{L}_H$  and  $\sigma_H$ , respectively. The stably stratified layer with buoyancy frequency  $N(r)$  propagates internal waves which are excited by the adjacent turbulence. A shear velocity field  $v_\perp(r)$ , associated with differential rotation, may also be present. After Strang & Fernando (2001). 118
- 4.2 Radial profile of the simulated region for the oxygen shell burning models. The thin lines indicate the initial conditions and the thick lines indicate the 3D model at  $t = 400$  s. (top left) Temperature and density. (top right) Mass fraction of  $^{16}\text{O}$ . (bottom left) Squared buoyancy frequency. (bottom right) Buoyancy. . . . . 119

- 4.3 This time sequence shows the onset of convection in the oxygen shell burning model. The first 200 s of the 2D model (ob.2d.c) is shown, including the initial transient and the settling down to a new quasi-steady state. The light yellow line indicates the location of the convective boundary as defined in the 1D TYCHO stellar evolution model (Ledoux criterion), which was used as initial conditions for the simulation. . . . . 120
- 4.4 The time evolution of the 3D oxygen shell burning model. (top) The magnitude of the oxygen abundance gradient is shown and illustrates the migration of the convective boundaries into the surrounding stable layers. Interfacial oscillations are also apparent in the upper convective boundary layer ( $r \sim 0.85 \times 10^9$  cm), and internal wave motions can be seen quite clearly in the upper stable layer. (bottom) The kinetic energy density is shown, and illustrates the intermittent nature of the convective motions. The upwelling chimney-like features in the convective region are seen to excite internal wave trains in the stable layers, which propagate away from the boundaries of the convection zones. See also Fig. 4.25. . . . . 121
- 4.5 The time evolution of the energy budgets for the oxygen shell burning models: the (thick line) 3D model, and (thin lines) the three 2D models are shown, including: (thin-solid) ob.2d.c; (thin-dashed) ob.2d.e; and (thin dotted) ob.2d.C. The energy budget includes the internal energy  $E_I$ , the gravitational energy  $E_G$ , and the kinetic energy  $E_K$ . Note that the energy scale is logarithmic, so that the 3D kinetic energy is much smaller than the 2D values. . . . . 122
- 4.6 The r.m.s. velocity fluctuations for oxygen shell burning: (left) 3D model, with velocity components (thick-solid)  $v_r$ , (thin-solid)  $v_\theta$ , and (thin-dashed)  $v_\phi$ . (right) The 2D models, with velocity components (thick)  $v_r$  and (thin)  $v_\phi$  for simulations (solid) ob.2d.e, (dashed) ob.2d.c, and (dash-dot) ob.2d.C. . . . . 123
- 4.7 Mode diagrams for several radial positions in the oxygen shell burning model show the dominant spatial and time scales on which motions occur. The abscissa measures  $k$  which is related to the wavenumber index  $l$  of the mode by  $l = 12 \times k$ . The three locations shown here include: (left) Lower stable layer, just beneath the convective shell  $r = 0.4 \times 10^9$  cm. (middle) Middle of convective shell,  $r = 0.6 \times 10^9$ . (right) Upper stable layer, just above the convective shell  $r = 0.9 \times 10^9$  cm. . . . . 123

- 4.8 Radial profile of the simulated region for the main sequence core convection model. The thin lines show the initial conditions and the thick lines show the state of the 3D model at  $t = 10^6$  s. (top left) Temperature and density. (top right) Hydrogen abundance. (bottom left) Squared buoyancy frequency. (bottom right) Buoyancy. 124
- 4.9 Velocity isocontours show the development of the flow in the 3D core convection model. The turbulent convective flow excites internal waves which radiate into the overlying stably stratified layer. By the end of the time sequence shown the stable layer cavity is filled with resonant modes. . . . . 125
- 4.10 The velocity magnitude for the core convection model at  $t=10^6$  s: (left) a slice through the 3D model; and (right) the 2D model. The topology of the convective flow is significantly different between 2D and 3D models: the 3D convective flow is dominated by small plumes and eddies while the 2D flow is much more laminar, and dominated by a large vortical eddies which span the depth of the layer. The wave motions in the stable layer have similar morphology in 2D and 3D, but the velocity amplitudes are much larger in 2D. The computational domains have been tiled once in angle for presentation. . . . . 125
- 4.11 The time evolution of the energy budget for the main sequence core convection models: the (thick line) 3D model; and (thin line) the 2D model are shown. The energy budget includes the total internal energy  $E_I$ , gravitational energy  $E_G$ , and kinetic energy  $E_K$  on the computational grid. . . . . 126
- 4.12 The r.m.s. velocity fluctuations for the core convection model: (left) the 3D model, and (right) the 2D model. In each plot, the thick line indicates the radial velocity component and thin line is used to indicate horizontal velocity components, with the dashed line used to show the polar angle component in the 3D model. . . . . 127
- 4.13 Pressure fluctuations in core convection model: The time averaged horizontal r.m.s. pressure fluctuations are shown as the thick line, with extreme values over two convective turnovers indicated by the shaded region. The thin line shows the radial component of the turbulent ram pressure  $\rho v_r^2$  averaged over a convective turnover. At the upper boundary, the curves cross at a point where the turbulent pressure is balanced by the wave induced pressure fluctuations in the stable layer. This crossing point is coincident with the location of the convective boundary. The pressure perturbations at the lower boundary are due to the input luminosity which drives the convective flow. . . . . 128

- 4.14 (left) Density fluctuations in the 3D core convection model: The time averaged maximum density fluctuation is shown as the thick line, with extreme values for the averaging period (two convective turnovers) shown by the shaded region. The largest fluctuations occur at the interface between the turbulent convective region and the stably stratified layer. The maximum fluctuation at the interface is  $\rho'/\langle\rho\rangle \sim 0.12\%$ . (right) The buoyancy frequency is shown in units of ( $10^{-4}$  rad/sec). Also shown by the dashed line is the buoyancy frequency normalized by the gravity which sets the scale of the density fluctuations at the convective boundary through equation 4.13. The expected density fluctuation is  $\rho'/\langle\rho\rangle \sim v_c|N|/g \sim 0.12\%$ , where a velocity scale of  $v_c \sim 2 \times 10^5$  cm/s has been used (see Figure 4.12). . . . . 129
- 4.15 (left) Convective enthalpy flux,  $F_c = \langle \rho c_p v_r T' \rangle$ . (right) Temperature-velocity correlation function  $\alpha_E$  calculated according to equation 4.21, with mean value  $\langle \alpha_E \rangle = 0.7$  shown by the dashed line. . . . . 130
- 4.16 (left) Dimensionless temperature gradients: the stellar interior  $\nabla_s$ ; adiabatic  $\nabla_{ad}$ ; and Ledoux  $\nabla_{led}$  gradients are shown. (right) Super-adiabatic temperature gradient horizontally and time averaged. . . . . 130
- 4.17 (left) Time averaged r.m.s. temperature fluctuations: (thick solid) line shows the r.m.s. fluctuations; the (thin solid) and (thin dotted) lines show the fluctuations in the upward and downward directed flow components, respectively. (right) The radial dependence of the "thermal mixing length" parameters  $\alpha_T$  defined by equation 4.22 are shown the temperature fluctuations presented in the left panel, using the same line types. The mean values, averaged over  $r \in [0.5, 0.75] \times 10^9$  cm are shown by the thin dotted lines. . . . . 131
- 4.18 (left) Radial velocity amplitudes: (thick solid) r.m.s. value; the (thin solid) and (thin dashed) show the mean up- and down-flow velocities, respectively. (right) The radial dependance of the "velocity mixing length" parameters  $\alpha_v$  defined by equation 4.23 are shown for the velocity amplitudes presented in the left panel, using the same line types. The mean values, averaged over  $r \in [0.5, 0.75] \times 10^9$  cm are shown by the thin dotted lines. . . . . 132

- 4.19 The vertical correlation length scales  $L_V$  as defined in §B. (top left)  $L_V$  for velocity fluctuations,  $v'_r$ ; (top right)  $L_V$  for temperature fluctuations,  $T'$ . The pressure scale height  $H_p$  and density scale height  $H_\rho$  are shown for comparison. (bottom left) Illustration of the relationship between eddy shape and the correlation length scales,  $L_V^+$  and  $L_V^-$ . The grey patches represent the shapes of the eddies and the  $L_V^{+/-}$  values are measured in the radial direction, away from the horizontal line. (bottom right) Correlations lengths  $L_V$  scaled to pressure and density scale heights, e.g.,  $\alpha_V(v_r, H_p) = L_V(v_r)/H_p$  133
- 4.20 The horizontal and vertical correlation length scales,  $L_H$  (thick line) and  $L_V$  (thin line) are shown for temperature (dashed) and velocity (solid) fluctuations. . . . . 134
- 4.21 The fractional area occupied by the upward flowing material  $f_u$  is shown as a function of radial position. The downward flowing area is  $f_d = (1 - f_u)$  and the dashed line at 1/2 indicates up-down symmetry. . . . . 135
- 4.22 (left) Kinetic energy flux: (thick) line shows the value measured in the simulation averaged over two convective turnovers; the (thin solid) line shows  $F_K$  calculated according to equation 4.26; the (thin dashed) line shows  $F_K$  calculated according to equation 4.26 but uses  $c\langle v \rangle^3$  in place of  $\langle v^3 \rangle$ , and a correlation constant of  $c = 5$ . (right) Asymmetries in radial velocity: the (thick) line show the skewness in the velocity field,  $\gamma = \langle v^3 \rangle / \sigma_v^3$ ; the (thin solid) and (thin dashed) lines show the correlations  $\chi = \langle v^3 \rangle / \langle v \rangle^3$  where the subscripts  $u$  and  $d$  indicate up- and down-flows, respectively. . . . . 136
- 4.23 Equatorial slices showing the flow in the vicinity of the convective boundaries in the 3D simulations, ordered by relative stability: (row a) upper shell convection boundary,  $Ri_B \sim 36$ ; (row b) core convection boundary,  $Ri_B \sim 48$ ; (row c) lower shell convection boundary,  $Ri_B \sim 419$ . The colormap indicates composition abundance, where the darker tones trace stable layer material entrained across the interface. The velocity vectors have been sampled every third zone in each dimension. . . . . 137

- 4.24 The time history of (top row) the convective boundary location, and (bottom row) the thickness of the convective interface for: (left) upper shell burning boundary; (middle) lower shell burning boundary; and (right) core convection boundary. The (thick line) identifies the 3D models, ob.3d.B and msc.3d.B; and the (thin line) identifies the 2D models, ob.2d.e and msc.2d.b. The (dashed lines) show the averaged interface thickness for  $t > 300$  s for oxygen burning, and  $t > 6.0 \times 10^5$  s for core convection. The letters (a-c) in the upper left panel mark times when the outward migration rate of the convective boundary rapidly adjusts to a new value in the 3D model. . . . . 138
- 4.25 Buoyancy flux. Time-series diagrams and time-averaged radial profiles are shown for: (top-row) the 3D oxygen shell burning model; and (bottom-row) the 3D core convection model. . . . . 139
- 4.26 Normalized entrainment rate plotted against bulk Richardson number  $Ri_B$ . The 3D models are marked with squares, and the 2D data by plus signs. The best fit power-law to the 3D model data is shown by the dashed line. The 2D entrainment rates fall everywhere below the 3D trend. The arrow indicates the direction in the diagram that the 2D data points would move if the effective r.m.s. turbulence velocity were lower. . . . . 140
- 5.1 Presupernova silicon burning hydrodynamics: (left) The radial dependence of the convective velocity is shown as a function of time for a one-dimensional  $23 M_{\odot}$  stellar model as it approaches core collapse, which commences at the very end of the time-sequence shown. The innermost convection zone is due to silicon burning, and a transition from core to shell burning can be seen. The overlying convection zones are driven by oxygen, neon, and carbon burning shells. This model was evolved with the TYCHO stellar evolution code. (right) This snapshot shows the distribution of  $^{28}\text{Si}$  and net energy generation for a two dimensional hydrodynamic simulation of the TYCHO model  $\sim 1000$  s before core collapse. Silicon, oxygen, neon, and carbon are burning in concentric shells progressively further away from the iron-rich core which will soon undergo gravitational collapse. The outer boundary of the oxygen burning convection zone is strongly perturbed by the convective motions which eventually mixes the carbon, neon and oxygen burning shells together prior to core collapse. . . . . 150

## LIST OF TABLES

2.1	Model Parameters . . . . .	35
3.1	Comparison of Oxygen Burning Models . . . . .	66
4.1	Nuclei Included in Reduced Nuclear Reaction Network . . . . .	141
4.2	Summary of Oxygen Shell Burning Models . . . . .	142
4.3	Summary of "Core Convection" Models . . . . .	142
4.4	Assumed and Measured Convection Parameters <sup>a</sup> . . . . .	143
4.5	Convective Boundary Layer Properties For Oxygen Shell Burning Models . . . . .	144
4.6	Convective Boundary Layer Properties For "Core Convection" Mod- els . . . . .	145



## ABSTRACT

In this thesis, the hydrodynamics of massive star interiors are explored. Our primary theoretical tool is multi-dimensional hydrodynamic simulation using realistic initial conditions calculated with the one-dimensional stellar evolution code, TYCHO. The convective shells accompanying oxygen and carbon burning are examined, including models with single as well as multiple, simultaneously burning shells. A convective core during hydrogen burning is also studied in order to test the generality of the flow characteristics. Two and three dimensional models are calculated. We analyze the properties of turbulent convection, the generation of internal waves in stably stratified layers, and the rate and character of compositional mixing at convective boundaries.

## CHAPTER 1

### INTRODUCTION

*Thus the whole computing job we are contemplating turns out to be of such a magnitude that, in spite of the speed and capacity of modern computers, I know of no institution which could and would assign the necessary computer time to such an undertaking. No, I feel we are once again forced to try to think.*

Martin Schwarzschild (1969)<sup>1</sup>

Fields as diverse as stellar population synthesis modeling, galactic chemical evolution, star formation, and even cosmology (via the stellar and supernova distance ladder) all rely critically on our knowledge of how an individual star lives and dies. Therefore astronomers are faced with the question: how well can we model an individual star? Arriving at a satisfactory answer to this question is not a trivial exercise.

The basic ingredients that go into a stellar model are of two distinct types, including microphysical properties of the stellar plasma and a macroscopic fluid dynamics problem. The microphysics needed include radiative opacities; thermodynamic properties, including the equation of state; and nuclear reaction rates. These microphysical properties are then used as inputs to close the reactive-, radiation-, magneto-, hydrodynamics problem which describes the overall stellar structure and its time evolution. So, how well can we solve this problem? To first order, the theory of stellar evolution is a success: the basic properties of

---

<sup>1</sup>George Darwin Lecture, Royal Astronomical Society, published in the *Quarterly Journal of the Royal Astronomical Society* (1970) 11, 12-22.

stars, including the radii and luminosities can be fairly well characterized, including the time evolution of the star's structure as it moves through a variety of distinct phases driven by radiation and mass loss at the surface, interior mixing processes, and nuclear transmutation of composition.

Despite this success, the limitations in stellar theory are well known. Almost every ingredient that goes into a stellar model is subject to some level of uncertainty. For example, important nuclear reaction links, including the  $C^{12}(\alpha, \gamma)^{16}O$  link which determines the composition of stellar cores following helium burning and subsequent stages, are subject to considerable uncertainty due to the difficulty involved in both measuring the rates in the laboratory, and calculating them theoretically (see e.g. Kunz et al., 2002; Arnett & Thielemann, 1985; Thielemann & Arnett, 1985). The macrophysical problem is also the source of considerable uncertainty. For instance, the magneto- part of the problem is almost always ignored, and the hydrodynamic part of the problem has been so emasculated that any respectable fluid mechanic would recognize it as a back of the envelope calculation. Regardless of the simplifications made to the hydrodynamics, stellar models are still very complex systems with a large number of physical processes acting simultaneously with various types of feedback. Although only one-dimensional, the computational challenge is complicated by the necessity of an implicit solution method.

That the treatment of hydrodynamics in stellar evolution models is one of the primary weaknesses of the theory is related to the history of the field, which during its inception was limited by computational power. The earliest numerical models described stars as static spheres (essentially polytropes)<sup>2</sup>. Thrown

---

<sup>2</sup>An informal account of the early history of stellar structure by Martin Schwarzschild, including the contributions made by his uncle Robert Emden and his father Karl, is published in *The Astrophysical Journal* (1961), 134, 1.

out with the time evolution and multi-dimensionality were the non-radial modes of motion, except for convection which was initially treated in a highly simplified manner by assuming that convectively unstable regions obtain an adiabatic temperature gradient. The increased availability of calculating machines eventually led to numerical models defined on a radial grid that could evolve in time, although initially quasi-statically. This remains essentially the standard concerning the treatment of stellar hydrodynamics today (Kippenhahn & Weigert, 1990; Hansen & Kawaler, 1994).

What has been excised for practical purposes early in the history of the theory is a complex hydrodynamic flow which is superimposed over the background hydrostatic structure of the star. This neglected flow is hydrodynamically very rich, consisting of wave motions, turbulent convection, differential rotation, and large scale rotationally induced currents. The consequences of these hydrodynamic motions are not well understood, but based on experiences with similar flows in the laboratory and geophysics they are known to be capable of producing long-range transport of angular momentum and stellar matter (i.e., composition mixing).

The deficiencies in stellar modeling are resurfacing in light of increased observational scrutiny, and astronomers are now asking more of stellar evolution than first order answers. A few developments of recent interest include:

- *The Sun*. The radial profile of sound speed within the Sun, inferred by helioseismic inversion studies, reveal discrepancies with standard solar models at regions just beneath the convection zone (Bahcall et al., 2006) when new chemical abundances are used (Asplund et al., 2005). This region is known to be hydrodynamically active due to the presence of a shear layer called the *tachocline* as well convective overshooting. A related, unsolved conundrum

is the nearly solid body rotation of the core, also inferred from helioseismology data (Basu, 1997).

- *Surface abundance “anomalies” across the HR diagram.* Lithium and CNO abundances within the “Lithium dip”; He and N enrichment in massive O stars (see, e.g. Charbonnel & Talon, 1999; Pasquini et al., 2004); and the products of s-process nucleosynthesis (see, e.g. Lattanzio & Lugaro, 2005) all show discrepancies with standard stellar evolution models.
- *Wide eclipsing binaries.* The properties of stars in wide-eclipsing binary systems provide another direct observational probe of individual star evolution. If ages and metallicities can be constrained, these systems provide laboratories in which high precision stellar measurements can be made. Fundamental properties, including the radii and masses, are found to be in disagreement with theoretical models. For instance, theoretical radii for low mass stars ( $0.4 - 0.8 M_{\odot}$ ) are found to be 5 - 15% lower than observed (Ribas, 2006). With observational errors on the order of only a few percent, these are rigorous constraints for evolutionary models.

A variety of solutions have been proposed to these conundrums, which can be succinctly summarized as: the discrepancies between theory and observation can be resolved by adjusting the treatment of convection, and *increasing the amount of mixing that takes place beyond the edges of currently defined convective regions*. The degree of extra mixing required can almost certainly be accommodated by the hydrodynamic processes which are neglected.

The approach most often used to describe stellar mixing beyond the formal convective boundaries is to treat it as a diffusive process, with the mass fraction of species  $i$ , written  $X_i$ , evolved in the Lagrangian frame according to,

$$\frac{dX_i}{dt} = \left(\frac{\partial X_i}{\partial t}\right)_{nuc} + \frac{\partial}{\partial m_r} \left[ \hat{D} \frac{\partial X_i}{\partial m_r} \right]. \quad (1.1)$$

The terms on the right include composition changes due to nuclear burning and diffusive mixing. The physical model of mixing is then encapsulated in the Lagrangian diffusion coefficient,  $\hat{D} = (\partial m_r / \partial r)^2 D$ . The Eulerian diffusivity  $D$  is frequently taken to be the product of a velocity and length scale  $D \sim vl$ , or the ratio of a length scale squared and a timescale  $D \sim l^2/\tau$ . Here, the physics of mixing is encapsulated in the calculations of the length, time, and velocity scales. This analysis is almost exclusively based on order of magnitude estimates employing linear instability theory. Examples of mixing processes treated as diffusion include convective overshooting (Herwig et al., 1997)<sup>3</sup>, semiconvective mixing (Langer et al., 1983; Spruit, 1992), rotational instabilities (e.g. Pinsonneault et al., 1989), and gravity wave induced mixing (Press, 1981; García López & Spruit, 1991; Montalban, 1994; Denissenkov & Tout, 2003; Young et al., 2003).

Within convection zones, mixing is usually treated as instantaneous. During the late burning stages, however, the reduced nuclear exhaustion timescales can approach the convective turnover time, and a time-dependent treatment is needed (e.g. Woosley et al., 2002). Diffusive mixing is used, with a diffusivity based on the mixing length velocity and length scale  $D \sim v_c \Lambda$ , where  $\Lambda = \alpha H_P$  is the mixing length in terms of the pressure scale height  $H_P$ .

The use of a diffusive description for these "mixing" processes has been motivated mostly by a lack of understanding and the simplicity with which it can be implemented into existing stellar evolution codes, rather than a belief that it is the correct description of the process. In fact, based on geophysical analogs, it is known that hydrodynamic processes operating in a stellar interior can behave

---

<sup>3</sup>This is the one of the few examples of work which uses a fully nonlinear hydrodynamic model to calibrate the diffusion coefficient, rather than a linear model for mixing.

very differently than diffusion. In some cases, “anti-diffusive” behavior can occur where gradients are steepened rather than smeared out; and in other cases long distance transport processes can operate, such as internal wave transport of angular momentum (Dunkerton & Fritts, 1984). In chapter 4 I present another example of a mixing process which is not well described as diffusion: it is called turbulent entrainment, and although it is a well studied mixing processes in the geophysics and fluid mechanics literature, it has to date not been incorporated into stellar evolution modeling.

The mechanisms which drive stellar mixing are in general inherently non-linear, which means that their behavior is not readily derivable from the basic equations of motion. Some attempts have been made to incorporate non-linear turbulence models into stellar evolution codes (Grossman et al., 1993; Canuto & Dubovikov, 1998). These models, however, require closure assumptions that depend on characteristics of the flow that are not yet well understood. Furthermore, some commonly used closure assumptions, such as the down-gradient approximation (Kuhfuss, 1986), have been shown irrelevant for large regions of a stellar convection zone (Chan & Sofia, 1996). A formal analysis of the governing equations is therefore limited, and carefully designed numerical or laboratory experiments are needed. The past twenty years has seen tremendous growth in the accessibility of computing power, and numerical simulation is playing an ever more central role in our understanding of turbulent flow.

One of the most important, general results that has emerged from simulation work is a basic characterization of the different modes of motion which the stellar plasma can assume. Broadly, the following three types of motion occur: (1) In convectively unstable regions, which generally have large Rayleigh and Reynolds

numbers<sup>4</sup>, the flow obtains a highly turbulent state. (2) The boundaries of convection zones are highly dynamic. They host interfacial waves and instabilities which mediate the motions within the convectively unstable and stable layers. (3) The stably stratified layers are found to be dynamically active, and dominated by internal wave motions incited by the adjacent turbulent layers. Each region is a complex problem in itself, but equally important is how these different regions interact.

A variety of numerical simulations have studied the basic properties of the turbulent convective flow (e.g. Chan & Sofia, 1989, 1996; Kim et al., 1995, 1996; Cattaneo et al., 1991; Porter & Woodward, 2000; Porter, Woodward, & Jacobs, 2000; Robinson et al., 2003, 2004), and have additionally confronted these simulations with the mixing length theory of convection<sup>5</sup>. The results show that significant non-local (i.e., long distance) effects are important which mixing length theory fails to describe, and that mixing length scalings break down significantly near convective boundaries. In addition, the mixing length theory in inefficient convective<sup>6</sup> regions is found to be replete with inconsistencies. Despite these set-

---

<sup>4</sup>The Reynolds number is a dimensionless measure of the relative strength of inertial to viscous forces in a fluid flow. A transition from laminar to turbulent flow occurs as the relative importance of inertial forces surpasses a certain threshold, characterized by a critical Reynolds number (of order a thousand). The Rayleigh number is a dimensionless number associated with the heat transfer in a fluid system, and is formulated in terms of the timescales for buoyancy acceleration, and thermal and momentum diffusion. The Rayleigh number is an indicator of the mode of heat transport through a fluid system. Thermal conduction operates at low values, and a transition to laminar convective flow occurs once a critical value is reached. Increases in the Rayleigh number significantly above the critical value needed to initiate convective motions eventually leads to a transition to turbulence.

<sup>5</sup>The mixing length theory (MLT) is the standard treatment of convection in stellar evolution models. It is a heuristic model of convection which is based entirely on "local" properties of the stellar background. In addition to a variety of assumptions about the character of the flow, it includes only one parameter called the mixing length which represents the distance over which convective "eddies" remain coherent. MLT is described in more detail in §4.6.

<sup>6</sup>Efficient convection means that the energy lost by large eddies over the time it takes them to traverse the unstable region is small. Convection in optically thin atmospheres is often inefficient due to substantial radiative losses during a convective turnover time.



backs for using mixing length theory, a few robust features of the flow were newly discovered, including an up/down flow asymmetry linked to coherent “plume” structures which span the depth of the convection zones, even over multiple pressure scale heights. These coherent structures which form in the turbulent flow are an example of how order can emerge within a seemingly chaotic non-linear system. The benefit of having identified these flow features is that they provide useful guidance for constructing turbulence closure models. These flow features also shed light on the nature of the non-negligible kinetic energy flux which accompanies the convection and which has heretofore been ignored in the mixing length theory of convection.

Concerning convective boundary layers, a variety of idealized simulations have been studied to assess the degree to which “overshooting” occurs (Hurlburt, Toomre, & Massaguer, 1996; Brummell, Clune, & Toomre, 2002; Rogers & Glatzmaier, 2005). These simulations reveal that a convective boundary is best described as an active, transition region of finite width that separates the turbulence from the stably stratified, “radiative-layers”. Distilling this information for use in a one-dimensional stellar model is still in its infancy. Most emphasis has been placed on extracting a single number to quantify the “overshoot” distance beyond a formal convective boundary to which mixing will occur. A few models have started to study convective boundaries under more realistic stellar interiors conditions, including oxygen shell burning (Arnett, 1994; Bazan & Arnett, 1998; Asida & Arnett, 2000); A-star and white dwarf convection (Freytag, Ludwig, & Steffan, 1996); the base of the solar convection zone (Rogers & Glatzmaier, 2006); the core He-flash (Dearborn et al., 2006a); and He-shell burning (Herwig et al., 2006). To date, the most sophisticated application of these multi-dimensional results to one-dimensional stellar evolution is probably that of Herwig et al. (1997),

who parameterized the kinetic energy profiles found in the stable layers outside of the convection zones simulated by Freytag, Ludwig, & Steffan (1996). A diffusive mixing coefficient was then calculated using this stable layer velocity profile, and progress was made in elucidating some of the features of the s-process nucleosynthesis.

Finally, stable layer dynamics have been gaining increasingly more attention. In all of the numerical simulations of penetrative convection mentioned, internal waves were excited in the stably stratified layers<sup>7</sup>. The importance of internal waves is that they can drive transport processes in stable layers, including both angular momentum transport and compositional mixing. That mixing occurs in stably stratified layers is implied by several observational tests, including those mentioned previously. As an example, the rotational state of the radiative solar interior appears to require “nonstandard” mixing. A proposed solution is angular momentum transport by internal waves in the stable layers which are excited by the overlying turbulent convection zone (Kumar et al., 1999).

Obtaining a comprehensive theory of stellar hydrodynamics, which is tantamount to a complete understanding of stratified turbulent flows, is a distant goal. Strides can be made, however, by studying the flows in numerical experiments and analogs in the geophysics literature, and confronting stellar models with ever more stringent observational constraints. This knowledge is particularly relevant to the progenitors of supernovae, for which a *predictive stellar evolution model is needed*. This is so, because the advanced burning stages in massive stars are essentially unobservable. Once carbon core burning commences, the highly energetic burning that takes place in and around the core does not produce an observable effect at the stellar surface: instead, the surface luminosity of the star is domi-

---

<sup>7</sup>By stably stratified layers I refer to those layers which are linearly stable to convective instability.

nated by the hydrogen and helium burning shells, because the energy released by the heavy ion reactions in the deep core is radiated away locally by neutrino emissions (Arnett, 1996). The observational challenge is exacerbated by the significantly accelerated evolution that takes place during the late burning stages due to the small available binding energies in the fuel and the copious neutrino emissions. Therefore, apart from observing the neutrino emissions directly (see e.g. Odrzywolek et al., 2004), these phases of evolution are effectively invisible to astronomers on Earth.

The important role that supernovae play in cosmic evolution warrants a better understanding of their physics.

### 1.1 The Aim and Structure of the Present Work

In this thesis I describe research which is part of a larger effort motivated by David Arnett that strives to develop the next generation of stellar models. Improved progenitor models, which are the inputs to supernovae and nucleosynthetic yield calculations, are a primary goal. The approach is to develop a comprehensive enough understanding of multi-dimensional stellar hydrodynamics through simulation to be able to accurately “project” this physics into a one-dimensional prescription. The “1D prescription” would allow us to accurately predict the modes of hydrodynamic motions which are active including their attendant transport processes, given a one-dimensional stellar profile. In many ways, this work is of an exploratory nature given our current understanding of the hydrodynamics involved.

The primary tools for this work include the one-dimensional stellar evolution code TYCHO (Young & Arnett, 2005), and the PROMPI code which I have developed to perform multi-dimensional hydrodynamic simulations of stellar in-

teriors on parallel computing platforms. The TYCHO code is used both to test one-dimensional hydrodynamic prescriptions informed by simulation, as well as providing initial models for the simulations. Therefore, the research process is fundamentally iterative.

Multi-dimensional hydrodynamics are studied with the PROMPI code, which is based on the PROMETHEUS code, a direct Eulerian implementation of the piecewise parabolic method of Colella & Woodward (1984) generalized to include a multi-component fluid which uses a Riemann solver capable of non-ideal gases (Colella & Glaz, 1985). Parallelism has been implemented through domain decomposition using the MPI libraries for message passing. In addition to restructuring the code for parallel processing, additional microphysics is implemented as well as general subroutines to treat nuclear burning and radiative transport. The microphysics has been ported directly from the TYCHO code, including components of the equation of state and the opacities tables from the OPAL project, to effect easier comparison between these theoretical tools. Radiative transfer has been included in the diffusion limit, using both an implicit (Crank-Nicholson) and explicit solver. Nuclear burning is incorporated using the same subroutines as in the TYCHO code, and allows for an arbitrary reaction network to be assembled using the rate libraries of Rauscher & Thielemann (2000). Additional details are provided in subsequent chapters where relevant.

With the ability to compute on multi-processor platforms, I have been able to extend prior simulations of stellar interiors by our group (Arnett, 1994; Bazan & Arnett, 1998; Asida & Arnett, 2000) to larger computational domains (e.g., multiple burning shells) and three-dimensional flow<sup>8</sup>. In addition to extending the oxygen shell burning models, I have extended our modeling efforts to include

---

<sup>8</sup>Some comments regarding the computational costs involved are provided in §D.

both earlier (main sequence core convection) and later (silicon burning) evolutionary stages.

In chapter 2, I present a hydrodynamic model of a supernova progenitor that is actively burning hydrogen, helium, carbon, and oxygen in concentric shells. The simulation grid encompasses both the carbon and oxygen burning shells, making this the first simulation (that I know of) to model multiple convective burning shells. The most prominent new result attributable to these simulations is the strong influence that resonant internal waves, trapped between the oxygen and carbon burning convection zones, have on the carbon burning shell. These internal wave modes are found to be well described by the linearized wave equation, which I show through a direct comparison of eigenmode solutions to the wave equation and the full non-linear simulation data. This result provides not only support for using linear wave theory in future analysis, but also provides a validation test for the hydrodynamics code. This validation test is particularly interesting because the Mach numbers of the wave motions underlying the resonant modes are very low  $M < 10^{-3}$ , a regime in which compressible codes have recently been challenged (which is discussed further in chapter 3). In connection with supernova physics, I point out that large asphericities are expected at core collapse which are due to the wave motions at convective boundaries, and not due directly to perturbations in the convection zone. This seems to be a common misconception among supernova modelers who often seed instabilities in progenitor models with some form of random perturbations *in the depths of the convection zones* rather than as *low-order modes in the adjacent stable layers*. Additionally, I discuss in this chapter the role that waves play in mediating composition mixing at convective boundaries. In particular, I discuss a process whereby trapped internal waves grow to non-linear amplitudes and are followed

by a breakdown to turbulence through an advection instability: a mechanism first implicated in the deepening of the ocean's thermocline by Phillips (1966) and Orlanski & Bryan (1969), and later applied to atmospheric inversion layers by Pellacani & Lupini (1975). I conclude with some preliminary remarks on the differences seen in the 2D and 3D models. The velocity scales in 2D are greatly exaggerated due to the artificially imposed geometry of the flow.

In chapter 3 I compare our fully compressible 2D and 3D models of oxygen shell burning convection to the 3D anelastic model of Kuhlen, Woosley, & Glatzmaier (2003). I show that the solutions are in very good agreement in the convectively unstable region, and that differences between the models can be explained by physics which was not included in the simpler anelastic model. The deficiencies in the anelastic model include using hard boundaries within the convection zone instead of bounding stable layers, the use of only a single-component fluid, and a restriction to zero mean background expansion. The good agreement between the models of the statistical properties of the convective flow, however, lends additional support to the use of our fully compressible solver for the low Mach numbers simulated since the anelastic model is designed to perform well in these regimes. An important analytic tool developed in this chapter allows us to accurately calculate the amplitudes of the internal wave motions directly from the one-dimensional models profile.

Chapter 4 provides a more extensive overview of the simulations performed, and provides a broad range of diagnostics characterizing the resultant flows. An extensive comparison with mixing length theory is made for the 3D oxygen shell burning model, which is our most physically complete system. Although reasonable agreement is found between the mixing length theory assumptions and the velocity and super-adiabatic temperature gradient in the model, the univer-

salinity of this mixing length is dubious, which comes to light when comparing our results to related studies. One of the more interesting and novel results presented in this chapter concerns the rate and process by which material mixes at a convective boundary layer, which is best described as *turbulent entrainment*. Turbulent entrainment is the process by which material is drawn across a convective boundary layer by turbulent velocity fluctuations and differs qualitatively from the traditional "ballistic" picture of overshooting wherein large eddies are envisioned to penetrate into the stable layer (Zahn, 1991). What I find is that the empirical entrainment rates are governed by the characteristics of the turbulent flow and the stability structure of the convective boundary in the same manner as those found for geophysical flows. In particular, the entrainment rate is found to obey a power law dependence on a *bulk Richardson number*,  $Ri_B$  (eq. 4.1). The parameter  $Ri_B$  can be calculated directly from the one-dimensional model profile and provides an indicator of the qualitative nature of the hydrodynamic flow that takes place at the convective boundary, including the mixing rate.

In chapter 5, I reiterate some of the key results from this work and conclude by discussing some avenues for future research which build directly on the efforts laid down in this thesis.

## CHAPTER 2

### ACTIVE CARBON AND OXYGEN SHELL BURNING

*The material presented in this chapter was previously published in Meakin & Arnett (2006a)*

#### 2.1 Introduction

Numerical simulations of stellar evolution are generally based upon restrictive assumptions regarding dynamics (e.g., hydrostatic balance and mixing-length convection), because the dynamic timescales are so much shorter than the nuclear burning timescale. Neutrino cooling accelerates the last burning stages so that direct dynamic simulation is feasible (Bazan & Arnett, 1998; Asida & Arnett, 2000), at least for the oxygen burning shell. We are extending this work to longer evolutionary times, larger computational domains, and three dimensional flow (3D). In this chapter, I summarize new results with a discussion of the hydrodynamics underlying important symmetry breaking and compositional mixing processes which may significantly affect progenitor and core-collapse supernova models. A more detailed discussion of these results appears in subsequent chapters; I indicate some of the broader implications here.

#### 2.2 A Double Shell: Active Oxygen and Carbon Burning

Previously we have evolved a  $23M_{\odot}$  model with the one-dimensional TYCHO code to a point where oxygen and carbon are burning in concentric convective shells which overlay a silicon-rich core. The resultant stellar structure is presented in Figure 2.1. For subsequent hydrodynamic evolution we use the PROMPI



code described in the introduction. We use a 25 nucleus reaction network in these models, tuned to capture the oxygen and carbon burning energy generation rates to within 1% of the 177 species version used to evolve the 1D model. The 25 nucleus network contains electrons, neutrons, protons,  $^4\text{He}$ ,  $^{12}\text{C}$ ,  $^{16}\text{O}$ ,  $^{20}\text{Ne}$ ,  $^{23}\text{Na}$ ,  $^{24}\text{Mg}$ ,  $^{28}\text{Si}$ ,  $^{31}\text{P}$ ,  $^{32}\text{S}$ ,  $^{34}\text{S}$ ,  $^{35}\text{Cl}$ ,  $^{36}\text{Ar}$ ,  $^{38}\text{Ar}$ ,  $^{39}\text{K}$ ,  $^{40}\text{Ca}$ ,  $^{42}\text{Ca}$ ,  $^{44}\text{Ti}$ ,  $^{46}\text{Ti}$ ,  $^{48}\text{Cr}$ ,  $^{50}\text{Cr}$ ,  $^{52}\text{Fe}$ ,  $^{54}\text{Fe}$ ,  $^{56}\text{Ni}$ , and all significant strong and weak interaction links. The reaction rates, including  $^{12}\text{C}(\alpha, \gamma)$ , are from Rauscher & Thielemann (2000).

A two dimensional model has been calculated on a  $90^\circ$  wedge which is embedded in the equatorial plane of a spherical coordinate system and has radial limits which encompass both the oxygen and carbon burning convective shells. Table 2.1 lists some additional details of the simulated model. A three dimensional model including just the oxygen shell and bounding stable layers has been evolved to 800 seconds. (An extensive analysis of the 3D model is presented in Chapter 4.).

## 2.3 Results

*Flow Topology with Two Burning Shells.* Following the readjustment of the outer boundary due to small inconsistencies in the initial 1D model, a quasi-steady state flow develops, which is shown in Fig. 2.2. The top half of the figure shows the velocity magnitude; the lower shows energy generation. *Velocities are significant even in the nonconvective regions*, but have different morphology. The convective regions have round patterns (vortices) with occasional plumes, while the non-convective regions have flattened patterns (mostly g-modes). The flow fluctuates strongly. New fuel is ingested from above; the oxygen flame shows “feathery” features corresponding to such fuel-rich matter flashing as it descends. This was previously seen (Bazan & Arnett, 1998; Asida & Arnett, 2000). A new feature

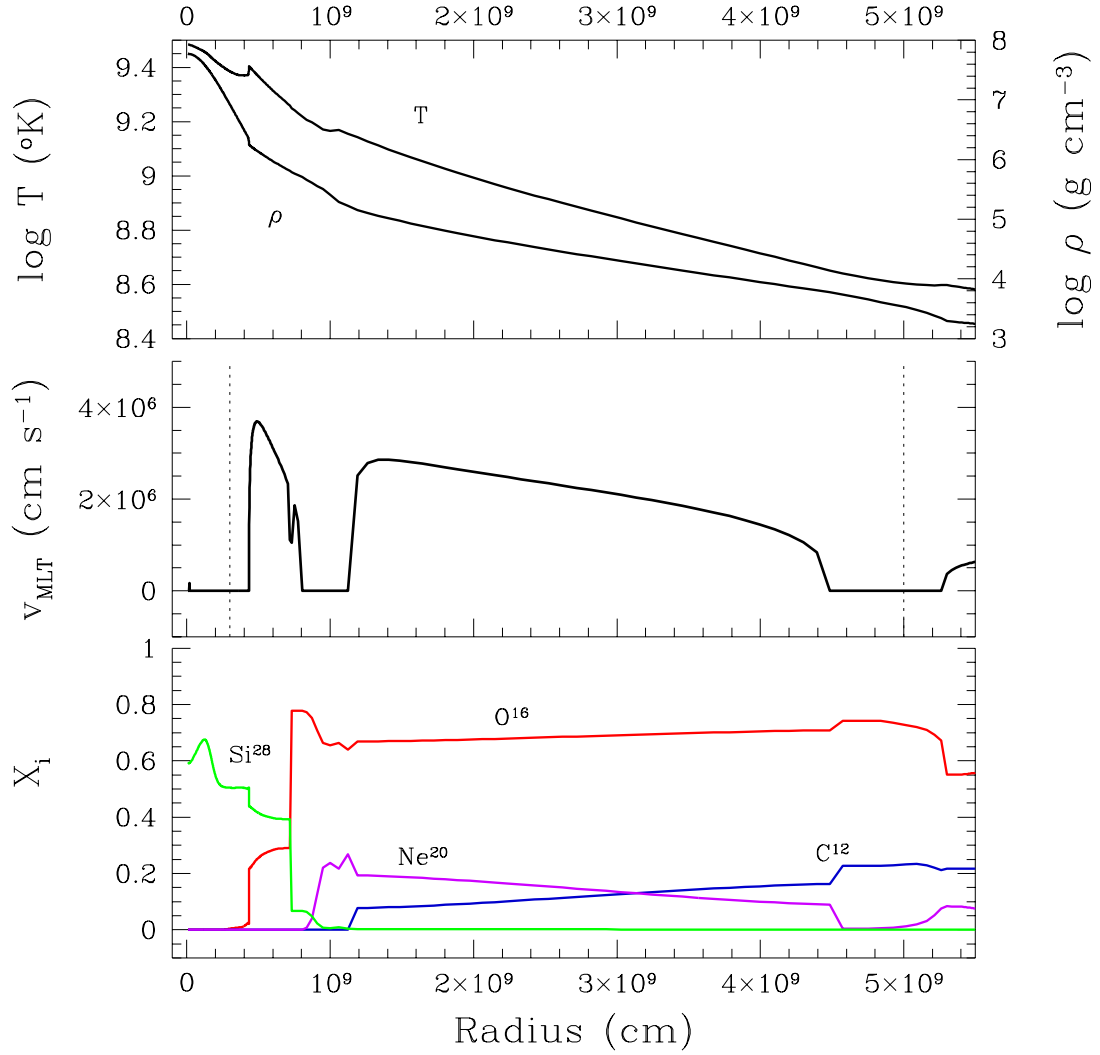


Figure 2.1: The  $23M_{\odot}$  TYCHO model used as initial conditions for the hydrodynamic simulation is shown here. (*top*) Density and temperature profiles are shown illustrating the large number of scale heights simulated as well as the complex entropy structure due to the burning shells. (*middle*) The mixing length velocities are shown and delineate the extents of the carbon and oxygen burning convection zones. The dashed vertical lines mark the boundaries of the simulation domain. (*bottom*) The onion skin compositional layering of the model is shown here for the four most abundant species.

Table 2.1. Model Parameters

Quantity	Value
Stellar mass ( $M_{\odot}$ ) . . . . .	23
Stellar age (yr) . . . . .	$2.3 \times 10^6$
Oxygen shell convective timescale <sup>a</sup> (s) . . .	$\sim 10^2$
Carbon shell convective timescale <sup>a</sup> (s) . . .	$\sim 10^3$
Hydro simulation time (s) . . . . .	$2.5 \times 10^3$
Inner, outer grid radius ( $10^9$ cm) . . . . .	0.3, 5.0
Pressure scale heights across domain . . .	$\sim 9$
Angular extent of grid (rad) . . . . .	$\pi/2$
Grid zoning, $n_r \times n_{\phi} \times n_{\theta}$ . . . . .	$800 \times 320 \times 1$
Numer of timesteps . . . . .	$\sim 1.5 \times 10^6$

<sup>a</sup>These convective timescales are based on the mixing length theory velocities.

appears in the movie version of Fig. 2.2, which shows a pronounced, low order distortion of the comoving coordinate, squashing and expanding the apparent circles on which carbon burning proceeds. This is due to the coupling of the two shells by waves in the nonconvective region between them. This behavior seems robust; we expect it to persist, so that at core collapse this part of the star (at least) will have significant nonspherical distortion.

*Stiffness and the Source of Density Perturbations.* Another asymmetry, nonspher-

ical density perturbations, was found by Bazan & Arnett (1998); Asida & Arnett (2000). The fluctuations in density and temperature, presented in the top panel of Figure 2.3 as root mean square deviations from an angular mean, reach values as large as  $\sim 10\%$  and are localized at the nonconvective region just beyond the convective boundary (top panel). The fluctuations are coincident with regions where the buoyancy frequency,  $N$ , is large, which can be seen in the bottom panel of Figure 2.3. Here,  $N^2$  is a measure of the “stiffness” of the stratification (Turner, 1973), and is proportional to the restoring buoyancy force on perturbed stellar matter,

$$N^2 = -g \left( \left. \frac{\partial \ln \rho}{\partial r} \right|_s - \frac{d \ln \rho}{dr} \right), \quad (2.1)$$

where  $g$  is the gravity, and the term in parentheses is the difference between the fractional density gradient of the stellar structure and the fractional density change due to a radial (adiabatic) Lagrangian displacement. Regions where  $N^2 \lesssim 0$  are unstable to convective motions. The spikes in  $N$  in our model are due to steep, stabilizing composition gradients which separate fuel from ash and lead to sharp gradients in density. Convection excites wave motions in the adjacent stable layers which give rise to the density perturbations. Similar internal wave phenomena can be observed in laboratory ice-water convection experiments where the largest temperature fluctuations are measured immediately above the convecting layer where the buoyancy frequency is large (Townsend, 1966), which highlights the generality of this phenomenon.

*Resonant Modes.* The underlying stellar structure determines the set of discrete resonant modes that can be excited. The narrow stable layers which bound the convective shells in our simulation, including the (truncated) core layer, are isolated enough from other wave propagation regions to act as resonating cavities. These modes are the deeper, interior counterparts to the modes observed in helio

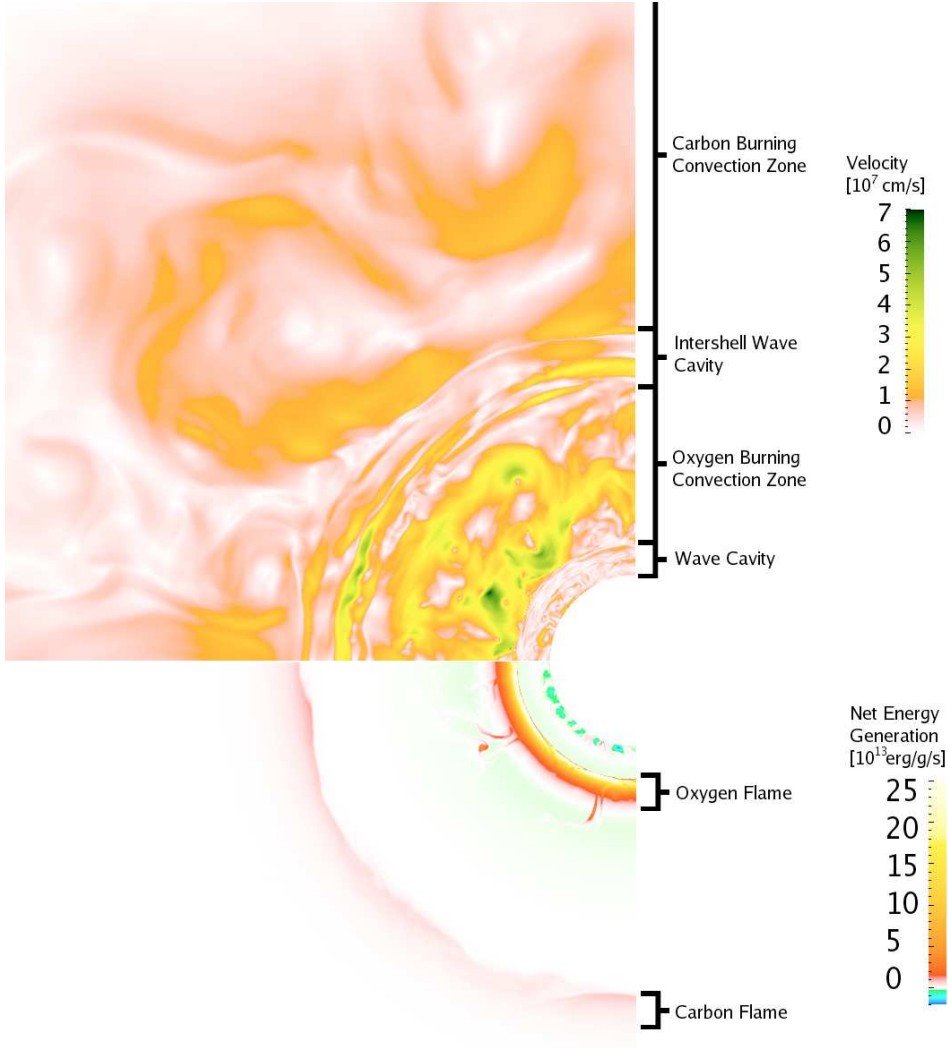


Figure 2.2: The magnitude of the flow velocity (*top*) and the net energy generation rate,  $\epsilon_{net} = \epsilon_{nuc} + \epsilon_{\nu}$  (*bottom*), is shown for a snapshot of the simulation which includes both an oxygen and carbon burning convection zone. The carbon burning convective shell extends to a radius of  $\sim 4.5 \times 10^9$  cm while the figure is truncated at a radius of  $\sim 2.9 \times 10^9$  cm for clarity. A weak silicon-burning convection zone develops at the inner edge of the grid due to a small boundary-zone entropy error which accumulates during the course of the calculation.

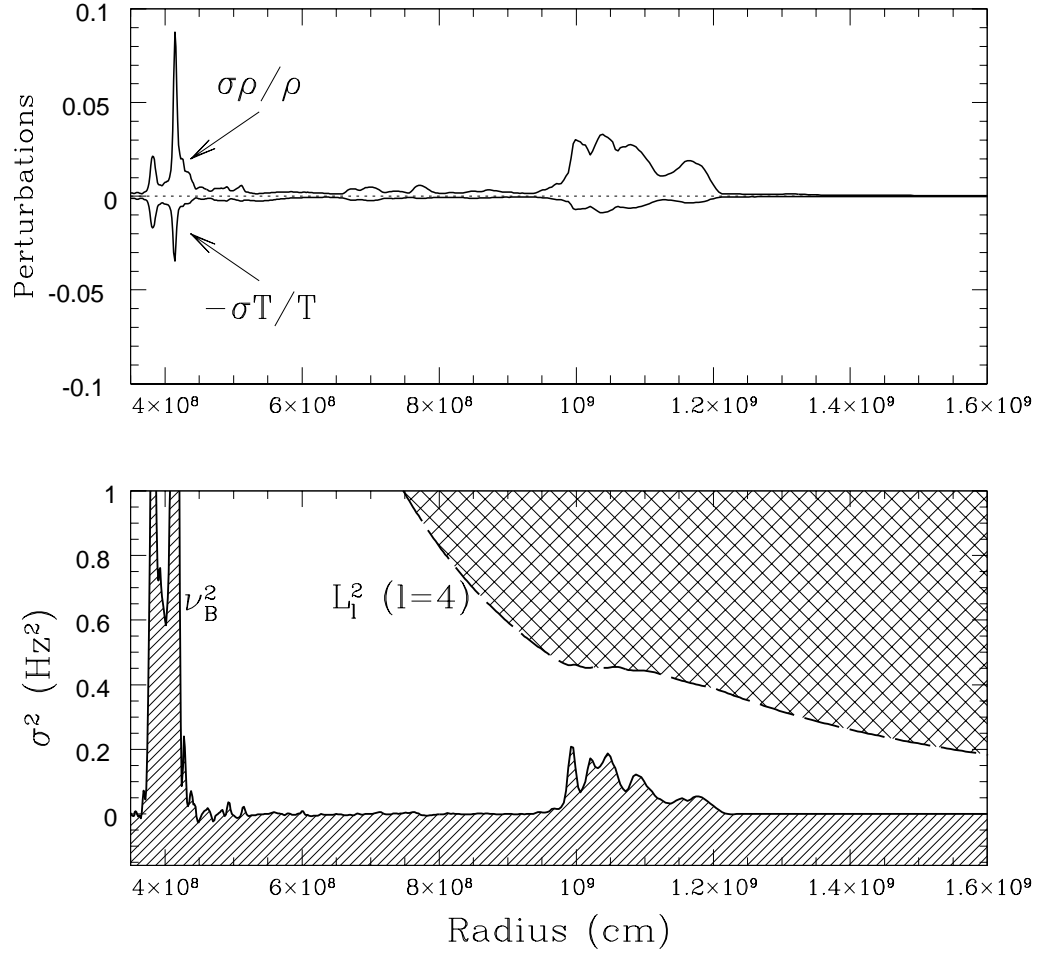


Figure 2.3: (*top*) Nonspherical density and temperature perturbations (root mean square fluctuation about the angular mean divided by the angular mean) are shown for the inner  $1.2 \times 10^9$  cm of the simulation domain. (*bottom*) In this propagation diagram (showing oscillation frequency versus stellar radius) the gravity wave and  $(l=4)$  acoustic wave propagation zones are indicated by the horizontal and cross-hatched shading, respectively. The gravity wave cavity is bounded above by the buoyancy frequency (solid line), while the acoustic cavity is bounded below by the Lamb frequency (dashed line).

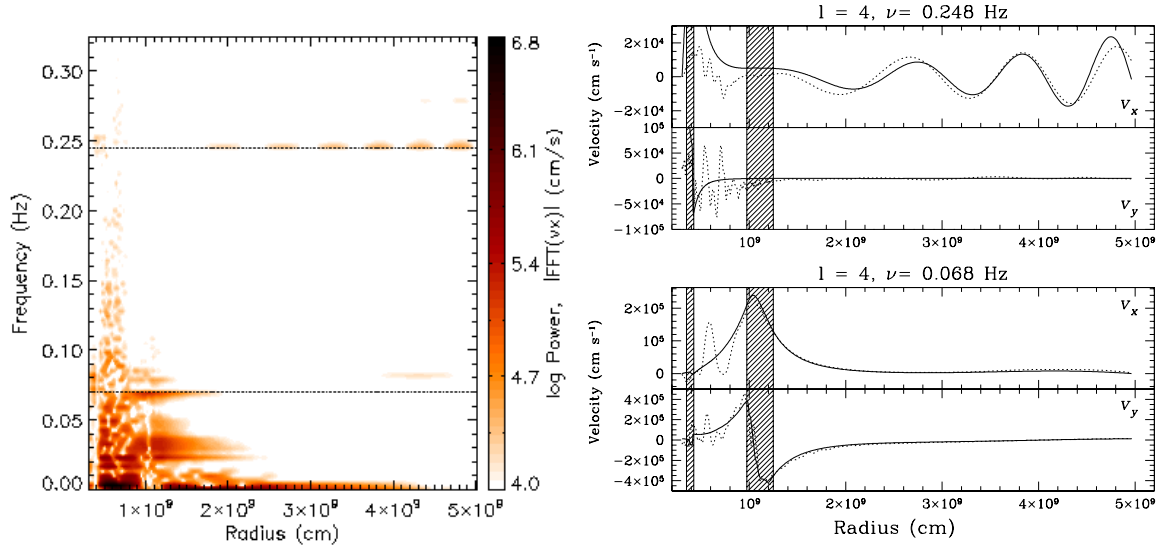


Figure 2.4: (*left*) The frequency power spectrum of the  $l=4$  component of the radial velocity ( $v_x$ ) is shown as a function of radius. The dashed horizontal lines indicate the frequencies of two waves with significant power that are compared to linear theory in the adjacent panel. (*right*) Two  $l=4$  wave forms are shown. The wave forms extracted from the simulation data (dotted line) and calculated with linear theory (solid line) are shown for comparison. For each mode the horizontal ( $v_y$ ) and radial velocity ( $v_x$ ) components are presented in units of  $\text{cm s}^{-1}$ . The shaded areas correspond to stably stratified regions. Both of these modes have some p- and g-mode character. The mode in the bottom panel is predominately of g-mode character, while the mode in the top panel is more clearly of mixed type.

and asteroseismology studies of milder evolutionary stages.

Each mode can be uniquely identified by its horizontal wavenumber index,  $l$ , and its oscillation frequency,  $\omega$ . We identify excited modes in our simulation by isolating spatial and time components of the motion through Fourier transforms. In Figure 2.4 we present a power spectrum at each radius in the simulation for motions with  $l = 4$ , the largest horizontal scale that can fit into the  $90^\circ$  wedge simulated. A direct comparison between modes identified in the simulation and those calculated from the linearized (non-radial) wave equation of stellar oscillations (see Appendix C) is presented in the right hand panel for two modes with significant power. Although the simulation data has additional features, including “noise” in the convection zones, the mode shapes in both velocity components are strikingly similar between simulation and the wave equation; the identification is unambiguous. Gravity waves evanesce (exponentially attenuate) beyond the boundaries of the stable layers but still contain significant power in the convection zones. Acoustic waves are free to propagate in the acoustic cavity which overlaps the carbon burning convection zone.

During the late evolutionary epoch simulated here, the g-mode and p-mode propagation zones are not widely separated in radius, allowing wave modes of mixed character to couple (Unno et al., 1989). The modes in the acoustic cavity are trapped by the boundary conditions of the calculation but would otherwise propagate into the stellar envelope where they would deposit their energy through radiative damping, providing an additional channel for energy transport out of the burning region.

The good agreement of the numerical modes with the analytic modes indicates that our numerical procedures give an excellent representation of the hydrodynamics of waves, even of very low Mach number. We note that anelastic



codes will not reproduce the p-mode and mixed mode waves properly, as we have ascertained by direct integration of the anelastic wave equation.

*Kinetic Energies and Wave Induced Mixing.* During the simulations, convective motions excite waves and build up significant kinetic energy in nonconvective regions. The integrated kinetic energies are  $2.1 \times 10^{45}$  ergs in the inner nonconvective region,  $5.2 \times 10^{47}$  ergs in the oxygen burning convective shell,  $9.7 \times 10^{45}$  ergs in the intermediate nonconvective region, and  $6.9 \times 10^{46}$  ergs in the carbon burning shell. The kinetic energy is small in the outer stable region, but is still increasing by the end of the simulation.

In our simulations, the importance of the excited g-modes in the stable layers lies primarily in the role they play in mediating mixing at the convective boundaries and in the stably stratified layers. We identify a cycle in which kinetic energy builds up in the stable layer until the underlying wave modes reach non-linear amplitudes, breakdown and drive mixing. This process is analogous to the physical picture which underlies semiconvective mixing (Stevenson, 1979; Langer et al., 1983; Spruit, 1992) but is driven on a hydrodynamic rather than a thermal timescale. The growth time for the fastest growing modes in our simulation is  $\sim 200$  seconds and leads to an average migration speed of outer oxygen shell boundary of  $\sim 4 \times 10^4 \text{ cm s}^{-1}$ , entraining mass into the convection zone at a rate of  $\sim 10^{-4} M_{\odot} \text{ s}^{-1}$ , significantly affecting the evolution. Identifying the spectrum of excited modes in numerical simulations, including amplitudes and waveforms, provides guidance for developing and testing a quantitative model of this mixing mechanism. An important parameter controlling the boundary entrainment rate is the Richardson number such that steeper density (and composition gradients) will lead to lower mixing rates so that sharp gradients are expected to form and persist (Peltier, 2003; Alexakis et al., 2004). In addition to the mixing associ-

ated with wave-breaking, enhanced compositional diffusion can be driven by the presence of the oscillatory flow setup by g-modes (Press, 1981; Knobloch & Merryfield, 1992). It has been demonstrated that the structure of presupernova iron cores is very sensitive to how mixing is handled at convective boundaries with significant implications for both the explosion mechanism and nucleosynthetic yields (e.g. Woosley & Weaver, 1988). If the amplitudes of the wave motions identified in our simulations remain robust to the numerical limitations (e.g., resolution, domain size) then neglecting the mixing processes associated with these waves constitutes a large source of error in progenitor models.

## 2.4 Discussion

*Differences in 2D and 3D.* While these 2D simulations allow us to see the interaction of carbon and oxygen shells, and show wave generation at convective boundaries, they impose an unphysical symmetry on the problem. Our 3D simulations, however, show that the wave generation is a robust result. The flow in the convection zones, however, is qualitatively different between the 2D and 3D models: the 2D flow is dominated by vortices which span the convection zone, while the 3D flow is characterized by smaller scale plumes. Quantitatively, the amplitude of the 2D convective motions is larger than the 3D by a factor of several, while the 3D motions are in fairly good agreement with those predicted by mixing length theory (see Chapter 4). *Two-dimensional simulations of gravitational collapse will be misleading at least to the extent that convective motions are important.*

*Presupernova Models.* Perhaps the most important impact that internal waves have on stellar structure in the late stages of massive star evolution is the degree to which they drive compositional mixing. In our simulations internal wave modes grow to non-linear amplitudes and mix material at convective boundaries

on a hydrodynamical timescale. Given the strong dependence of presupernova structure on the rate at which mixing occurs at convective boundaries we see the incorporation of internal wave physics into stellar evolution codes as a necessary refinement.

*Symmetry Breaking.* Spherical symmetry in presupernova models is broken by (1) the density perturbations induced by turbulence within the convection zone, (2) the wave interactions between burning shells, and (3) rotationally induced distortions. The perturbations by waves which are trapped between the oxygen and carbon burning shells are correlated on large angular scales, as is rotation, while the turbulent perturbations have both a smaller scale and amplitude. Our restricted simulation domain filters out wave modes with  $l < 4$ , so it is likely that even larger scale perturbations exist in real stars. Symmetry breaking will seed instabilities in an outward propagating supernova shock (Kuran et al., 2005), and in the collapsing core. The converging case has been intensely studied for inertial confinement fusion (Lindl, J., 1998). The diverging case has implications for the problem of  $^{56}\text{Ni}$  and  $^{56}\text{Co}$  decay in SN1987A (Herant & Benz, 1991; Kifonidis et al., 2003).

The conclusion that internal wave modes do not grow to large amplitudes during core collapse through nuclear driven overstability (Murphy et al., 2004), is based upon an analysis that ignores (1) the dynamics of convective motion and (2) the shell-shell interactions, both of which are expected to become more violent as collapse is approached. Asymmetries in core collapse have implications for pulsar birth kicks, explosion mechanisms, and for gravitational wave generation. Talon & Charbonnel (2005) have shown that internal gravity waves can transport angular momentum at a rate sufficient to be important in the evolution of solar mass stars; we suggest that they are important for evolution of more mas-

sive stars to core collapse, and for plausible prediction of the angular momentum distribution in that collapse.

To what extent are the hydrodynamic flows discussed in this chapter a product of the numerical scheme that we used? In the next chapter, we explore the robustness of our simulation results by comparing them to those of a similar evolutionary epoch (oxygen shell burning) which was calculated using an entirely different hydrodynamics solver, using the anelastic approximation. As will be shown, the comparison is encouraging.

## CHAPTER 3

## ANELASTIC AND COMPRESSIBLE MODELS OF OXYGEN BURNING

*It seems to me that the problem of wave emission by turbulent convection is getting ripe for a more detailed attack.*

Martin Schwarzschild (1960)<sup>1</sup>

## 3.1 Introduction

Oxygen burning (by  $^{16}\text{O}+^{16}\text{O}$  fusion) occurs in the precollapse stages of the evolution of massive stars. Neutrino cooling speeds these stages to the extent that the evolutionary times scales are close enough to the sound travel time so that direct compressible numerical hydrodynamics can be applied (Arnett, 1994). The first detailed studies of this stage (Bazan & Arnett, 1998) were done in two-dimensional symmetry (2D) with PROMETHEUS (Fryxell, Müller, & Arnett, 1989), a multi-fluid multidimensional compressible hydrodynamics code based on the Piecewise Parabolic Method (PPM) of Colella & Woodward (1984). They showed vigorous convection, with significant density fluctuations (up to 8%) at the convective-nonconvective boundaries. These results were confirmed in detail in 2D with the VULCAN Arbitrary-Lagrangian-Eulerian (ALE) hydrodynamics code (Livne, 1993) by Asida & Arnett (2000). VULCAN is an entirely independent compressible hydrodynamics code, so that these two sets of simulations only shared the initial model, the sonic time step limitation, and the 2D geometry. A new version of the PROMETHEUS code, PROMPI (which uses the Message Passing Interface

---

<sup>1</sup>Thirteenth Henry Norris Russell Lecture of the American Astronomical Society, published in *The Astrophysical Journal* (1961), 134, 1.

for parallelism), has extended the study to 3D. In all these compressible models except the earliest (Arnett, 1994) the computational domain has included both the convective oxygen burning shell as well as two bounding stably stratified layers.

Kuhlen, Woosley, & Glatzmaier (2003) investigated shell oxygen burning in 3D using an anelastic hydrodynamics code which filters out sound waves (and thus ameliorates the restrictive Courant condition<sup>2</sup> on the time step) and linearizes thermodynamic fluctuations around a background reference state (Glatzmaier, 1984; Gough, 1969). In contrast to the fully compressible results above, Kuhlen, Woosley, & Glatzmaier (2003) found only small density and pressure contrasts, and subsonic flows which were well within the anelastic approximation (all thermodynamic contrasts less than 1 percent). The boundary conditions used were impermeable and stress-free and were placed within the convection zone so that convective overshoot could not be studied. In particular, the dynamic consequences of the neighboring non-convective shells, and their elastic response to convective fluctuations, were ignored. The formulation was single fluid, so that effects depending upon composition, i.e., mixtures of fuel and ashes, were not modeled.

The applicability of both fully compressible and anelastic hydrodynamic methods has recently been challenged by developers of low-Mach number solvers (Almgren et al., 2006). The reliability of compressible codes has been questioned for low velocity flows due to possible violations of elliptic constraints that arise in the evolution equations in the very small Mach number limit (e.g., Schneider et al., 1999). The limits for which compressible solvers remain robust in the astrophysical context, however, has not been rigorously studied. Anelastic methods,

---

<sup>2</sup>The Courant condition is a stability restriction on the time stepping used by an explicit compressible hydrodynamics solver. The time step used must be smaller than the most restrictive sound crossing time for all of the grid zones.

on the other hand, enforce a divergence constraint on the mass flux ( $\nabla \cdot \rho \mathbf{v} = 0$ ) which filters out sound waves, but are formulated assuming that thermodynamic fluctuations are small and only linear deviations from a background reference state are retained. Therefore, this approximation is expected to fail for models which include large gradients in the thermodynamic variables such as occur at the boundaries of shell burning regions.

The correct identification of the behavior in shell oxygen burning has wide implications. This stage of massive star evolution is important for a variety of topics of current research interest (e.g. Young, et al., 2005, 2006). In this chapter, I discuss the quantitative similarities and differences between the models of oxygen shell burning which were introduced above and show that the two models are in good agreement with each other. In addition, the compressible models are in agreement with scaling relations derived from the basic hydrodynamic equations as well as analytic solutions to the non-radial wave equation for motions in the stable layers. These findings lend strong support to the validity of both simulations. There are no signs that either the anelastic or the PPM method is breaking down for the conditions simulated, even in regions of the flow where the Mach number does not exceed  $M \sim 0.01$ .

## 3.2 Model Comparison

### 3.2.1 The Initial Models and Simulation Parameters

Table 3.1 summarizes the initial conditions, computational domains, zoning, and properties of the developed flow for the three models discussed in this paper. These include a 2D and a 3D compressible model calculated with the PPM method (see Chapters 2 & 4 for additional details) and the non-rotating anelastic model described by Kuhlen, Woosley, & Glatzmaier (2003). The initial conditions for the

compressible simulations are of a  $23 M_{\odot}$  star previously evolved with the TYCHO stellar evolution code (Young & Arnett, 2005) which is directly mapped onto the hydrodynamics grid. A 25 nuclei reaction network is used to track composition and energy generation. The computational domains for the compressible models are restricted to fractions of a sphere and use a spherical coordinate system. The 2D model is a  $90^{\circ}$  wedge embedded in the equatorial plane, and the 3D model is a wedge of  $30^{\circ} \times 30^{\circ}$  degrees centered on the equator. The radial limits for these models enclose both the convectively unstable oxygen burning shell, as well as two surrounding stably stratified layers. Boundary conditions, which are *placed in the stable layers*, are impermeable and stress free. The net energy generation due to nuclear burning and neutrino cooling,  $L_{net} = \int (\epsilon_{nuc} + \epsilon_{\nu\bar{\nu}}) dM \approx 3.5 \times 10^{46}$  erg/s, is positive and goes into PdV work through a background expansion which develops naturally in the compressible model in the same way it does in the initial TYCHO model.

The anelastic model uses a reference state which is a polytropic fit to a  $25 M_{\odot}$  stellar model which was evolved with the KEPLER code (Weaver et al., 1978). A multi-fluid model and reaction network are not used and nuclear energy generation is instead estimated using a power law fit for density and temperature dependence. The anelastic model uses spherical harmonics for angular coverage, ameliorating the pole singularity problem of a spherical coordinate system, and covers a full  $4\pi$  steradians. Chebyshev polynomials are used in the radial direction. The radial limits of the anelastic model enclose *only the convection zone with no regions of stable stratification*. The boundary conditions, which are within the unstable convective layer, are also impermeable and stress free. The net energy generation is positive,  $L_{net} \approx 1.5 \times 10^{45}$  erg/s. The anelastic model used is unable to model background expansion so the excess energy is forced to escape from the



outer boundary of the calculation. The lower net energy generation of this model may be due to its being in a later evolutionary stage.

Both hydrodynamic models use the equation of state provided by Timmes & Swesty (2000). The radial limits of the oxygen burning convection zone and enclosed mass for the two initial models evolved with the KEPLER and TYCHO codes are remarkably similar. The compressible model uses 400 logarithmically spaced radial zones (to keep zone aspect ratio  $dr/r d\theta \sim 1$ ) and an angular resolution of  $\sim 0.3^\circ$  per zone. The anelastic model uses 145 zones for a comparable radial extent, and spherical harmonics up to order  $l = 63$  to cover the sphere which is roughly equivalent to a Nyquist sampling of  $\sim 1.5^\circ$  per zone, approximately a factor of five lower angular resolution than the compressible model. The Rayleigh and Reynolds numbers quoted by Kuhlen, Woosley, & Glatzmaier (2003) are  $Ra \sim 5 \times 10^7$  and  $Re \sim 3000$ . Since the compressible model is more strongly driven (larger  $L_{net}$ ) and has finer zoning (resulting in a lower effective viscosity), both the effective Rayleigh and Reynolds numbers will be higher in the compressible model.

### 3.2.2 Flow Properties: Anelastic Model

The anelastic simulation has been run for 6500 seconds. With an average flow velocity of  $v_c \approx 0.49 \times 10^7$  cm/s, and a radial extent for the convection zone  $\Delta R \approx 0.39 \times 10^9$  cm the turnover time  $t_c = 2\Delta R/v_c \approx 159$  seconds and the simulation spans approximately 41 convective turnovers. The peak velocity is given as  $v_{peak} \approx 1.8 \times 10^7$  cm/s which corresponds to a peak Mach number  $M \sim 0.04$  for a sound speed  $c_s \approx 4.5 \times 10^8$  cm/s. The maximum density fluctuations within the convection zone are found to be of the order  $\rho'/\langle\rho\rangle \sim 2 \times 10^{-3}$  which is the same order of magnitude as the peak Mach number squared,  $M^2 \sim 1.6 \times 10^{-3}$  consistent with the scaling arguments for the anelastic approximation for thermal

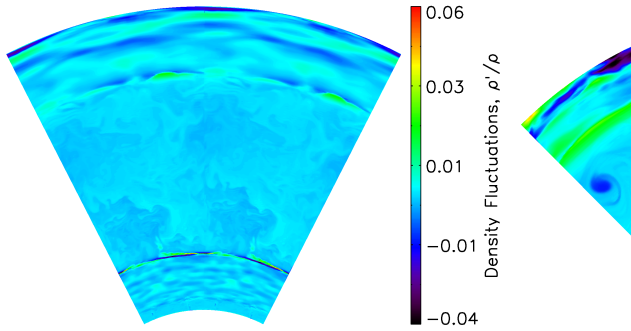


Figure 3.1: Spatial distribution of density fluctuations are shown for (left) a slice through the 3D compressible model and (right) the 2D compressible model. In both models the flow is composed of two distinct regimes, including the convective flow in the center which is bounded above and below by stably stratified layers which are host to internal waves. The scale on the 2D model has been truncated to same limits as the 3D model for comparison, but extreme values exceed the scale limits by a factor of  $\sim 2$ . The 3D model has been tiled twice in angle for clarity.

convection (Gough, 1969).

### 3.2.3 Flow Properties: Compressible Models

The flow in the compressible simulations consists of two distinct regimes: the turbulent convection zone, and the wave-bearing stably-stratified layers. These can be quite readily discerned in the density fluctuation field shown in Figure 3.1. In this section I discuss these two regimes in turn for the three dimensional model, and then discuss the properties of the two dimensional model.

The three dimensional compressible model was run for  $\sim 800$  seconds of star time. The average flow velocity is found to be  $v_c \approx 0.8 \times 10^7$  cm/s. With a convection zone width  $\Delta R \approx 0.41 \times 10^9$  cm the turnover time is  $t_c \approx 103$  seconds and the simulation spans approximately 8 convective turnovers. After an ad-

justment in the initial size of the convection zone due to penetrative convection (see Chapter 2 & 4), the flow achieves a steady state within  $\sim 200$  seconds, or two convective turnovers, after which the average flow properties do not change appreciably. Figure 3.2 shows the peak density fluctuation and the Mach number at each radius for the three dimensional model. Within the convection zone,  $0.44 < r/10^9 \text{ cm} < 0.85$ , the maximum density fluctuation and Mach number are  $\rho'/\langle\rho\rangle \sim 5 \times 10^{-3}$  and  $M \sim 0.09$ , respectively. Here also, the fluctuation scale is the same order of magnitude as the peak Mach number squared,  $M^2 \sim 8 \times 10^{-3}$ . The rms Mach number in the convection zone is  $M_{rms} \sim 0.01$ .

These velocity and fluctuation scales are comparable to those of the 3D anelastic model and are listed in Table 1 for both simulations for comparison. The point we want to emphasize here is that *the character of the convective flow is quantitatively in agreement between the anelastic and compressible models*. We also find, from the comparison presented in Chapter 4, that the 3D compressible model compares well with the stellar mixing length theory (Kippenhahn & Weigert, 1990), including the velocity scale ( $v_c \sim 10^7 \text{ cm/s}$ ) and the superadiabatic stratification ( $\Delta\nabla \sim 5 \times 10^{-4}$ ). The slightly larger velocity scale in the compressible model compared to the anelastic can be attributed to the higher Rayleigh number due to the larger luminosity needed to be transported by the convective flow.

### 3.2.3.1 Additional Sources of Fluctuations

In this section I discuss the origins of thermodynamic fluctuations which are due to physics not included in the anelastic model of Kuhlen, Woosley, & Glatzmaier (2003), including stably stratified layers and composition effects. I begin with a discussion of the internal wave dynamics occurring near the convective boundaries.

Significant density fluctuations occur at the convective boundaries in the com-

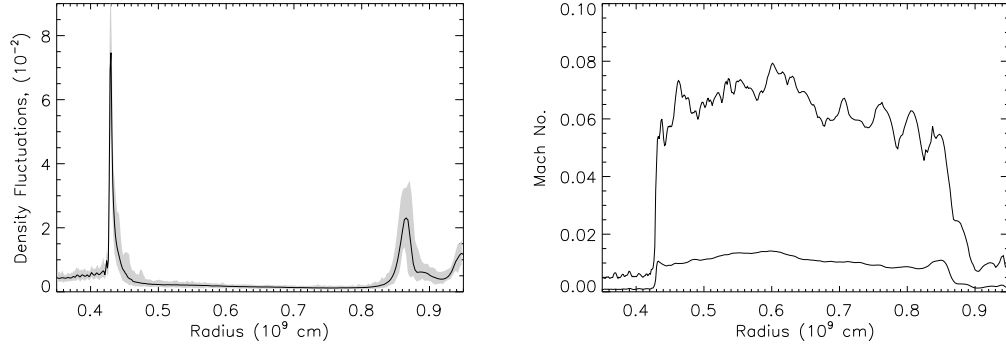


Figure 3.2: (left) Density fluctuations for 3D compressible model: The time average of the maximum density fluctuation is shown as the thick line, with the extreme values for the averaging period (two convective turnovers) shown as the shaded region. Within the body of the convection zone the average fluctuations are quite low  $\sim 0.25\%$ . The largest fluctuation (the spike at  $r \approx 0.43 \times 10^9$  cm) is  $\sim 11\%$  (exceeding the plot limits), while the secondary maximum ( $r \approx 0.85 \times 10^9$  cm) reaches  $\sim 3.5\%$ . These fluctuations occur in the radiative regions that enclose the convection zone (outside the computational domain of Kuhlen, Woosley, & Glatzmaier (2003)). (right) Mach number for the 3D compressible model: shown is the instantaneous value of the maximum Mach number at a given radius (thick line), and the rms Mach number (thin line).

compressible model, reaching values as large as  $11 \times 10^{-2}$ , over twenty times larger than in the body of the convection zone (Figure 3.2 and Table 3.1). Examining the spatial distribution of the density fluctuations presented in Figure 3.1 reveals that the largest fluctuations occur at the interface between the convection zone and the stably-stratified, wave-bearing layers. The morphology of the largest density fluctuations in the domain (i.e., those at the convective boundary) are periodic in angle and harmonic in time, identifying them with internal wave dynamics.

In the following discussion I present analytic estimates for the amplitudes of the density fluctuations at the convective boundary and show that they are in good agreement with the simulation data.

For small amplitude waves the Eulerian density fluctuations and pressure fluctuations are related by (Unno et al., 1989, p.93):

$$\frac{\rho'}{\langle \rho \rangle} = \frac{p'}{\langle p \rangle} \frac{1}{\gamma_{ad}} + \xi_r \frac{N^2}{g} + (\text{nonadiabatic terms}) \quad (3.1)$$

with buoyancy frequency  $N$ , and Lagrangian displacement  $\xi_r$ . I defer a discussion of nonadiabatic and composition effects to the end of this section. In the convection zone, material is nearly neutrally stratified and the buoyancy frequency is very close to zero so the second term on the right hand side is not very important. At convective boundaries the stellar structure assumes a stable stratification with a positive buoyancy frequency, and this term can become dominant. This term represents the component of the Eulerian density fluctuation due to g-mode oscillations and is the projection of the Lagrangian displacements of the wave,  $\xi_r$ , onto spherical shells. In the presence of steep density gradients, waves can lead to large Eulerian fluctuations even when compressibility is not important. To be as clear as possible on this key point, we give an analogy to well known physics: consider waves on a lake. The Lagrangian surface is the surface of the water. The Eulerian surface is the average level of the water and Eulerian density fluctuations occur as the waves (water) and troughs (air) move by the observer. The large variation in density is not due to compression, but the choice of coordinates (Eulerian in this case).

In order to estimate the amplitude of the density fluctuations using equation 3.1 we need to know the size of the pressure fluctuation and the maximum radial displacement amplitude,  $\xi_r^{\max}$ , for wave motions at the boundary. Both quantities

can be estimated by assuming that the ram pressure of the convective turbulence is balanced by wave induced pressure fluctuations at the convective/stable layer interface:

$$\rho v_c^2 \approx p'_w. \quad (3.2)$$

The validity of this approximation is demonstrated in Figure 3.3, which shows that the RMS horizontal pressure fluctuations and the turbulent ram pressure are comparable in the convection zone and do indeed balance at the locations of the convective boundaries.

The relationship between the pressure fluctuation of an internal wave,  $p'_w$ , and the maximum radial displacement,  $\xi_r^{\max}$ , depends on the wave frequency  $\sigma$  and horizontal wavenumber  $k_h$ . Perhaps the simplest approximation is to assume that internal waves generated at the convective boundary are directly related to the convection through the convective velocity  $v_c$  and eddy scale,  $l_c \sim H_p$ , by  $v_c \sim \sigma/k_h$  and  $k_h \sim 2\pi/l_c$  in the spirit of stellar mixing length theory (Press, 1981). Adopting these values we can then use the linearized momentum equation (Unno et al., 1989, p.96),

$$\xi_h^{\max} \sim \frac{[l(l+1)]^{1/2} p'_w}{r\sigma^2} \approx \frac{k_h}{\sigma^2} v_c^2 \quad (3.3)$$

and the dispersion relation (for waves in which  $\sigma \ll N < L_l$ ),

$$k_h/k_r \sim \frac{\sigma}{N} \quad (3.4)$$

to estimate the radial displacement:

$$\xi_r^{\max} = \xi_h^{\max} \times k_h/k_r \sim \frac{k_h v_c^2}{\sigma^2} \frac{\sigma}{N} \sim v_c/N. \quad (3.5)$$

The dispersion relation used to connect the horizontal and radial displacement amplitudes is valid when the wave frequency is much smaller than both the buoyancy frequency and the Lamb frequency  $L_l = k_h c_s$ , with sound speed  $c_s$ , and is a reasonable approximation for the wave properties adopted above (where  $\sigma/L_l \approx M_c$ ).

Here, our main result is the last expression in equation 3.5 for the radial displacement amplitude of the interfacial wave which is in pressure balance with the ram pressure of the convection. This expression is equivalent to the statement that the kinetic energy of the turbulent motion exciting the wave is balanced by the potential energy of the wave, which follows naturally from the basic energetic properties of waves in fluids (Lighthill, 1978).

Finally, we use the displacement given by equation 3.5 and the pressure fluctuation in equation 3.2 with equation 3.1 to arrive at our estimate for the interfacial density fluctuation amplitude,

$$\frac{\rho'}{\langle \rho \rangle} \sim M_c^2 + \frac{v_c N}{g} \quad (3.6)$$

in terms of the Mach number  $M_c$ , gravity  $g$ , and buoyancy frequency  $N$ . Adopting flow parameters from the simulation ( $v_c \sim 10^7$ ,  $g \sim 10^9$  in cgs units) we find  $\rho'/\langle \rho \rangle \sim (10^{-3} + N \times 10^{-2})$  with  $N$  in rad/s. The validity of this expression is apparent when comparing the buoyancy frequency in Figure 3.3 with the density fluctuations at the convective boundaries in Figure 3.2.

It can also be seen that the density fluctuations throughout the stable regions, not just at the convective boundaries, are in rough agreement with the scaling given by equation 3.6, though the amplitudes in the stable layers drop off with distance from the convective boundary. This is due to a spectrum of internal wave modes excited at the convective boundaries, rather than the single mode assumed

in the above analysis. Each modal component contributes to the pressure balance at the convective boundary and is composed of wave packets that travel back and forth within the resonating cavity of the stable layer (Unno et al., 1989) causing fluctuations throughout the region. A more detailed analysis is possible in which the entire spectrum of internal waves is estimated by matching the wave motions to those of the spectrum of turbulent convection (e.g. Carruthers & Hunt, 1986). Our single mode approach, however, works very well in describing the amplitudes of the fluctuations at the convective boundaries and provides a reasonable upper limit to the fluctuations throughout the entire stable layer.

I conclude this section with a discussion of the role that entropy fluctuations play in setting the scale of density fluctuations and hence buoyancy of material in the convection zone. The non-adiabatic term in equation 3.1 takes the form,

$$\frac{\rho'}{\langle \rho \rangle} = \frac{v_T}{c_p} \delta S \quad (3.7)$$

with thermodynamic derivative  $v_T = -(\partial \ln \rho / \partial \ln T)_p$ , specific heat at constant pressure  $c_p$ , and Lagrangian entropy fluctuation  $\delta S$ . In the present model the largest non-adiabaticity is the net effect of nuclear burning and neutrino cooling. The entropy fluctuation can then be written  $\delta S_{nuc} = \delta Q_{net}/T \approx \epsilon_{net} \delta t / T$  where the time material dwells in the burning region is  $\delta t \approx \Delta r / v_c \sim l_c / v_c \sim 10s$ . For the nuclear energy release in the current model, with a peak burning rate of  $\epsilon_{net} \sim 10^{14}$  erg/g/s, the maximum entropy fluctuation will be of order  $\delta S_{nuc}^{max} \sim 0.01$  in units of  $N_A k_B$ . The corresponding maximum density fluctuation will be approximately  $\rho' / \langle \rho \rangle|_{nuc} \sim 2.5 \times 10^{-3}$ , which is of order the amplitude of the fluctuations due to the weak compressibility effects in the convective flow. These values compare well to the perturbations estimated using mixing length theory, consistent with the convective flow being driven by the nuclear burning luminosity in the



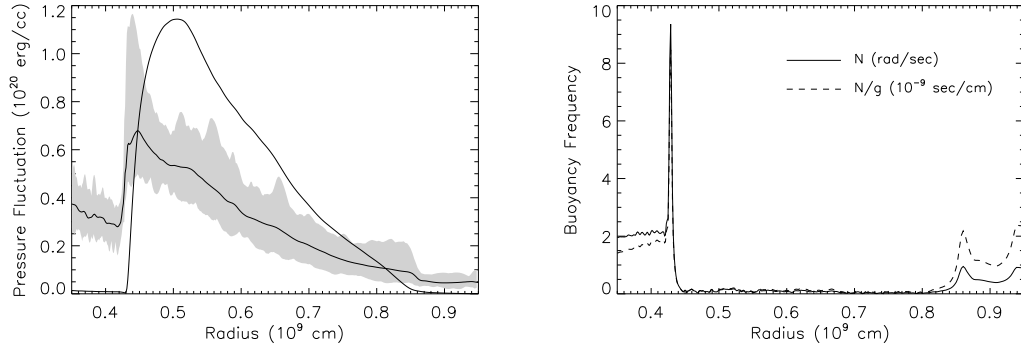


Figure 3.3: (left) Pressure fluctuations in 3D compressible model: The time averaged horizontal RMS pressure fluctuations are shown as the thick line, with the envelope of extreme values over two convective turnovers indicated by the shaded region. The radial ram pressure of the turbulent convection,  $\rho v_r^2$ , is shown as the thin line. The curves cross at the convective boundaries where the turbulent pressure is balance by the pressure fluctuation induced by internal waves in the adjoining stably stratified layers. (right) The magnitude of the buoyancy frequency is shown in units of rad/s. Also shown by the dashed line is the buoyancy frequency normalized by the gravity which, through Equation 3.6, sets the scale of the density fluctuations at the convective boundaries (compare with Figure 3.2(left)).

shell.

Entropy fluctuations also occur within the convection zone due to composition inhomogeneities. The radial entropy profile and the RMS entropy fluctuations are presented in Figure 3.4. The fluctuations are due to: (1) interfacial wave motions which cause Eulerian fluctuations in the same manner as for the density fluctuations discussed above; and (2) the entrainment of high and low entropy material at the convective boundaries which is mixed into the nearly adiabatic convection zone. The wave induced fluctuations appear as spikes near the con-

vective boundaries and are present in both the curve of minimum and maximum fluctuation. The regions affected by compositional inhomogeneities are labeled in Figure 3.4, with low entropy material entrained from below and high entropy material entrained from above. The entropy fluctuations associated with this material are another source of density fluctuations and explains the larger values that occur just within the boundaries of the convection zone in Figure 3.2. The entropy fluctuations associated with the entrained material are much larger than those due to nuclear burning (the entropy perturbation in the region of greatest nuclear energy deposition,  $r \sim 0.45 \times 10^9$  cm, is primarily *negative*). The entrainment of material from stable layers by a turbulent convective flow is an essential addition to stellar evolution modeling with significant consequences for the evolution of burning shells in presupernova models. An analysis of the entrainment properties is included in Chapter 4.

### 3.2.3.2 Dimensionality

It has long been known that 2D simulations were informative only to the extent that care is used in their interpretation. In 2D the vorticity is restricted to the direction normal to the computational domain, while in 3D instabilities cause its orientation to wander. Thus 2D is useful in situations in which there are physical reasons to enforce the symmetry (e.g., terrestrial cyclonic storms), but has nevertheless been used widely in more general applications because of computer resource limitations. The increasing availability of computing clusters and software parallelization tools is now making 3D hydrodynamic simulation more common, and we are starting to assess the adequacy and limitations of earlier 2D work.

We have calculated a 2D compressible model for 2400 seconds of star time. We find an average flow velocity of  $v_c \approx 2.0 \times 10^7$  cm/s and a convective turnover time of  $t_c \approx 40$  seconds, so our simulation spans approximately 60 turnover times.

The peak velocity during the course of the simulation is  $\sim 5.5 \times 10^7$  cm/s, corresponding to a peak Mach number of  $M \sim 0.163$ . The density fluctuations within the convection zone reach a maximum value of  $\rho'_c/\langle\rho\rangle \sim 6 \times 10^{-2}$ . At the convective boundaries the density fluctuations attain a peak value of  $\rho'_b/\langle\rho\rangle \sim 12 \times 10^{-2}$ .

We find two significant differences between the 2D and 3D models. First, we find a significantly decreased turbulent mixing rate in the 2D simulation. Material entrained into the convection zone at the boundaries is pulled into the large cyclonic flow patterns in the 2D simulation where large composition inhomogeneities persists for several convective turnovers. In contrast, material entrained into the convection zone in the 3D models is homogenized within a single convective turnover time. This effect is illustrated in Figure 3.5, which shows the spatial distribution of oxygen abundance, as well as RMS fluctuations for both the 2D and 3D simulations. The 2D simulation retains high level fluctuations throughout the convective zone, while inhomogeneities in the 3D model are mixed to low levels by the time material completes a single crossing. Figures 3.5 and 3.1, which are snapshots at the same time, reveal that the high entropy oxygen entrained at the top boundary corresponds to a negative density perturbation.

The second major discrepancy between the 2D and 3D models is the convective velocity scale. We find that both the mass averaged convective velocity and the peak velocity fluctuation are  $\sim 2$  times larger in the 2D model. This velocity scale difference may be connected to the lower turbulent mixing efficiency in the 2D flow. We find that the net enthalpy flux, which consists of upward and downward directed components,  $F_{net} = F_{up} - F_{down}$ , is the same between the 2D and 3D models. In the 2D model, however, the relative value of the individual flux components relative to the net flux, e.g.,  $F_{up}/F_{net}$ , is much larger than in the 3D model. Therefore, the 2D model requires a larger velocity scale to move the

same net flux due to the inefficiency of depositing the advected enthalpy across the convection zone.

We find that 2D and 3D models compare well in the wave region, but differ in the convection zone. The 3D convection is more similar to that of the anelastic model of Kuhlen, Woosley, & Glatzmaier (2003) and the values predicted by mixing length theory. While waves behave similarly in 2D and 3D, turbulent convection does not, particularly with regards to turbulent mixing efficiency. Although the spatial resolution of the 2D and 3D models is the same, the number of degrees of freedom in the angular direction is much larger in the 3D model,  $N_{3D}/N_{2D} = (100)^2/320 \sim 31$ . If the number of degrees of freedom were the only important parameter determining the degree to which the flow becomes turbulent, one might wonder if 2D can provide a more efficient surrogate to 3D. It turns out that 2D is actually more expensive than 3D because the same degrees of freedom in 2D requires a higher spatial resolution and hence a more severe time step constraint, and computational cost is  $N_{cost} \propto N_{space} \times N_{time}$ .

### 3.3 Conclusions

A comparison between the flow properties in fully compressible and anelastic simulations of stellar oxygen shell burning indicates that the two methods produce quantitatively similar results. Both methods produce convective flows in 3D models which are compatible with the results expected for the mixing length theory of convection for this phase. The compressible models have been extended to include additional physics not included in the anelastic model, namely stably stratified boundary layers and a multi-fluid flow ( $N_{species} = 25$ ). The interaction between the convection and the stable layers excites internal waves which produce larger thermodynamic fluctuations (up to 11% in 3D). Composition in-

homogeneities due to ongoing entrainment events at the convective boundaries also cause density fluctuations on the several percent level, though material is homogenized rapidly in the 3D model through turbulent mixing.

The relatively large fluctuations which arise at the convective boundaries  $\sim 11\%$  may stress the reliability of the anelastic approximation if this region is to be included in future simulations of oxygen burning, or later epochs where entropy and density gradients are large. A variety of convection studies have shown that boundary condition type (e.g., hard wall compared to stable layer) alters the overall flow pattern within a convection zone (Hossain & Mullan, 1993; Rogers & Glatzmaier, 2005) and therefore the astrophysically correct conditions should be used. Low Mach number solvers (e.g. Lin et al., 2006) may be the most efficient tools for extending studies of oxygen and silicon shell burning to full spherical domains in 3D while retaining the crucial density gradients at the convective boundaries where convective penetration and entrainment operate, and asymmetric fluctuations arise which may have important implications for the evolution of pre-supernova models. Earlier stages such as carbon and neon burning have both milder flows and shallower density gradients and should be better suited for anelastic methods, even at convective boundaries. However, background expansion and multi-fluid effects should be included. The large time step advantage of the anelastic and low Mach number simulations allows for much larger domains or better resolution.

Although the efficiency of fully compressible hydrodynamics may be low for the Mach numbers modeled, there are no signs that the solver used is breaking down in the oxygen shell burning simulations presented here. This conclusion is supported on several grounds, including: (1) The compressible model is in good agreement quantitatively with the anelastic methods for the convection zone re-

gion, including the velocity scales, and thermodynamic fluctuation amplitudes, a region in which the anelastic method is expected to perform well. (2) The compressible simulation of the convection zone is also in good agreement with the results of the one-dimensional TYCHO model, including the velocity scale and background stratification estimated using mixing length theory. (3) The dynamics in the stably stratified layers in the simulation agree well with the analytic solutions to the non-radial wave equation, including the decomposition of the flow into specific, unambiguous modes (Chapter 2). (4) The fluctuation amplitudes at the convective boundaries which are due to wave motions are found to be in good agreement with analytic estimates for their scale.

Contrary to the assertion made by Almgren et al. (2006) that compressible codes should generally fail for  $M < 10^{-2}$ , we find a robust solution that agrees with an anelastic method for the same region simulated. Additionally, recent compressible simulations of He shell flash convection by Herwig et al. (2006) using the finite-volume Godunov code RAGE (Baltrusaitis et al., 1996) find a flow with  $M \sim 10^{-3}$ , with apparently robust results, including well behaved g-modes. Almgren et al. (2006) present an example simulation illustrating the failure of PPM to track temperature for a simple flow with Mach number  $M \sim 0.05$ . This calculation, however, uses a compressible PPM code (FLASH) with two major differences from ours (PROMPI): they used the hydrodynamic procedure described in Zingale, et al. (2002) to remove the hydrostatic pressure from the Riemann solver, and their stellar model was much more degenerate than ours (the equation of state tends to become independent of temperature under their conditions, and care must be taken with cancellation of terms).

In the next chapter, a more extensive analysis of the convective flow and the mixing rates at convective boundaries is presented. In addition, a model of core

convection during hydrogen burning is introduced in order to test the degree to which the properties of the flow observed in the oxygen shell burning model are of more general applicability.

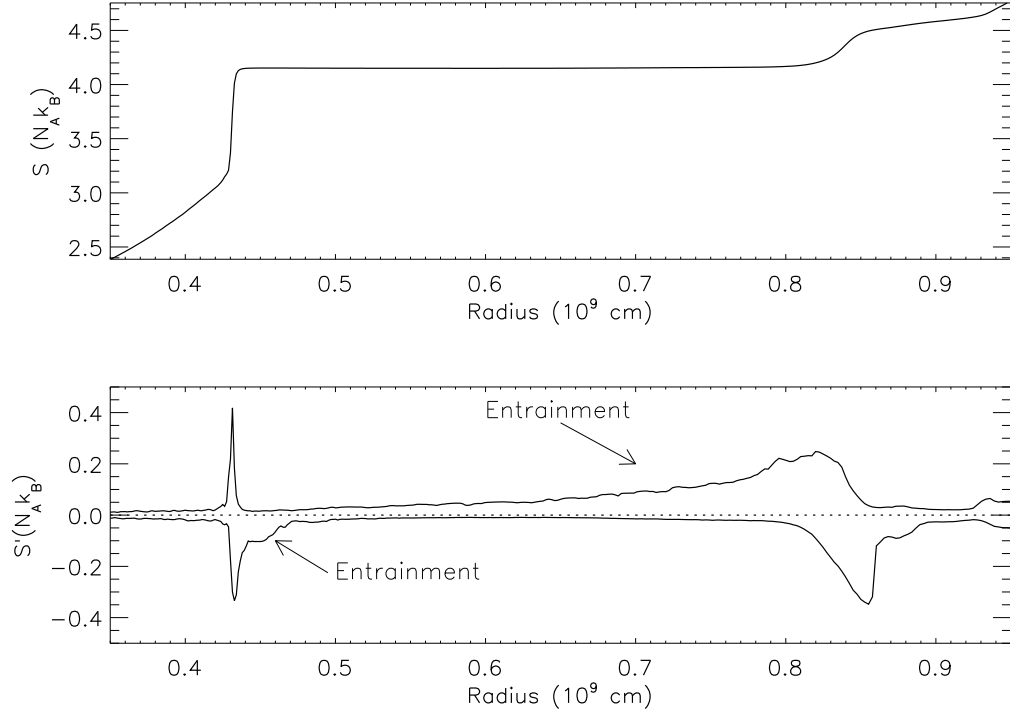


Figure 3.4: (top) Entropy profile of 3D compressible model. (bottom) Entropy fluctuations for 3D compressible model: The two solid lines indicate the maximum and minimum fluctuation for a given radius over the course of two convective turnovers. The annotations indicate fluctuations due to low entropy material entrained at the lower boundary and high entropy material entrained at the upper boundary.



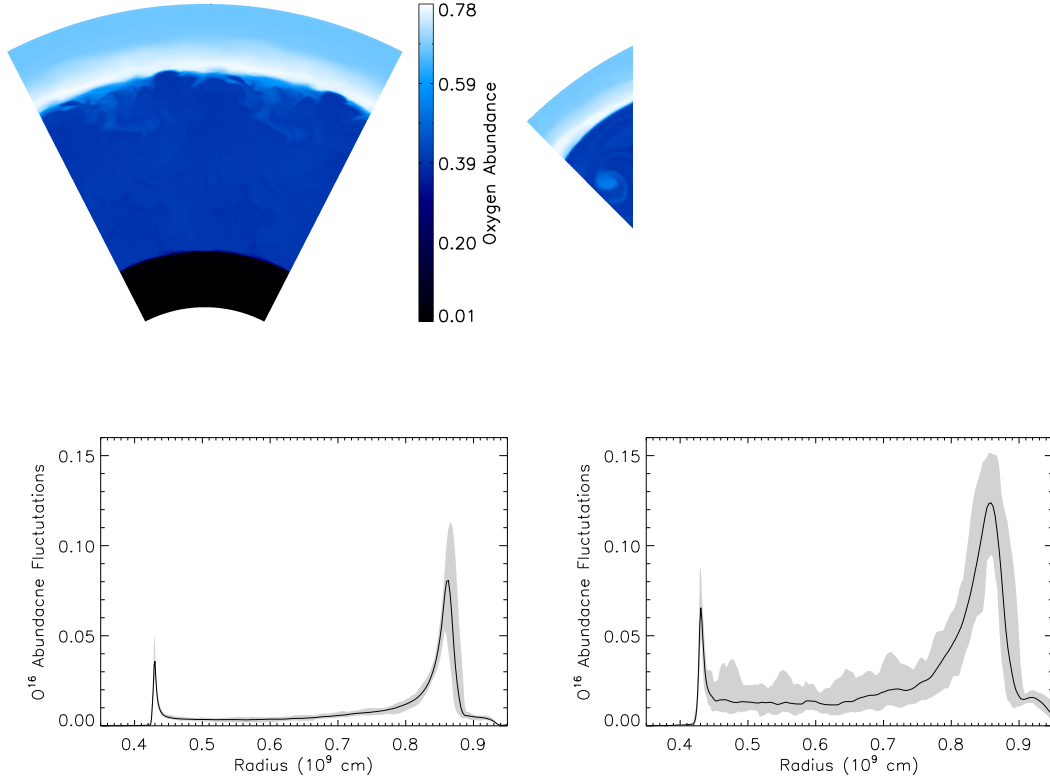


Figure 3.5: Spatial distribution of the oxygen mass fraction is shown for (left panels) the 3D compressible model and (right panels) the 2D compressible model. The spatial distribution is shown in the top row, and the time averaged RMS horizontal fluctuations are shown in the bottom row with the shaded region indicating extreme values of the fluctuations over two convective turnovers.

Table 3.1. Comparison of Oxygen Burning Models

Variable	Units	2D-PPM	3D-PPM	3D-Anelastic <sup>1</sup>
$M_*$ <sup>a</sup>	( $M_\odot$ )	23	23	25
$M_{in}, M_{out}$ <sup>b</sup>	( $M_\odot$ )	1.0(1.5), 2.7(2.4)	1.0(1.5), 2.7(2.4)	1.2, 2.3
$r_{in}, r_{out}$ <sup>b</sup>	( $10^9$ cm)	0.3(0.44), 1.0(0.85)	0.3(0.44), 1.0(0.85)	0.45, 0.84
$L_{net}$ <sup>c</sup>	(erg/s)	$3.2 \times 10^{46}$	$3.5 \times 10^{46}$	$1.5 \times 10^{45}$
$\Delta\theta, \Delta\phi$	(deg.)	90	30, 30	360, 180
Zones/Modes	( $n_r \times n_\phi \times n_\theta$ )	$400 \times 320 \times 1$	$400 \times 100 \times 100$	$145 \times 63(l) \times 31(m)$
$v_{max}$	( $10^7$ cm/s)	7.2	3.8	1.8
$\langle v_{conv} \rangle$	( $10^7$ cm/s)	2.0	0.8	0.49
$M_{peak}$	-	0.163	0.09	$\sim 0.04$
$M_{rms}$	-	0.03	0.01	$\sim 0.01$
$t_{conv}$	(s)	40	103	159
$t_{max}$	(s)	2400	800	6500
$\max\{ \rho'_c / \langle \rho \rangle \}$ <sup>d</sup>	$10^{-2}$	1.0(6.0) <sup>e</sup>	0.5	0.2
$\max\{ T'_c / \langle T \rangle \}$	$10^{-2}$	0.25	0.05	0.06
$\max\{ \rho'_b / \langle \rho \rangle \}$	$10^{-2}$	12.0	11.0	-
$\max\{ T'_b / \langle T \rangle \}$	$10^{-2}$	2.7	1.0	-

<sup>1</sup>The values quoted for the 3D anelastic model are from Kuhlen, Woosley, & Glatzmaier (2003).

<sup>a</sup>Zero age main sequence mass.

<sup>b</sup>Values in parentheses indicate the extents of the convection zone for the compressible models and the other values indicate the extents of the entire computation domain including the stable layers.

<sup>c</sup>The net luminosity for the compressible models,  $L_{net} = \int (\epsilon_{nuc} + \epsilon_{\nu\bar{\nu}}) dM$ , is estimated at  $t \sim 400$  s and is slowly decreasing with time due to an overall background expansion occurring within the burning region.

<sup>d</sup>The  $c$  and  $b$  subscripts indicate thermodynamic fluctuation amplitudes that are estimated in the convection zone and in the region of the convective boundary, respectively.

<sup>e</sup>The value in parentheses is the maximum density fluctuation estimated over two convective turnovers while the other value represents the time averaged maximum fluctuation. The significantly larger fluctuations seen in the 2D model compared with those in the 3D model occur near the center of large vortices which persist for several convective turnover times in the 2D model but are absent in the 3D convective flow.

## CHAPTER 4

### TURBULENT CONVECTION IN STELLAR INTERIORS

#### 4.1 Introduction

We have simulated three-dimensional (3D), turbulent, thermally-relaxed, nearly adiabatic convection (high Péclet number). Such flow is relevant to deep convective regions in stars (i.e., to most stellar mass which is convective, but not mildly sub-photospheric and surface regions). We simulate oxygen shell burning on its natural time scale, and core hydrogen burning driven at 10 times its natural rate. The simulations develop a robust quasi-steady behavior in a statistical sense, with significant intermittency. We analyze this statistical behavior quantitatively, and compare it to predictions of astrophysical mixing length theory (Böhm-Vitense, 1958). Mixing length theory (MLT) gives a good representation of many aspects of convection, but omits others (especially wave generation and mass entrainment) which are related to the dynamical behavior of stably stratified layers adjacent to the convection.

Section 4.2 briefly summarizes some results of the study of turbulent entrainment in geophysics, to prepare the reader for its appearance in our astrophysical simulations. This process is not included in the standard approach to stellar evolution (Cox & Guili, 1968; Clayton, 1983; Kippenhahn & Weigert, 1990; Hansen & Kawaler, 1994). In Section 4.3 I discuss our numerical and theoretical tools. In Section 4.4 I present our simulations of oxygen shell burning, which attain a thermal steady state (this is possible because of the rapidity of nuclear heating and neutrino cooling). In Section 4.5 I discuss a less advanced burning stage, core

hydrogen burning, which we are able to examine with the use of an artificially enhanced hydrogen burning rate (by a factor of ten). We find that the behavior is similar to the oxygen burning shell, suggesting that our results may have broad application for stellar evolution. In Section 4.6 I compare our results to the assumptions of MLT, and in Section 4.7 show that our results lead to a simple model of turbulent entrainment, an effect not in MLT nor in standard stellar evolutionary calculations.

This work is part of a larger project. Subsequent projects are planned in which the “empirical” convection model developed in this chapter will be integrated into the TYCHO stellar evolution code in order to assess its influence on stellar evolution, on nucleosynthetic yields, and on the structure of supernova progenitors.

## 4.2 Turbulent Entrainment

The presence of a turbulent layer contiguous with a stably stratified layer is common in both astrophysical and geophysical flows. Turbulence in a stratified media is often sustained by strong shear flows or thermal convection and bound by a stabilizing density interface. Over time, the turbulent layer “diffuses” into the stable layer and the density interface recedes, thus increasing the size of the mixed, turbulent region. The basic features of this *turbulent entrainment problem* are illustrated in Figure 4.1. The rate at which the density interface recedes into the stable layer  $u_E = \partial r_i / \partial t$  is called the entrainment rate, and its dependence on the parameters characterizing the turbulent and the stable layers has been the subject of numerous experimental and theoretical studies. It is generally ignored in stellar evolutionary studies.

Experimental studies have mostly been of “mixing box” type which involves

a tank of fluid with a turbulent layer and a density stratified layer. The turbulence is generated by thermal convection or an oscillating wire mesh, and density stratification imposed by either a solute or thermal gradient (Turner, 1980). Complementary to these shear-free mixing box models are shear driven-models. Shear-driven turbulence experiments involve either a recirculation track which propels one layer of fluid above a stationary layer, or a rotating plate in contact with the fluid that drives a circulation in the upper layer. Shear instabilities sustain a turbulent mixed layer in the overlying fluid which then entrains fluid from the lower, stationary layer (Kantha et al., 1977; Strang & Fernando, 2001). In all of these laboratory experiments, a variety of flow visualization techniques are used to study both the overall entrainment rate  $u_E$  and the physical mechanisms which underly the entrainment process.

One of the primary conclusions of these studies is that the entrainment rate depends on a Richardson number, which is a dimensionless measure of the “stiffness” of the boundary relative to the strength of the turbulence. In shear-free turbulent entrainment the bulk Richardson number,

$$Ri_B = \frac{\Delta b L}{\sigma^2}, \quad (4.1)$$

is most commonly studied. Here,  $\Delta b$  is the buoyancy jump across the interface,  $\sigma$  is the r.m.s. turbulence velocity adjacent the interface, and  $L$  is a length scale for the turbulent motions often taken to be the horizontal integral scale of the turbulence at the interface. The relative buoyancy is defined by the integral,

$$b(r) = \int_{r_i}^r N^2 dr \quad (4.2)$$

where  $N$  is the buoyancy frequency defined by,

$$N^2 = -g \left( \frac{\partial \ln \rho}{\partial r} - \frac{\partial \ln \rho}{\partial r} \Big|_s \right). \quad (4.3)$$

The entrainment coefficient  $E$  is the interface migration speed  $u_e$  normalized by the r.m.s. turbulent velocity at the interface  $E = u_e/\sigma$ , and is generally found to obey a power law dependence on  $Ri_B$ ,

$$E = A Ri_B^{-n}. \quad (4.4)$$

The exponent is usually found to lie in the range  $1 \lesssim n \lesssim 1.75$  and has been the subject of many theoretical studies of the entrainment process. Dimensional analysis suggests that  $Ri_B$  should be the controlling parameter, so long as microscopic diffusion plays a minor role (Phillips, 1966). Basic energetic arguments in which the rate of change of potential energy due to mixing is assumed to be proportional to the turbulent kinetic energy available at the interface leads to an exponent of  $n = 1$  (e.g. Linden, 1975). This same power law exponent has also been derived for models of the growth of the planetary boundary layer due to turbulent entrainment by penetrative convection (Stull, 1973; Tennekes, 1974; Stull, 1976a; Sorbjan, 1996).

The normalization of the entrainment coefficient  $A$  has been found to vary significantly between the various laboratory and field studies conducted, with recent values found in the range  $0.1 < A < 0.5$  (e.g. Stevens & Bretherton, 1999). The discrepancy among the normalization constants has been called the 'A-dilemma' (Bretherton et al., 1999). Experimental measures of the parameters in the entrainment law of equation 4.4 are tabulated in Fernando (1991) and a recent review of entrainment models used in the atmospheric sciences is discussed by Stevens (2002).

The experimental and theoretical models discussed above are generally moti-

vated by geophysical problems, but are directly relevant to the conditions found in stellar interiors. The bulk Richardson numbers which characterize stellar convective boundaries fall within the same parameter range ( $10 < Ri_B < 500$ ), and the background stratifications possess a similar buoyancy structure, so that it is interesting to learn from the geophysical models and compare to the stellar case.

### 4.3 The Numerical Tools

#### 4.3.1 1D Stellar Evolution

The hydrodynamic simulations which we studied in this chapter are of two distinct phases in the evolution of a  $23 M_{\odot}$  supernova progenitor: main sequence core convection, and convective oxygen shell burning. The initial conditions for the multi-dimensional simulations are taken from one-dimensional stellar models evolved with the TYCHO stellar evolution code. TYCHO (Young & Arnett, 2005) is an open source code<sup>1</sup>. A choice of standard 1D stellar evolution procedures is used. The mixing length theory as described in Kippenhahn & Weigert (1990) is used with instantaneous mixing of composition in the convectively unstable regions. The limits of the convection zones are determined using the Ledoux criterion, which incorporates the stabilizing effects of composition gradients. Semiconvective mixing has been turned off. Nuclear evolution is followed with a 177 element network using the rates of (Rauscher & Thielemann, 2000). Opacities are from Iglesias & Rogers (1996) and Alexander & Ferguson (1994) for high and low temperature regimes, respectively. The solar abundances of Grevesse & Sauval (1998) are used. Although more recent abundance determinations have been made (Asplund et al., 2005) the impact on the stellar structure of the models presented here is small, and minor variations in the abundances

---

<sup>1</sup><http://chandra.as.arizona.edu/~dave/tycho-intro.html>

have a negligible influence on the development of the hydrodynamic flow.

#### 4.3.2 Multi-Dimensional Reactive Hydrodynamics with PROMPI

The core of our multi-dimensional hydrodynamics code is the solver written by Fryxell, Müller, & Arnett (1989) which is based on the direct Eulerian implementation of PPM (Colella & Woodward, 1984) with generalization to non-ideal gas equation of state (Colella & Glaz, 1985). This code solves the Euler equations, to which I have added energy deposition by nuclear reactions and radiative diffusion through an operator-split formulation. The complete set of combustive Euler equations, including diffusive radiative transfer, can be written in state-vector form,

$$\frac{\partial \mathbf{Q}}{\partial t} + \nabla \cdot \mathbf{\Phi} = \mathbf{S}, \quad (4.5)$$

with the *state vector*

$$\mathbf{Q} \equiv \begin{bmatrix} \rho \\ \rho u \\ \rho E \\ \rho X_l \end{bmatrix}, \quad (4.6)$$

the *flux vector*

$$\mathbf{\Phi} \equiv \begin{bmatrix} \rho \mathbf{u} \\ \rho \mathbf{u} \mathbf{u} + p \\ (\rho E + p) \mathbf{u} + \mathbf{F}_r \\ \rho X_l \mathbf{u} \end{bmatrix}, \quad (4.7)$$

and the *source vector*



$$\mathbf{S} \equiv \begin{bmatrix} 0 \\ \rho \mathbf{g} \\ \rho \mathbf{u} \cdot \mathbf{g} + \rho \epsilon_{net} \\ R_l \end{bmatrix}, \quad (4.8)$$

where  $E = E_I + E_K$  is the total energy per gram consisting of internal and kinetic energy components, and  $\rho$ ,  $p$ ,  $\mathbf{u}$ ,  $\mathbf{g}$ , and  $T$  are the density, pressure, velocity, gravitational force field and temperature. The net energy source term due to nuclear reactions and neutrino cooling is  $\epsilon_{net} = \epsilon_{burn} + \epsilon_{cool}$ , and the time rate of change of composition  $X_l$  due to nuclear reactions is denoted  $R_l$ . The radiative flux is  $\mathbf{F}_r = -k_r \nabla T$ , with radiative “conductivity”  $k_r = 4acT^3/(3\kappa_R\rho)$  and Rosseland mean opacity,  $\kappa_R$ . Self-gravity is implemented assuming the interior mass at each radius is distributed with spherical symmetry. The mass interior to the inner boundary of the hydrodynamics grid is adopted from the TYCHO stellar model.

The stellar models, which are calculated on a finely meshed Lagrangian grid, are linearly interpolated onto the Eulerian hydrodynamics grid taking into account the sub-grid representation of mass used in the PPM scheme. Mapping the models leads to small discrepancies in hydrostatic equilibrium. An equilibration to hydrostatic balance occurs through the excitation and then damping of low amplitude, standing, predominantly radial pressure waves within the computational domain. These low amplitude waves, which are well described by the linearized wave equation, have a negligible affect on the convective flow.

To save computational resources, I simulate carefully chosen subregions of the star. Thus, these calculations are local models of convection in the *box in a star* tradition. The advantage of local convection models is that higher effective resolution can be used than is currently possible in global circulation models.

This approach, however, precludes investigation of the lowest order modes of flow, and we do not yet include rotation or magnetic fields which are best studied using global domains. The boundary conditions used are periodic in angular directions, and stress-free reflecting in the radial direction.

The simulation code, which I have dubbed PROMPI, has been adapted to parallel computing platforms using domain decomposition and the sharing of a three zone layer of boundary values and uses the MPI message passing library to manage interprocess communication.

#### 4.4 Oxygen Shell Burning

We have evolved a  $23 M_{\odot}$  stellar model with the TYCHO code to a point where oxygen is burning in a shell which overlies a silicon-sulfur rich core. Approximately 60% of the oxygen fuel available for fusion has been depleted at the time we begin the hydrodynamic simulation, when the star is  $\sim 2 \times 10^7$  yrs from the zero age main sequence. Carbon, helium, and hydrogen burning shells are also present contemporaneously at larger radii in the classic "onion skin" structure (Hoyle, 1946). In one of the models presented here (ob.2d.e), which was first introduced in chapter 2, an outer radius was used that encompasses both the oxygen and carbon burning shells. In this paper, however, I focus my analysis on the oxygen shell burning convection zone and the stable layers which bound it.

The oxygen shell burning model affords us the opportunity to study a thermally relaxed model because the thermal balance is determined by the very large neutrino cooling rates rather than the much lower radiative diffusion timescale (Arnett, 1996, ch.11). Neutrinos dominate the energy balance in the stable layers so that the stellar structure and the nature of convection are determined by the interplay between nuclear burning and neutrino emission (Aufderheide, 1993;

Arnett, 1972). The effects of radiative diffusion are both unresolved and energetically unimportant during these evolutionary phases, and have not been included in the oxygen shell calculations for computational efficiency.

The radial profile of the simulated region is presented in Figure 4.2. The temperature and density profiles betray the complex structure of the model, including the narrow burning shell that resides at the very base of the convection zone which is coincident with the temperature peak. The initial extent of the convection zone can be identified by the plateau in oxygen mass fraction at  $0.43 < r_9 < 0.72$  (where  $r_9 = r/10^9\text{cm}$ ). Characteristic of shell burning regions, the entropy gradient is quite steep at the boundaries of the convection zone and gives rise to peaks in the buoyancy frequency at those locations. The initial location of the upper convective boundary is coincident with a small stable layer at  $r \sim 0.72 \times 10^9\text{cm}$ , which is overwhelmed by the convective flow that develops in the simulation (see §4.4.1). A new boundary forms where the buoyancy frequency again becomes stabilizing at  $r \gtrsim 0.8 \times 10^9\text{cm}$ . This mixing is shown in the change in  $^{16}\text{O}$  abundance (Figure 4.2, top right) after 400s.

In Table 4.1 I list the 25 nuclei used in the network. This network reproduces to within 1% the energy generation of the full 177 element network used to evolve the one-dimensional TYCHO model for the simulated conditions, including oxygen and carbon burning shells. During carbon burning the dominant reactions are  $^{12}\text{C}(^{12}\text{C}, \alpha)^{20}\text{Ne}$  and  $^{12}\text{C}(^{12}\text{C}, \text{p})^{23}\text{Na}$ , leaving an ash of  $^{20}\text{Ne}$ ,  $^{23}\text{Na}$ , protons and alpha-particles.  $^{20}\text{Ne}$  is photodisintegrated through the  $^{20}\text{Ne}(\gamma, \alpha)^{16}\text{O}$  reaction. The dominant reactions during oxygen burning are  $^{16}\text{O}(^{16}\text{O}, \alpha)^{28}\text{Si}$ ,  $^{16}\text{O}(^{16}\text{O}, \text{p})^{31}\text{P}$ , and  $^{16}\text{O}(^{16}\text{O}, \text{n})^{31}\text{S}$ , leaving an ash of predominantly  $^{28}\text{Si}$  and  $^{32}\text{S}$ . Neglecting the non-alpha chain species  $^{23}\text{Na}$ ,  $^{31}\text{P}$  and  $^{31}\text{S}$  can affect the net energy generation rate during carbon and oxygen burning by a factor of a few under the conditions

studied here. The reaction rates, including  $^{12}\text{C}(\alpha, \gamma)^{16}\text{O}$ , are from Rauscher & Thielemann (2000).

Nuclear evolution is time advanced using the same reaction network subroutines as the TYCHO code and uses implicit differencing (Arnett, 1996). I include cooling by neutrino-antineutrino pair emission, denoted  $\epsilon_{cool}$ , which results from photo, pair, plasma, bremsstrahlung, and recombination processes (Beaudet et al., 1967; Itoh et al., 1996).

The Helmholtz equation of state code of Timmes & Swesty (2000) is used to represent the ion and electron pressure with an arbitrary degree of electron degeneracy. With our 25 nuclei network, the initial conditions are thermodynamically consistent with the initial TYCHO model to better than a few percent at all radii after mapping to the hydrodynamics grid.

I have calculated oxygen shell burning models in two and three dimensions. My baseline model, labeled ob.2d.c, is a  $90^\circ$  wedge embedded in the equatorial plane with radii encompassing the oxygen burning convective shell and two stable bounding layers. The effects of dimensionality on the oxygen burning convective shell are explored with a three-dimensional model ob.3d.B which has an angular extents of  $(27^\circ \times 27^\circ)$ . The influence of the upper boundary was studied with model ob.2d.e, which includes the overlying carbon burning convective shell as well (additional details concerning this model are presented in chapter 2). A preliminary resolution study is undertaken with model ob.2d.C which uses the same domain limits but twice the linear resolution of the baseline model. Properties of the oxygen shell burning models presented in this chapter are summarized in Table 4.2.

#### 4.4.1 The Correct Mixing Boundary

Convection is initiated through random low-amplitude (0.1%) perturbations in density and temperature applied to a region in the center of the convectively unstable layer on a zone by zone basis. (Two additional simulation models with the same characteristics as ob.2d.c were calculated which used perturbations with larger amplitudes (1%), and a low order mode distribution. The development of the convective flow was found to be insensitive to these differences.) The role played by the perturbations is to break the angular symmetry of the initial model, and seed rising and sinking plumes whose growth is driven by nuclear burning, neutrino cooling, and the slightly superadiabatic background gradient imprinted in the initial TYCHO model. As the plumes rise they penetrate the original convective boundary which was determined in the TYCHO code using the Ledoux criterion. The initial evolution of the flow is presented in a time series of snapshots in Figure 4.3; the light yellow contour shows the initial outer convective boundary.

The location of the initial outer boundary can be seen as a small bump in the initial profile of the buoyancy frequency presented in Figure 4.2 at radius  $r \sim .72 \times 10^9 \text{cm}$ . The reason the boundary is stable in the 1D model but did not survive in the multi-D simulation is because of the local nature of the Ledoux criterion used. This can be appreciated by the fact that although the buoyancy frequency at this location is positive, and hence locally stable to convective turnover, the *buoyancy jump* across this region is very small  $\Delta b \sim 3 \times 10^6 \text{ cm/s}^2$  compared to the turbulent kinetic energy in the adjacent flow, by which it is easily overwhelmed. This type of inconsistency can be relatively easily removed from 1D simulations by using a parameter akin to the bulk Richardson number (eq. [4.1]) to characterize convective boundaries in place of the Ledoux or Schwarzschild

criteria. For the original outer boundary  $Ri_B \lesssim 1$ , a condition under which a boundary is expected to mix on an advection timescale, akin to the expansion of turbulence into a homogenous medium.

The relationship between  $Ri_B$  and the traditional Schwarzschild and Ledoux criteria can be appreciated by writing the buoyancy frequency in terms of the well known "nablas" used in stellar evolution,

$$N^2 = \frac{g\delta}{H_P} \left( \nabla_{ad} - \nabla_s + \frac{\varphi}{\delta} \nabla_\mu \right) \quad (4.9)$$

where  $\nabla = (d \ln T / d \ln p)$ ,  $\nabla_s$  is the gradient of the stellar background,  $\nabla_{ad}$  is the gradient due to an adiabatic displacement,  $\nabla_\mu = (d \ln \mu / d \ln p)$  is the mean molecular weight gradient, and the thermodynamic derivatives are  $\delta = -(d \ln \rho / d \ln T)$  and  $\varphi = (d \ln \rho / d \ln \mu)$ . Therefore, the Ledoux criteria is simply,

$$N^2 > 0. \quad (4.10)$$

The Schwarzschild criteria is the same, but with the stabilizing effect of the mean molecular weight gradient  $\nabla_\mu$  neglected. For comparison, the bulk Richardson number can be written  $Ri_B \sim N^2 h L / \sigma^2$ , where  $h$  is some measure of the boundary width. A convective boundary will start to become stabilizing when,

$$N^2 \gtrsim \sigma^2 / (hL). \quad (4.11)$$

This criteria is based on a finite threshold for stability which takes into account the strength of the convective turbulence. Additionally, the bulk Richardson number is more than a simple stability criteria; it is also an indicator of the rate at which boundary erosion will proceed. I conclude that the correct criterion for determining the extent of a convective zone is neither the Ledoux nor the Schwarzschild criterion, which are both static, linear, and local criteria, but a *dynamic boundary*

*condition*, based on the bulk Richardson number, which I discuss in more detail in §4.7.

#### 4.4.2 Time Evolution

The rich dynamics taking place at the convective boundary are apparent in the time evolution of the 3D flow presented in Figure 4.4, which provides a global view of the evolution. The upper panel shows the evolution in time and radius of the oxygen abundance gradient, represented by a colormap in which light is large and dark is small. At the beginning of the simulation (far left) the colors are smooth as the turbulence has not yet developed. The light line near the bottom of the panel is the lower boundary of the convective shell, where oxygen is separated from the silicon-sulfur core below. The short horizontal band at  $r \sim 0.72 \times 10^9 \text{ cm}$  is the initial weakly stable convective boundary discussed above; it is overwhelmed in the first 100 seconds by convection. After  $\sim 300$  seconds the abundance distribution has approached a quasi-steady state, with slow growth of the convective region. The bottom of the convection zone moves downward, but at a much slower rate than the upper boundary moves outward. The mottled appearance in the convection zone is due to the ingestion of new oxygen entrained from above, followed by turbulent mixing. At the top boundary of the convection zone an oscillatory behavior can be seen, and in the overlying stable region wave motions are apparent.

The lower panel in Figure 4.4 shows the radial profile of the kinetic energy, which illustrates a major feature of the convection: intermittency. While these simulations are well described by a statistical steady state over a few convective turnover times, at any instant the fluctuations are significant. The flow is episodic, with bursts of activity followed by lulls. The bursts in kinetic energy in the convection zone are seen to induce wave trains in both the upper and lower

stable layers. Characteristic of g-modes, the phase velocity (orientation of the wave crests) is orthogonal to the group velocity (direction of energy transport) in these wave trains, which can be seen by comparing the composition and kinetic energy profiles.

#### 4.4.3 Quasi-Steady Oxygen Shell Burning Convection

Following the transient readjustment of the outer convective boundary, the oxygen burning convective shell attains a quasi-steady character. In Figure 4.5 I present the time evolution of the integrated internal, gravitational, and kinetic energy. The energy is calculated by forming horizontal averages of the flow properties and then assuming a full spherical geometry. The gravitational energy contribution from material on the computational grid is calculated according to,

$$E_G \equiv \int \frac{GM(r)dM}{r} dr, \quad (4.12)$$

where the mass increment is  $dM = 4\pi r^2 \langle \rho \rangle$ , and the integral is taken over the radial limits of the grid.

The total kinetic energy levels off in all of the models by  $t \sim 300$ s. The 2D models are characterized by a much larger overall kinetic energy. The total kinetic energy settles down to a slow increase as the oxygen shell evolves; this is true for both 2D and 3D.

The radial profile of the r.m.s. velocity fluctuations is presented in Figure 4.6 for the 2D and 3D models. The velocity fluctuation amplitudes in all of the 2D models are higher than the 3D model by a factor of  $\sim 2$ . The 2D models also assume a significantly different radial profile than the 3D model, with a flow structure that is dominated by large convective vortices which span the depth of the convection zone. The signature of these large eddies is apparent in the horizontal velocity components, as well as the fairly symmetric shape of the radial velocity



profile within the convection zone. The velocity components in the 3D model reveal an up and down flowing circulation with horizontal deflection taking place in a fairly narrow layer at the convective boundaries.

Although significant differences exist between 2D and 3D models, the 2D models are found to be in good agreement with each other to the extent that the statistics have converged, which are calculated over the time period  $t \in [300, 450]$ s. The time period for calculating statistics was limited by the model ob.2d.C, which was only run as far as  $t \sim 450$ s. The agreement among the 2D models shows that the outer boundary condition (tested by model ob.2d.e) and the grid resolution (tested by model ob.2d.C) are not playing a decisive role in determining the overall structure of the flow, at least in these preliminary tests. The agreement in overall velocity amplitude in the upper stable layer in model ob.2d.e indicates that the stable layer velocity amplitudes are not strongly affected by the details of the modes that are excited in that region. This gives credence to the analysis in chapter 3 which assumes that the stable layer velocity amplitudes are determined by the dynamical balance between the convective ram pressure and the wave induced fluctuations.

The convective turnover times  $t_c = 2\Delta R/v_{conv}$  for the 2D models are all of order  $t_c \sim 40$ s, and they span between 10 and 55 convective turnovers. The turnover time for the 3D model is  $t_c \sim 103$ s, and the model spans approximately 8 convective turnovers.

#### 4.4.4 Stable Layer Dynamics During Shell Burning

In both the 2D and 3D models, the stably stratified layers are characterized by velocity fluctuations throughout their extents (Figure 4.6). These fluctuations are the signature of g-modes excited by the convective motions. In the 2D model, the amplitudes of the stable layer velocity fluctuations are higher. In the lower

stable layer, the 2D models also have a much smaller ratio of horizontal to radial velocity amplitude. The velocity amplitude ratio is roughly proportional to the ratio of the mode frequency and buoyancy frequency,  $v_r/v_\perp \approx \omega/N$  (Press, 1981), so that the waves excited in the 2D model are of lower frequency. The velocity ratios in the upper stable layer are comparable between the 2D and 3D models, though the 2D amplitudes are higher by a factor of  $\sim 2$ .

During late burning stages, multiple concentric convective shells form which are separated by stably stratified layers. These intervening stable layers act as resonating cavities for g-modes that are excited by the turbulent convection. In chapter 2 it was shown that the stable layer motions in model ob.2d.e can be decomposed into individual g-modes that are well described by the linearized non-radial wave equation (§C). In chapter 3, I showed that a good estimate for the amplitudes of the wave motions (and the associated thermodynamic fluctuations) in both the 2D and 3D models can be made by assuming that the pressure fluctuations associated with the g-modes balance the ram pressure of the turbulent convection. In chapter 3, a single mode (frequency and horizontal scale) was assumed, based on integral properties of the turbulence (convective turnover time, and mixing length scale). Here, I present the spectrum of motions present in the stable layers and turbulent regions for the more realistic 3D model.

For a given background structure, a spectrum of eigenmodes exists which is a solution to the non-radial wave equation and boundary conditions. Individual modes can be uniquely identified by a horizontal wavenumber index  $l$  and oscillation frequency  $\omega$ . In Figure 4.7,  $l - \omega$  diagrams are presented for the convection zone, and the two bounding stable layers. The individual  $l - \omega$  components have been isolated through Fourier transforms of a time sequence of the simulation data.

Several modal components or “branches” can be identified in the stable layer diagrams (left and right panels). These include: (1) p-modes, seen as a series of points at the lowest  $l$  values that extend to high frequencies; (2) g-modes, which appear as ridges that are bound above by the buoyancy frequency; and (3) f-modes, which appears as a ridge separating the g- and p-modes. The  $f$ -modes are interfacial waves, and are most prominently seen in the lower-boundary diagram at a radius  $r = 0.4 \times 10^9$  cm. The f-mode signature is due to interfacial waves running along the convective boundary at  $r \sim 0.43 \times 10^9$  cm, where there is a spike in buoyancy frequency.

In the convection zone, the spectrum is dominated by power at low temporal and spatial frequencies. This strong non-modal convection signature is also present, though at lower amplitude, in the stable layers. This “turbulence” spectrum can be seen extending from the lower left corner of the diagrams. This same feature was also present in the simulations of He-shell burning by Herwig et al. (2006).

#### 4.5 Core Convection

Are the hydrodynamic features of oxygen shell burning of more general applicability? To investigate this, I examine core convection during hydrogen burning. Because of the long thermal time scale for radiative diffusion in such stars, I focus on the hydrodynamic behavior of a model in which the inner boundary provides a driving luminosity about ten times larger than natural. This allows us to simulate the convection with our compressible hydrodynamics code; an anelastic method (if multi-fluid) would allow this to be done in the star’s natural time scale. While our calculation is not thermally relaxed on a Helmholtz-Kelvin time scale, it does relax dynamically, and provides some clue as to the convective

behavior.

We have previously evolved a  $23\ M_{\odot}$  star onto the main sequence with TYCHO, to an age of  $2.4 \times 10^5$  yrs, at which point hydrogen is burning in a convective core. I then map this model onto the PROMPI hydrodynamics grid for simulation. This model represents an early point in main sequence evolution, in which the core hydrogen content has been depleted by only 1.7% ( $X_{core} = 0.689$ ,  $X_{init} = 0.701$ ,  $\Delta X = 0.012$ ). The inner radius of the simulation was chosen such that the convectively unstable region covers  $\sim 1$  pressure scale height (convective cores are usually only of order a pressure scale height because of the divergence of the scale height towards the stellar center). The entire domain covers  $\sim 5$  pressure scale heights and  $\sim 3.3$  density scale heights. The density contrast across the computational domain is  $\sim 30$  with a contrast of  $\sim 2$  across the convectively unstable region.

The radial profile of the simulated region is presented in Figure 4.8 including the run of temperature, density, composition, buoyancy frequency, and relative buoyancy. The entropy jump at the edge of the convective core, due to the fuel-ash separation, gives rise to a buoyancy jump (spike in buoyancy frequency).

The equation of state for the main sequence model is well described by an ideal gas with radiation pressure component. The ratio of gas to total pressure lies in the range  $0.85 < \beta < 0.95$ , with an increasing contribution from radiation pressure as the stellar center is approached. A single composition representing hydrogen has been evolved to keep track of nuclear transmutation and the mean molecular weight of the plasma. A metallicity of  $Z = 0.01879$  has been used to represent the additional 175 species in the initial TYCHO model and helium is calculated according to  $Y = 1 - (X + Z)$ , where  $X$  is the self-consistently evolved hydrogen mass fraction.

The luminosity due to nuclear burning in the computational domain is a small fraction of the total stellar luminosity (2.4%) which is dominated by burning in the inner regions of the core and  $L_{tot} = 7.8 \times 10^4 L_{\odot}$ . Core burning is incorporated into the simulation as an input luminosity at the inner boundary of the computational domain.

The Kelvin-Helmholtz timescale for this model is  $t_{KH} \sim 10^5$  years, which is many orders of magnitude longer than the dynamical timescales that are feasible to simulate. Additionally, the small luminosity of the star produces a convective velocity scale that is very subsonic ( $M \sim 10^{-3}$ ). Since we are not interested in the thermal relaxation of the model, we have boosted the input luminosity by a factor of 10 to increase the velocity scale of the flow. This was necessary because our fully compressible code is limited by the sound crossing time. (An anelastic or low-Mach number method would be ideal for simulating this core convection flow at the natural velocity scale.)

Radiation transport is treated in the diffusion limit. Opacities are approximated by Thompson scattering, which agrees well with the OPAL opacities (Iglesias & Rogers, 1996) used in the 1D TYCHO model for the region simulated. The effects of radiative diffusion, however, are found to be unresolved in the current simulation (with the diffusion time across a single zone  $\tau_{rad} = \Delta^2/k_{rad} \gg t_{conv}$ , with grid zone size  $\Delta$ ) and therefore energy transport in the convection zone occurs primarily on the subgrid level due to numerical diffusion. This is a high Péclet number simulation.

I have calculated a 2D and a 3D model. The simulated wedges have angular extents of  $\sim 30^\circ$  in both the polar and azimuthal directions and are centered on the equator to avoid zone convergence problems near the poles. This minimal angular domain size was chosen by calculating models of increasing angular size

in 2D domains until the flow pattern converged. The angular domain size used in the present simulations encompasses a large convective roll in 2D. Smaller 2D domains were found to distort the convective roll while domains larger by integer multiples contained proportionally more rolls of the same flow amplitude and morphology. The boundary conditions in the radial direction are reflecting and stress free, and periodic conditions are used in both angular directions. The grid zoning, domain limits, and simulation run times are summarized in Table 4.3 for the 2D and 3D models.

#### 4.5.1 Quasi-Steady Core Convection

Convection is initiated through random low-amplitude (0.1%) perturbations in density and temperature applied as in the oxygen shell simulation. In order to save computing time, the 3D model was initiated on a domain one-quarter as large in azimuthal angle which was then tiled four times in angle once convective plumes began to form. The initial development of the flow in the 3D model is presented in Figure 4.9 as a time sequence of velocity isosurfaces. The turbulent structure of the convective flow, as well as the excitation of internal waves which radiate into the overlying stably stratified layer, are clearly illustrated. A comparison of the flow morphology between the 2D and 3D models is presented in Figure 4.10. The 2D convective flow is much more organized and laminar, and is dominated by a single large convective cell while the 3D convection is composed of many smaller scale plume-like structures and is more obviously turbulent. In both models the stably stratified regions are rife with internal waves excited by the convection.

The 3D convective flow attains a quasi-steady character after approximately  $6 \times 10^5$  s, or approximately two convective turnovers. The evolution of the internal, gravitational, and total kinetic energy components on the computational grid

for the 2D and 3D models, are presented in Figure 4.11 and are calculated in the same way as for the oxygen burning model.

In both the 2D and 3D models, the total kinetic energy fluctuates in times with excursions from the mean as large  $\delta E_K / \overline{E_K} \sim 0.4$  in 3D and  $\delta E_K / \overline{E_K} \sim 0.6$  in 2D. The kinetic energy in the 2D model grows on a slightly longer timescale, and achieves a steady character after  $\sim 10^6$  s, at which time the kinetic energy growth rate tapers off. The total energy is conserved to better than  $\sim 0.2\%$  for both the 2D and 3D flows by the end of the calculation.

The r.m.s. velocity fluctuations are presented in Figure 4.12 for the 2D and 3D models. The resultant flows in both the 2D and 3D models are similar to those found for the oxygen shell burning model. The velocity amplitudes are higher in 2D by a factor of  $\sim 5$  (see axis scale in Figure 4.12), and the flows are dominated by large eddies spanning the depth of the convective region. The horizontal deflection of matter is also found to occur in a much narrower region in the 3D model. The hard-wall lower boundary of the 3D model is characterized by an even narrower horizontal flow, probably due to the absence of a stable layer which is host to g-modes.

The time averaged convective flow velocity for the 3D model is  $v_c \approx 2.8 \times 10^5$  cm/s. The turnover time is  $t_c = 2\Delta R / v_c \approx 3.2 \times 10^5$  s, and the simulation spans approximately 5 convective turnovers. The peak velocity fluctuation is  $v_{peak} \sim 2 \times 10^6$  cm/s, corresponding to a peak Mach number of  $M \sim 0.03$ , and the maximum density fluctuations within the convective flow are  $\sim 0.02\%$ , which is of order  $M^2$  as expected for low Mach number thermal convection (Gough, 1969). The time averaged convective flow velocity in the 2D model is  $v_c \approx 1.3 \times 10^6$  cm/s, and the convective turnover time for this model is  $t_c \approx 7 \times 10^4$  s. The simulation spans  $1.5 \times 10^6$  s which is  $\sim 21$  convective turnovers. The peak velocity fluctuation in

the 2D model is comparable to that in the 3D simulation, with  $v_{peak} \sim 2 \times 10^6$  cm/s and the peak density fluctuations is a little more than twice that found in the 3D model,  $\sim 0.05\%$ . The turnover times and convective velocity scales are summarized in Table 4.3.

#### 4.5.2 The Stable Layer Dynamics Overlying the Convective Core

As in the oxygen shell burning model, the stably stratified layers in the core convection models are characterized by velocity fluctuations throughout. Similar to shell burning, the 2D stable layer velocity amplitudes are larger and have a smaller radial to horizontal component ratio  $v_r/v_\perp \approx \omega/N$  compared to the 3D flow.

The stable layer motions in the core convection simulation are predominantly resonant modes, which compare well to the analytic eigenmodes of the linearized wave equation, and are analogous to those discussed for the oxygen shell burning model. The region outside the convective core will act as a resonant cavity, with the outer boundary at the location where the buoyancy frequency and Lamb frequency cross.

The amplitudes of the internal waves are determined by the ram pressure of the turbulence at the convective boundary. In Figure 4.13 the ram pressure and horizontal r.m.s. pressure fluctuations are presented for the 3D model, and can be seen to balance at the interface between the convective core and the stably stratified layer. Using this condition of pressure balance, we estimated the amplitudes of the excited internal wave velocities and the induced thermodynamic fluctuations and find this to be in good agreement with the oxygen shell burning simulations in chapter 3. The relationship between the density fluctuations, the convective velocity scale, and the stellar structure (i.e.,  $N$  and  $g$ ) was found to be,



$$\frac{\rho'}{\langle \rho \rangle} \sim M_c^2 + \frac{v_c N}{g}. \quad (4.13)$$

That this proportionality holds in the core convection model as well, where fluctuation amplitudes are lower than those in the oxygen shell burning model by an order of magnitude, is illustrated in Figure 4.14, which presents the buoyancy frequency and density fluctuation profiles for the boundary region. The measured density fluctuation and the value calculated according to equation 4.13 compare remarkably well, with  $\rho'/\langle \rho \rangle \sim 0.12\%$ .

#### 4.6 Simulations and Mixing Length Theory

In this section I compare our 3D oxygen shell burning simulation results to the mixing length theory of convection. I chose to compare this particular simulation since it represents the most physically complete model in our suite of calculations, both in terms of dimensionality and thermal evolution. Unless otherwise specified, the time period over which averaging is performed on the simulation data is  $t \in [400, 800]s$ , which is approximately 4 convective turnovers. I find that this period is sufficiently long compared to the time evolution of the flow that average values are not affected appreciably by increases in the averaging time period.

##### 4.6.1 Mixing Length Theory Picture

The basic picture underlying the mixing length theory, which is the standard treatment of convection used in one-dimensional stellar evolution modeling (see Cox & Guili, 1968; Clayton, 1983; Kippenhahn & Weigert, 1990; Hansen & Kawaler, 1994), is one in which large eddies are accelerated by an unstable temperature gradient and advect across a certain distance until they suddenly lose their identity by turbulently mixing with the *background*. Energy is transported through

this process because the envisioned turbulent *blobs* which are moving radially outward have a higher entropy at their formation location than the location in which they *dissolve*. The vertical extent over which large eddies retain their identity as they advect through a convection zone is a fundamental parameter in the mixing length theory. This *mixing length*  $\Lambda$  is generally taken to be a multiple of the local pressure scale height  $\Lambda = \alpha_\Lambda H_p$ .

Within this physical picture, the mixing length theory develops a relationship between the convective flux, the temperature gradient, the velocity scale, and the geometrical factors which describe the large scale eddies. The starting point in mixing length theory is the radial enthalpy flux, which is written in terms of fluctuations in the flow properties, and is taken to be (assuming a horizontally isobaric flow),

$$F_c = v_c \rho c_P T'. \quad (4.14)$$

The temperature fluctuations in mixing length theory are related to the temperature gradient and the distance traveled,

$$T'/T = \left( \frac{\partial \ln T_e}{\partial r} - \frac{d \ln T_0}{dr} \right) \frac{\Lambda}{2} = (\Delta \nabla) \frac{1}{H_p} \frac{\Lambda}{2} \quad (4.15)$$

where the subscript "e" indicates properties of the large convective eddies, the dimensionless temperature gradient  $\nabla$  is used (see §4.4.1), and the difference between the gradient in the eddy as it moves and the averaged stellar background is written,

$$\Delta \nabla = (\nabla - \nabla_e).$$

The factor of 1/2 in equation 4.15 represents the idea that on average the large

convective eddies have traversed about half a mixing length before reaching the current position. The velocity obtained by the convective eddy is computed by calculating the work done by the buoyancy force over a mixing length,

$$v_c^2 = g\beta(\Delta\nabla)\frac{\Lambda^2}{8H_p}. \quad (4.16)$$

Here again, the eddy is assumed to have been accelerated over half of a mixing length and an additional factor of 1/2 is incorporated on the right hand side to account for energy lost driving other flows, such as small scale turbulence and horizontal motions (e.g., note that the r.m.s. horizontal velocity is of the same order as the r.m.s. radial velocity in the simulation). The average convective flux can then be written,

$$F_c = \rho c_p T \sqrt{g\beta} \frac{\Lambda^2}{4\sqrt{2}H_p^{3/2}} (\Delta\nabla)^{3/2}. \quad (4.17)$$

The temperature gradient for the convecting material is found by assuming that eddies follow isentropic trajectories  $\nabla_e = \nabla_{ad}$ . Deviations from isentropic motion have been considered in the mixing length theory. In the case of strong radiative diffusion losses, the eddy geometry (in terms of the surface area to volume ratio) is an important additional parameter since the eddies are envisioned to *leak* a fraction of their thermal energy over a mixing length distance. When local cooling dominates, either through radiative losses (in optically thin regions) or neutrino losses (such as in the present model), the geometry of the eddies is not important since energy escapes everywhere from the large eddies, not just at eddy "surfaces".

During the oxygen shell burning simulations being considered here, non-adiabatic losses are small over a convective turnover time and the convection is expected to be "efficient". A quantitative measure of convective efficiency is the

Péclet number, which is the ratio of the energy loss timescale to the convective turnover timescale for the large eddies. In the current model, energy losses are dominated by neutrino cooling  $\epsilon_\nu$ . I calculate an effective Péclet number using the following convective and neutrino-cooling timescales:

$$\tau_c \sim \frac{H_p}{v_c} \quad (4.18)$$

$$\tau_\nu \sim \frac{c_p T'}{T' \partial \epsilon_\nu / \partial T} = \frac{c_p T}{\epsilon_\nu} \left( \frac{\partial \ln \epsilon_\nu}{\partial \ln T} \right)^{-1} \quad (4.19)$$

$$Pe = \frac{\tau_\nu}{\tau_c} \sim \frac{v_c c_p T}{H_p \dot{\epsilon}_\nu} \left( \frac{\partial \ln \epsilon_\nu}{\partial \ln T} \right)^{-1} \sim 10^4 \left( \frac{\partial \ln \epsilon_\nu}{\partial \ln T} \right)^{-1} \quad (4.20)$$

where characteristic values from the simulation have been used in equation 4.20, and the temperature dependence of the neutrino loss rates is  $(\partial \ln \epsilon_\nu / \partial \ln T) \lesssim 9$ . Therefore, the Péclet number for the convection is  $Pe \gtrsim 10^3$ , and we should expect the convection zone to be very nearly isentropic.

#### 4.6.2 The Enthalpy Flux, Background Stratification, and Temperature and Velocity Fluctuations

The convective enthalpy flux measured in the simulation is presented in Figure 4.15. The spike at the bottom of the convection region and the slight dip at the top reflect the braking of convective motion at these boundaries. The enthalpy flux is calculated by performing time and horizontal averages on the flow. Mixing length theory, however, makes the assumption that the velocity and temperature fluctuations are perfectly correlated, so that horizontal averaging of fluctuations is comparable to products of the averages. This is not necessarily true. To test the degree to which the velocity and temperature fluctuations are correlated I calculate the correlation coefficient,  $\alpha_E$ , which is defined in the following way:

$$F_c = \langle \rho c_p T' v'_c \rangle = \alpha_E \langle \rho c_p \rangle \langle T' \rangle \langle v'_c \rangle. \quad (4.21)$$

The fluctuations,  $T'$  and  $v'_c$  in equation 4.21 are taken to be the r.m.s. fluctuations in the simulation. The radial profile of  $\alpha_E$  is shown in Figure 4.15. We find  $\langle \alpha_E \rangle = 0.7 \pm 0.03$  averaged over the radial interval  $r \in [0.5, 0.75] \times 10^9$  cm within the convection zone. A value smaller than unity indicates that the horizontal distribution of temperature and velocity fluctuations in the flow are not perfectly correlated. The degree of correlation, however, is found to be fairly uniform throughout the convection zone.

I consider next how well the velocity and temperature fluctuations are correlated with the local temperature gradient. In Figure 4.16 the temperature gradient of the horizontally averaged hydrodynamic model profile  $\nabla_s$  as well as the adiabatic  $\nabla_{ad}$  and the composition-corrected (Ledoux) gradient  $\nabla_{Led} = \nabla_{ad} + \varphi/\beta \times \nabla_{\mu}$  are presented. The super-adiabatic temperature profile of the stellar background  $\Delta\nabla = \nabla_s - \nabla_{ad}$  is presented in the right panel of Figure 4.16. While the convection zone is found to have a super-adiabatic profile throughout, it is very small ( $\Delta\nabla \lesssim 10^{-3}$ ). This confirms the efficiency of the convection, in accord with our estimate for Pé. Stability is maintained in the upper boundary layer by the composition gradient,  $\nabla_{ad} < \nabla_s < \nabla_{Led}$ .

In order to assess the validity of the mixing length theory temperature and velocity fluctuation amplitudes given by equations 4.15 and 4.16 I calculate the correlation coefficients  $\alpha_T$  and  $\alpha_v$  which are defined by,

$$T'/T = (\Delta\nabla)\alpha_T \quad (4.22)$$

and

$$v_c = \frac{\alpha_v}{2} \sqrt{g\beta(\Delta\nabla)H_p}. \quad (4.23)$$

An important question concerns how to interpret and measure the temperature and velocity fluctuations  $T'$  and  $v_c$  in the simulations for comparison to mixing length theory. In the mixing length theory, these fluctuations are identified with the properties of large eddies. Therefore, a direct comparison would entail isolating the large eddies from the rest of the flow, and measuring their properties. In lieu of this complicated procedure I identify the fluctuations in the large eddies with two distinct quantities for comparison: (1) the r.m.s. fluctuations in the flow; (2) the difference between the horizontally averaged background value and the mean values in the up and down flowing material.

The temperature fluctuations calculated using these two methods are presented in Figure 4.17. The temperature fluctuations in the convection zone follow a trend similar to the super-adiabatic gradient, i.e., decreasing with increasing radius. In the right panel of Figure 4.17 the radial profile of  $\alpha_T$  is shown using both definitions of the fluctuations. The nonzero temperature fluctuations outside the convective region are due to distortions in stable layers due to convective buoyancy braking (chapter 3); the use of separate up and down flows is cleaner, eliminating these. The slope in the temperature fluctuation profiles are slightly overcompensated for by the super-adiabatic gradient when forming the ratio  $\alpha_T$ . Within the scatter, however,  $\alpha_T$  is fairly well represented by a constant value. The mean value within the body of the convection zone (taken to be  $r \in [0.5, 0.75] \times 10^9$  cm) is larger for the r.m.s. fluctuations  $\langle \alpha_T(\text{rms}) \rangle = 0.73$  compared to  $\langle \alpha_T(\text{up}) \rangle = 0.45$  and  $\langle \alpha_T(\text{down}) \rangle = 0.40$ . The largest departures from the mean, within the convective region, occur at the base of the convection zone,  $r \lesssim 0.52 \times 10^9$  cm, where the nuclear flame is driving the convective flow. The

departures are also large at the top, in the region of buoyancy braking.

The corresponding analysis for the velocity fluctuations is presented in Figure 4.18. The overall trends are similar for  $\alpha_T$  and  $\alpha_v$ . The mean values of  $\alpha_v$  within the body of the convection zone are  $\langle\alpha_v(\text{rms})\rangle = 1.22$ ,  $\langle\alpha_v(\text{up})\rangle = 1.08$ , and  $\langle\alpha_v(\text{down})\rangle = 0.96$ . The largest departure from constancy is again found to be at the base of the convection zone (the flame region).

The sharp decrease in the effective mixing length near the lower boundary is not entirely surprising. The distance to the convective boundary provides an upper limit to the mixing length, while further away from the boundaries the mixing length is limited by the distance over which eddies can maintain their coherence. This effect is possibly more exaggerated at the lower boundary because of the steep gradient in velocity which is needed to move the energy out of the burning zone. In contrast, the upper boundary is characterized by a more gentle deceleration of material and a "softer" boundary (i.e., lower  $N^2$ ). Ignoring this boundary effect and using the same mixing length parameter throughout the convection zone would result in a shallower temperature gradient near the boundary. The stiff temperature dependence of the nuclear reaction rates may therefore be affected.

The absolute calibration of  $\alpha_T$  and  $\alpha_v$  are somewhat arbitrary, and are scaled by factors of order unity for a particular implementation of the mixing length theory based on the heuristic arguments discussed above. According to equations 4.15, 4.16, 4.22, and 4.23 the equivalencies are  $\alpha_{\Lambda,T} = 2 \times \alpha_T$  and  $\alpha_{\Lambda,v} = \sqrt{2} \times \alpha_v$  where the values subscripted by  $\Lambda$  indicate the mixing length theory values defined by Kippenhahn & Weigert (1990). The corresponding values measured in the simulation are  $\langle\alpha_{\Lambda,v}(\text{rms})\rangle = 1.73$ ,  $\langle\alpha_{\Lambda,v}(\text{up})\rangle = 1.53$ , and  $\langle\alpha_{\Lambda,v}(\text{down})\rangle = 1.35$ , for velocity fluctuations; and  $\langle\alpha_{\Lambda,T}(\text{rms})\rangle = 1.46$ ,  $\langle\alpha_{\Lambda,T}(\text{up})\rangle = 0.9$ , and

$\langle \alpha_{\Lambda,T}(\text{down}) \rangle = 0.8$  for temperature fluctuations.

The ratios  $\alpha_{\Lambda,T}/\alpha_{\Lambda,v}$  are 0.84, 0.59, and 0.60 for the r.m.s., up-flow, and down-flow values, respectively. In relation to the present simulation, a higher degree of consistency (i.e.,  $\alpha_{\Lambda,v} = \alpha_{\Lambda,T}$ ) can be brought to this implementation of the mixing length theory by scaling the velocity fluctuation in equation 4.16 by the inverse of the ratio  $\alpha_{\Lambda,T}/\alpha_{\Lambda,v}$ . Physically, this translates into a higher efficiency (by a factor  $\sim 1.2 - 1.7$ ) for the buoyancy work to accelerate the large eddies over the value of  $1/2$  adopted above, which is reasonable considering the heuristic argument used. Alternatively, agreement can be made by scaling the temperature fluctuations in equation 4.15 by the same ratio, which amounts to decreasing the distance over which eddies remain coherent and adiabatic as they move across the convection zone. Both of these effects are plausible, as well as a combination of the two so long as the ratio is maintained. Which is operating in the present simulation? Unfortunately, the degeneracy between these two parameters cannot be broken because they combine linearly when calculating the enthalpy flux, which therefore does not provide a further constraint. Finally, *it is possible that the effective mixing lengths for temperature and velocity fluctuations are different*, a notion that is supported by the correlation lengths which we discuss next.

#### 4.6.3 Correlation Length Scales

In the top two panels of Figure 4.19 the vertical correlation length scales, calculated according to equation B.1, are presented for the velocity and temperature fluctuations. The vertical scale height is defined as the full width at half maximum of the correlation function, and can be written in terms of the correlation length in the positive and negative directions,  $L_V = L_V^+ - L_V^-$ . The relative values of  $L_V^+$  and  $L_V^-$  give an indication of asymmetries in the eddies (Figure 4.19, lower-left):  $L_V^+/L_V^- = 1$  is a symmetric eddy;  $L_V^+/L_V^- > 1$  is an eddy flattened on



the bottom; and  $L_V^+/L_V^- < 1$  is an eddy flattened at the top. Based on this simple diagnostic both the temperature and velocity correlations indicate that the eddies near the lower boundary are flattened on the bottom, and those at the upper boundary are flattened on the top. The "overshooting" distance ( $h \sim 10^7$  cm at the upper boundary and  $h \lesssim 10^6$  cm at the lower boundary), which is best described as an elastic response to the incoming turbulent elements, is very small compared to the correlation lengths measured here. Therefore, these eddies are effectively hitting a "hard wall" upon reaching the boundaries.

The signature of this eddy "flattening" is also present in the radial profile of the full width length scale,  $L_V$ . In the case of velocity, which has larger correlation length scales, significant asymmetries are present throughout the convection zone. The smaller length scales associated with the temperature fluctuations permit a broad region throughout the convection zone where the eddies are roughly symmetric ( $L_V^+/L_V^- \approx 1$ ) and appear to be uninfluenced by the boundaries. In this intermediate region, away from the boundaries, the temperature fluctuation length scales are relatively constant in size, even decreasing with radius, in contrast to the pressure and density scale heights which are increasing with radius.

In the standard mixing length theory, the sizes of convective eddies are assumed to be comparable to the size of the mixing length. How do the correlation length scales compare to the mixing length parameters found above? The lower left panel of Figure 4.19 shows the ratios of  $L_V$  to the pressure and density scale heights. None of these curves are particularly constant within the convection zone, and boundary effects are particularly strong throughout the convection zone in the case of the velocity correlations. Interestingly, the velocity correlation parameter  $\alpha_v(v_r, H_p) = L_V(v_r)/H_p$  is larger than the temperature correlation parameter  $\alpha_v(T', H_p) = L_V(T')/H_p$ . This is in accord with the ratio  $\alpha_{\Lambda, T}/\alpha_{\Lambda, v} < 1$

found in the mixing length analysis above. Concerning the absolute calibration, however, *the correlation length scales are smaller than the mixing length values by as much as a factor of a few*. In an analogous comparison by Robinson et al. (2004) for subgiant atmosphere models, the vertical correlation lengths were also found to be smaller than the mixing length used to construct the initial model, and the ratio varied significantly throughout the convection zone.

The horizontal correlation lengths  $L_H$  are shown in Figure 4.20 together with the vertical scales for comparison. For the velocity, the horizontal scale is much smaller than the vertical, indicative of eddies which are significantly elongated in the vertical direction. The temperature fluctuations appear to be much more symmetric, with only a small degree of elongation in the vertical direction which is slightly more pronounced near the top of the convection zone. In the stable layers, the horizontal scales are larger than the vertical, which is a characteristic of the horizontal “sloshing” motions associated with g-modes.

#### 4.6.4 The Kinetic Energy Flux, Flow Asymmetry, and Moving Beyond the Mixing Length Theory

The kinetic energy flux associated with convection is ignored in the mixing length theory since it arises from the *asymmetries* in the flow and MLT assumes that the flow is symmetric. An order of magnitude estimate for the kinetic energy flux, however, can be made:

$$\frac{F_K}{F_c} \sim \frac{\rho v_c^2 / 2}{\rho c_p T'} \frac{v_c}{v_c} \sim \frac{\alpha_\Lambda}{8} \frac{\beta P}{T \rho c_p} = \frac{\alpha_\Lambda}{8} \nabla_{ad} \sim 0.03 \quad (4.24)$$

where mixing length relationships have been used to calculate  $v_c$  and  $T'$ ,  $\alpha_\Lambda$  is assumed to be of order unity, and  $\nabla_{ad} \sim 0.25$  has been adopted from the simulation. This result tells us that the kinetic energy flux will be a few percent of the convective enthalpy flux. This estimate is an upper limit since up-flows and down-flows

will cancel to some degree (Böhm-Vitense, 1992, §6.1). In the simulation, the ratio of kinetic to enthalpy flux is found to be  $F_{K,max}/F_{c,max} \sim 0.01$ , which is of order the simple MLT scaling, but down by a factor of a few as expected.

We can directly relate the kinetic energy flux to the flow asymmetry in the following way. The upflow area covering fraction  $f_u = A_{up}/A_{tot}$  is shown in Figure 4.21. We can then write an estimate for the kinetic energy flux as,

$$F_{K,net} = \frac{1}{2}\rho_0(f_u v_u^3 - f_d v_d^3) \quad (4.25)$$

which can be written in terms of just the flow velocities,

$$F_{K,net} = \frac{1}{2}\rho_0 \left[ \frac{v_u^3 + v_d^3}{v_u/v_d + 1} - v_d^3 \right] \quad (4.26)$$

where we have used the mass conservation equation,  $f_u v_u + f_d v_d = 0$  assuming  $\rho_u \approx \rho_d$  which is a good approximation in these simulations. The kinetic energy flux in the simulation is shown in Figure 4.22. Shown by the thin line is  $F_K$  calculated according to equation 4.26, which is in good agreement. Here, I have used the horizontal and time averaged values for  $\langle v \rangle$  and  $\langle v^3 \rangle$ . The mixing length theory, however, does not provide information about  $\langle v^3 \rangle$ , but only  $\langle v \rangle$ . I overplot with the dashed line  $F_K$  calculated using  $\langle v \rangle^3$  in place of  $\langle v^3 \rangle$ ; it has to be scaled by a factor of 5 to fit the simulation data.

The scaling factor needed to calculate the kinetic energy flux is required to account for the skewness in the radial velocity field. More precisely, the correlation coefficient  $\chi = \overline{v_u^3}/\overline{v_u}^3$  is needed, which is related to the skewness  $\gamma = \overline{v^3}/\sigma_v^3$ . Both  $\chi$  and  $\gamma$  are presented in Figure 4.22. Note, that the skewness is a good proxy for the down-flow covering fraction ( $f_d = 1 - f_u$ ; see Figure 4.21), and therefore its sign is indicative of the direction of the kinetic energy flux.

Convective regions which are spanned by several pressure scale heights are

found to have kinetic energy to enthalpy flux ratios larger than a few percent as found in this study. For instance, the simulations of Cattaneo et al. (1991) and Chan & Sofia (1989) which each span  $\sim 5$  pressure scale heights achieve  $|F_K/F_c| \sim 35\%$ , and the domain in Chan & Sofia (1996) spanning  $\sim 7$  pressure scale heights achieves  $|F_K/F_c| \sim 50\%$ . A key result in the analysis of Cattaneo et al. (1991) is that the kinetic energy flux is dominated by coherent, downward-directed flows which are correlated over distances comparable to the simulation domain. Additionally, the enthalpy flux and kinetic energy fluxes associated with these down-flows essentially cancel with  $c_p T' \sim v_c^2$ , which was shown to follow if the down-flows can be described as Bernoulli streamlines.

The long range correlations just described, together with the boundary effects which dominate our shell burning model, undermine the basic mixing length theory picture of convection. The large coherence of the flows seen in these simulations, however, and present even in turbulent parameter regimes, suggest that modeling these *coherent structures* is a viable approach. Already, models incorporating multiple streams or “plumes” as closure models (e.g. Rempel, 2004; Lesaffre et al., 2005; Belkacem et al., 2006) are providing enticing alternatives to the mixing length theory.

#### 4.6.5 Related Studies

Although the mixing length parameters calculated above deviate from constancy near the convective boundaries, a mean value is a good approximation for most of the convection zone. It would be interesting if these parameters  $\alpha_E$ ,  $\alpha_T$ , and  $\alpha_v$  were universal, as assumed by mixing-length theory. If we restrict consideration to 3D compressible convection simulations for simplicity and homogeneity, there are several previous studies which have confronted mixing length theory to which we can compare our results. These studies investigate convection un-

der diverse conditions, including slab convection (Chan & Sofia, 1987, 1989, 1996; Porter & Woodward, 2000), a red giant envelope (Porter, Woodward, & Jacobs, 2000), and solar and sub-giant surface layers (Kim et al., 1995, 1996; Robinson et al., 2003, 2004, 2005). The number of zones used range from  $1.9 \times 10^4$  (Chan & Sofia, 1989) to  $6.7 \times 10^7$  (Porter & Woodward, 2000). The equations of state used include a gamma-law (Chan & Sofia, 1989; Porter & Woodward, 2000), ionized gas (Kim et al., 1996; Robinson et al., 2004), and a combined relativistic electron plus ion gas (Timmes & Swesty, 2000) in this paper. Subgrid scale physics was treated by a Smagorinsky model (Smagorinsky, 1963) or by ignoring it. We note that Styne, et al. (2000) have shown that PPM methods solving the Euler equations converge to the same limit as solutions to the Navier-Stokes equations, as resolution is increased and viscosity reduced. Additionally, the subgrid scale turbulence "model" implicit in the numerical algorithm of PPM is known to be well behaved (Fernando Grinstein, personal communication). Given this already inhomogeneous set of simulations, determining consistent convection parameters is difficult. My attempt is given in Table 4.4, in which I summarize the convection parameters found in these studies for comparison to our own.

How well do these compare? In some respects the agreement is striking. The parameter  $\alpha_E$  is in the range  $\sim 0.7 - 0.8$  for all groups. Further, all agree that for their case, the mixing-length theory gives a fairly reasonable representation of the simulations in the sense that the alphas are roughly constant throughout the body of the convection zone. The difficulty is that the specific values of these alphas depend upon the case considered. The two best-resolved simulations, ours and (Porter & Woodward, 2000), use the same solution method, PPM, yet have the most differing alphas. This suggests to us that the differences are due to the physical parameters of the respective convection zones. Porter, Woodward, &

Jacobs (2000) have already shown that slab and spherical geometry give qualitatively different behavior for the alphas. Our shell is only two pressure scale heights in depth, and is relatively slab-like; Porter & Woodward (2000) have a convection zone which is more than twice as deep by this measure. There is a suggestion in Table 4.4 that the alphas increase with the depth of the convection zone. This would be reasonable if a convective plume were accelerated through the whole convection region before it is decelerated at the nonconvective boundary. However, the other differences mentioned above probably contribute to the scatter in the alpha parameters in 4.4.

Further efforts on this issue are needed. If convection does depend upon the nonlocal, physical structure of the star, calibration of the mixing length to fit the sun, as is traditionally done, is not wise. Furthermore, it is well known that the mixing length theory is particularly prone to problems in the surface layers where convection becomes inefficient. Therefore, the empirical agreement of mixing length calibration to the sun and to Population II giants (Ferraro, et al., 2006) may be a fortuitous coincidence.

#### 4.7 Mixing At Convective Boundaries

The boundaries which separate the convective regions from the stably stratified layers in our 3D simulations span a range of relative stability, with  $1 \lesssim Ri_B \lesssim 420$ . At the lowest values of  $Ri_B$ , the boundary is quickly overwhelmed by turbulence, as described in §4.4.1. Once  $Ri_B$  becomes large enough, the boundary becomes stabilizing and evolves over a much longer timescale. Snapshots of the quasi-steady shell burning and the core convection boundaries are presented in Figure 4.23, ordered by  $Ri_B$  with spans the range  $36 \lesssim Ri_B \lesssim 420$ . The anatomy of the convective interfaces includes the turbulent convection zone, the distorted

boundary layer of thickness  $h$ , and the stably stratified layer with internal wave motions (compare to Figure 4.1).

The boundary becomes more resilient to thickening, and distortion by the turbulence as  $Ri_B$  increases. A region of partial mixing exists primarily on the turbulent side of the interface, where material is being drawn into the convection zone. The “ballistic” picture of penetrative overshooting (Zahn, 1991) in which convective eddies are envisioned to pierce the stable layer does not obtain. Instead, material mixing proceeds through instabilities at the interface, including shear instabilities and “wave breaking” events, which break the boundary up into wisps of material that are then drawn into the turbulent region and mixed. The convective interface remains fairly sharp in all cases, and the effective width is well described by the elastic response of the boundary layer to incoming eddies,  $h \sim v_c/N$ . The convective interfaces seen in our simulations bear a striking resemblance to those observed in laboratory studies of turbulent entrainment of comparable  $Ri_B$  (see e.g. McGrath et al., 1997, Figs. 2-5).

The mixing that occurs due to the instabilities and eddy scouring events at the interface leads to a steady increase in the size of the convection zone. In this section I quantify the entrainment rates at the convective boundaries, I discuss these results in terms of the buoyancy evolution of the interface, and I describe how the “turbulent entrainment” process can be incorporated into a stellar evolution code as a dynamic boundary condition to be used in addition to the traditional static Ledoux and Schwarzschild criteria. I conclude the section with some comments on numerical resolution.

#### 4.7.1 Quantifying the Boundary Layer Mixing Rates

As evident in Figure 4.23, the convective boundary layers are significantly distorted from spherical shells. To estimate the radial location of the interface we

first map out its shape in angle  $r_i = r_i(\theta, \phi)$ . At each angular position the surface is taken to be coincident with the radial position where the composition gradient is the steepest (this is comparable to the location of minimum density scale height  $H_\rho = [\partial \ln \rho / \partial r]^{-1}$ ). The interface thickness  $h$  is taken to be the r.m.s. variation of the surface  $r_i$  with angle,  $h = \sigma[r_i(\theta, \phi)]$ , which provides a quantitative measure of the amplitudes of the distortions imparted to the interface. The mass interior to the interface is calculated according to,

$$M_i = \int_{r_0}^{\langle r_i \rangle} 4\pi r^2 \langle \rho \rangle dr \quad (4.27)$$

where  $r_0$  is the inner boundary of the computational domain,  $\langle \rho \rangle$  is the horizontally averaged density, and the mean interface radius is used for the upper limit on the integral. The time derivative  $\dot{M}_i$  is the rate at which mass is entrained into the convection zone.

In Figure 4.24 the time histories of the averaged interface location  $\langle r_i \rangle$  and interfacial thickness  $h$  are shown for the convective boundaries in our simulations. A 3D model and a representative 2D model are shown for each boundary. The outer shell boundary layer adjusts rapidly in the first 100s to a new position, due to the penetration event discussed in §4.4.1, after which a slow outward migration ensues. For the 3D model, the outward migration proceeds in distinct stages, labeled (a - c) in Figure 4.24. Each stage is well described by a linear increase of radius with time, and ends with a rapid adjustment to a new entrainment rate. This behavior can also be seen in Figure 4.4, where the change in entrainment rate is coincident with changes in the background composition gradient and stability (compare to the initial buoyancy frequency profile in Figure 4.2).

The downward migration of the lower shell boundary is more uniform and proceeds at a significantly reduced rate compared to the upper boundary. The



core convection boundary evolution departs most significantly from a linear trend, but Monotonic growth is clearly established very soon after the simulation begins  $t \gtrsim 2 \times 10^5$ s.

The interfacial thickness  $h$  in the oxygen burning models are initially large, reflecting the strong mixing event during the initial transient, but settle down to relatively constant values for  $t \gtrsim 300$ s. In contrast, the boundary thickness in the core convection model increases gradually with time until a steady state value is achieved, reflecting the milder initial development. In all cases, the time averaged values of  $h$  during the quasi-steady states compare well to the boundary displacement expected for eddies impacting the stable layer with the characteristic convective velocities of the model,  $h \sim v_c/N$ .

The entrainment rate and the interfacial thickness is larger in all of the 2D models as a consequence of the larger velocity scales in those simulations. The interface migration rates and averaged interfacial layer thicknesses are tabulated for all of the models in Tables 4.5 and 4.6, and are broken down into various time intervals over which linear growth of the boundary is a good approximation. Time averaged mass entrainment rates are also included in Tables 4.2 and 4.3.

#### 4.7.2 The Entrainment Energetics

In order for entrainment to take place at a convective boundary the buoyancy increment of the stable layer material over that of the mixed layer material must be overcome. This can happen in two distinct ways. First, non-adiabatic processes can change the relative stability of the stable layer. For example, heating the convective region will cause an increase in its entropy, and the buoyancy jump separating the overlying layer will decrease. The rate at which the convective boundary will grow due to heating is  $u_s = \dot{s}/(\partial_r s)$ , where  $\partial_r s$  is the radial gradient of entropy at the boundary and  $\dot{s}$  is the time rate of change of entropy in the

shell. This process will cause both the upper and lower boundaries to migrate to larger radii – the upper boundary will be weakened, while the lower boundary will become stiffer. Non-adiabatic processes in the boundary layers will affect their stability in the same way: cooling in the upper and heating in the lower boundaries will weaken their stratification.

A related, but distinct process is “turbulent entrainment” whereby turbulent kinetic energy does work against gravity to draw material into the turbulent region. In this process, the stratification is weakened at a convective boundary by the turbulent velocity fluctuations. This is quantified in terms of the buoyancy flux  $q = g\rho'v'/\rho_0$ . In the absence of heating and cooling sources the buoyancy in the interfacial layers will evolve according to the buoyancy conservation equation,

$$\partial_t b = -\text{div}(q) \quad (4.28)$$

and a positive flux divergence at the boundary will lead to a weakening of the stratification. The relationship between turbulent entrainment and the weakening of a boundary through heating and cooling can be understood in terms of the enthalpy flux which attends the buoyancy flux. In fact, the buoyancy flux is directly related to the enthalpy flux across the interface,

$$F_c = \rho_0 c_p \langle T' v_r' \rangle = \frac{c_p T_0}{\beta} \langle \rho' v_r' \rangle = \rho_0 c_p \frac{T_0}{\beta g} \times q \quad (4.29)$$

and is equivalent to heating and cooling processes operating in the boundary layer (note the downward directed enthalpy flux within the boundary layers in Figure 4.15).

What drives the entrainment seen in the present simulations? Can the entrainment in the outer shell boundary be explained by the heating of the convection

zone by nuclear burning? Comparing the entropy growth rate of the shell to the entropy gradient at the boundary I find  $u_s \sim 0.8 \times 10^4$  cm/s, which is at most 17% of the measured growth rate for this boundary, and typically of order a few percent. Shell heating will reduce the growth rate of the lower boundary by  $u_s \sim 0.04 \times 10^4$  cm/s, which is of order a few percent of the rate measured. Therefore, the overall heating and cooling of the shell contributes very modestly to the growth of the shell over the course of the simulation. The long thermal timescale in the core convection model reduces this effect even more, where it is lower by several orders of magnitude. Therefore, I turn to the turbulent hydrodynamic processes operating in the boundary layer to understand the growth of the convection zones.

In Figure 4.25 I present the buoyancy flux profiles for our 3D simulation models, including both time-series diagrams and time averaged radial profiles. The properties of the buoyancy flux can be divided into three distinct flow regimes: (1) the body of the buoyant convecting layer, which is dominated by positive  $q$ ; (2) the convective boundary layers, with negative  $q$ ; (3) the stably stratified layers, where  $q$  is oscillatory, but has a nearly zero mean (in both a horizontal and time average sense).

The buoyancy driving of the convective flow in regime (1) can be appreciated by comparing the flow velocity to the commonly used buoyant convection velocity scale  $v_*^3 = 2.5 \int \langle q \rangle dr$ , where integration is taken over the radial extent of the convection zone (see e.g. Deardorff, 1980).  $v_*$  for the 3D shell burning and core convection models are  $v_* \sim 10^7$  cm/s and  $v_* \sim 3 \times 10^5$  cm/s, which compare well to the radial r.m.s. turbulent velocities measured in the simulation (Figures 4.6 and 4.12).

In regime (2), which occurs in the convective boundaries, the buoyancy flux

is negative. A negative value of  $q$  signifies that the turbulent kinetic energy is being converted into potential energy. The mixing that attends this negative buoyancy flux underlies the entrainment that is taking place at the boundaries through equation 4.28. We demonstrate this by showing that the entrainment speeds measured in the simulation are consistent with the measured buoyancy fluxes. The interface migration speed is incorporated into the conservation equation by writing the time derivative as an advective derivative,

$$\partial_t b \sim u_e \partial_r b = u_e N^2 \quad (4.30)$$

where I have used the relationship  $\partial_r b = N^2$ . Using this time derivative in equation 4.28 and solving for  $u_e$  I find,

$$\tilde{u}_e = \frac{\Delta q}{h N^2} \quad (4.31)$$

where I have approximated the divergence of the buoyancy flux with the difference  $\Delta q/h$ . I use the symbol  $\tilde{u}_e$  to distinguish the estimated rate from the values measured in the simulation.

If I adopt the buoyancy flux at the interface for  $\Delta q$  (Figure 4.25), the measured interface thickness  $h$ , and the buoyancy frequency at the boundary, I find the following entrainment rates. For the upper shell boundary, lower shell boundary, and the core convection boundary I have:  $\tilde{u}_e \sim 5.1 \times 10^4$  cm/s;  $\tilde{u}_e \sim 1.1 \times 10^4$  cm/s; and  $\tilde{u}_e \sim 2.2 \times 10^3$  cm/s, respectively. These are to be compared with  $u_e = |\dot{r}_i - v_{exp}|$  measured in section §4.7.1 and presented in Tables 4.5 and 4.6. The values corresponding to the same time period are:  $u_e = 4.6 \times 10^4$  cm/s;  $u_e = 1.2 \times 10^4$  cm/s; and  $u_e = 2 \times 10^3$  cm/s. Although these estimates are only order of magnitude (e.g., using the crude approximation for the time derivative in eq. [4.30]) they compare well to the values measured in the simulations and

the buoyancy flux due to “turbulent entrainment” can account for the growth of the convective layers seen here.

#### 4.7.3 Whence $q$ ?

The buoyancy flux  $q$  appears as a term in the turbulent kinetic energy (TKE) equation, which we present in §A.1 (eq. [A.12]). In our notation, the buoyancy flux is related to the buoyancy work term by  $q = \langle W_B \rangle / \rho_0$ . The buoyancy flux, therefore, is related to the rate at which turbulent kinetic energy is advected into the stable layer  $F_K$ , the rate at which it dissipates through viscous forces  $\varepsilon_K$ , and the rate at which energy is transported through the boundary layer by pressure-velocity correlations  $F_p$ . In essence, entrainment is the process by which the turbulent kinetic energy in the boundary layer does work against gravity to increase the potential energy of the overall stratification.

Two theoretical approaches have been taken to study entrainment. The first approach ignores the TKE equation and instead posits an “entrainment law”. The entrainment law is merely a functional form for the rate at which stable layer mass will flow into the turbulent region, and is therefore a dynamic boundary condition. These laws are usually parameterized by the stability properties of the interface and the strength of the turbulence through  $Ri_B$  (see e.g. Fedorovich, Conzemius & Mironov, 2004). Once an entrainment law is adopted, the enthalpy flux can be calculated and the evolution of the boundary can be self-consistently solved for. The advantage of such an entrainment law is the simplicity with which it can be incorporated into global circulation models of the atmosphere, for instance.

An alternative approach to adopting an entrainment law is an explicit physical model for the terms in the TKE equation (eq. [A.12]). For example, general forms for the buoyancy flux profile within the stable layer have been applied

with some success in reproducing the growth of the atmospheric boundary layer and the deepening of the oceanic thermocline (Stull, 1976b; Deardorff, 1979; Fedorovich & Mironov, 1995). In some respects, however, these models are glorified entrainment laws since the buoyancy flux is prescribed in a simplified, parameterized way. Moving beyond assumptions concerning the turbulence profiles within the interfacial layer, are theoretical models which take into account the interactions of waves and turbulence and incorporate non-linear models for the evolution of instabilities (e.g. Carruthers & Hunt, 1986; Fernando & Hunt, 1997). The approach adopted in these theoretical studies is general enough that any adjustable parameters may turn out to be universal and a predictive model can be developed. In addition, the framework employed is general enough that the production of turbulence by mean flows (i.e., stellar rotation) can be incorporated, as well as long-range effects due to internal waves. The internal waves are incorporated through the pressure-correlation flux,  $F_p$ , and plays a central role in the evolution of the buoyancy flux when wave breaking is important.

#### 4.7.4 An "Empirical" Entrainment Law

The development of a sophisticated turbulence model to explain entrainment is beyond the scope of the present work. Instead, we ask to what extent do the entrainment laws used in geophysical models apply to our simulations and stellar interiors? Guided by laboratory study and geophysical large eddy simulation I study the dependance of the entrainment rate on the bulk Richardson number.

$Ri_B$  is calculated according to equation 4.1, where I use the horizontal correlation length scale  $L = \mathcal{L}_H$  defined in §B. The buoyancy jump is calculated by performing the integration in equation 4.2 over the width of the interface which we take to be the interval  $r \in [\bar{r}_i - h, \bar{r}_i + h]$ . The normalized entrainment rates  $E = u_e/\sigma$ , the buoyancy jumps  $\Delta b$ , and  $Ri_B$  are presented in Tables 4.5 and 4.6.

The dependance of the entrainment coefficient  $E$  on  $Ri_B$  is presented in Figure 4.26.

The 2D and 3D data are found to obey similar trends (lower  $E$  for higher  $Ri_B$ ), but occupy significantly different regions of the diagram. This can be explained by the much higher r.m.s. velocities in the 2D simulation. The velocity scale in 2D is apparently an artifact of the reduced dimensionality of the problem which significantly influences the flow morphology. Although the velocity scale is higher in the 2D models, it is much more laminar and accompanied by less turbulent mixing. The arrow in Figure 4.26 indicates the direction that the 2D data points would move if a lower effective r.m.s. velocity were assumed. In what follows I focus the analysis exclusively on the entrainment data found for the more realistic 3D models.

What I find is that the entrainment coefficient  $E$  is well described by a power law dependance on  $Ri_B$  of the form in equation 4.4. The best fit values for the parameters are  $\log A = 0.027 \pm 0.38$  and  $n = 1.05 \pm 0.21$ . This entrainment law is shown by a dashed line in Figure 4.26. Remarkably, the power law is of order unity, in agreement with geophysical and laboratory studies. The fact that the entrainment in our simulations are governed by the same, fairly universal dependance on  $Ri_B$  as these other studies may have been anticipated, considering the striking degree of similarity between the buoyancy profiles and the character of the developed flow in the vicinity of the boundary (Figure 4.23).

#### 4.7.5 A Dynamic Convection Zone Boundary Condition

Mass entrainment is a fundamentally different phenomena from diffusion, which is the typical route used to incorporate new mixing phenomena into a stellar evolution code. Therefore, how might we incorporate this new process? Schematically, the idea is very simple. For each convective boundary, initially found with

the traditional stability criteria ( $\partial s / \partial r = 0$ ,  $\partial^2 s / \partial r^2 \neq 0$ ), we can calculate the associated bulk Richardson number based on the background stratification and an approximation of the turbulence characteristics (e.g., from MLT). With  $Ri_B$  in hand we can then input this into our entrainment law,  $E = E(Ri_B)$  which returns to us the entrainment rate. The entrainment rate, therefore, is the boundary growth rate as a function of  $Ri_B$  and possibly other parameters of the system. The function  $E(Ri_B)$  can be broken up into at least three regimes for convenience.

*Low stability:*  $Ri_B < Ri_B^{min}$ . For low  $Ri_B$  it is observed that mass entrainment happens very quickly, on an advection timescale (§4.4.1). Therefore, we can define a minimum  $Ri_B^{min}$  at which the expansion of the convection zone will proceed very quickly, eliminating convective boundaries which are too weak to support the adjacent turbulence.

*Intermediate Stability:*  $Ri_B^{min} < Ri_B < Ri_B^{max}$ . For an intermediate range of stability, we can use the fairly universal entrainment law which matches our simulation data, defined by the two parameters  $A$  and  $n$ . Although scatter in mixing rates were found to be as large as a factor of a few relative to the best fit law, the general monotonic, power-law dependance was found to be robust. We can incorporate this physics into the stellar evolution code as a mass entrainment rate,

$$\dot{M}_E = \frac{\partial M}{\partial r} u_E = (4\pi r_i^2 \rho_i) \sigma_H \times f_A \times 10^{(-n \log Ri_B)} \quad (4.32)$$

where the normalization factor is written  $f_A = 10^{(\log A)}$  and represents the turbulent entrainment mixing efficiency. More sophistication can subsequently be incorporated as our understanding of the entrainment process improves.

*High Stability:*  $Ri_B > Ri_B^{max}$ . The entrainment process will cease to operate at some upper limit  $Ri_B^{max}$ , above which the boundary evolution will be controlled by diffusive processes on the molecular scale. Following (Phillips, 1966), we have,



$$Ri_B^{max} \simeq \left(\frac{u_E}{\sigma}\right) \left(\frac{\sigma L}{\kappa}\right) \quad (4.33)$$

which is based on the condition that the kinetic energy in the turbulence is sufficient to lift the material from the interface,  $\rho\sigma^2 \gtrsim \rho N^2 \Delta^2$ . Here, the interface thickness is taken to be that due to molecular diffusion with  $\Delta \gtrsim \kappa/u_E$ . The relatively small diffusion rates in stellar interiors imply that turbulent entrainment will continue to operate to very high Richardson numbers. For comparison, the entrainment process in the ocean is estimated to operate up to  $Ri_B \sim 10^{5-6}$ .

Additional details concerning the implementation of this type of boundary condition into TYCHO will be presented in subsequent work on this subject, and is outside the scope of the present thesis.

#### 4.7.6 Spatial Scales, Numerical Resolution, and Entrainment

I conclude this section with a few comments on how well simulation can be trusted in elucidating the process of entrainment, which is not very well understood. The spatial scales which limit the entrainment rate at a convective boundary are also not well understood, and depend on the interplay between large eddy and small scale turbulent transport processes. As discussed by Lewellen & Lewellen (1998), there is feedback between the transport rate away from the turbulent boundary layer which is controlled by large eddies, and the transport rate of material in the immediate vicinity of the interface by small scale turbulence. A full understanding of this problem hinges on being able to resolve the entrainment zone in the presence of the large scale eddies.

A code comparison and resolution study of the entrainment problem in the planetary boundary layer context was conducted by Bretherton et al. (1999) and Stevens & Bretherton (1999). In these studies, it was suggested that the appropriate criteria for resolving boundary layer entrainment is that the grid zoning is

smaller than the fluctuations induced in the inversion layer by the large eddies so that shear instabilities (e.g., Kelvin-Helmholtz) would not be suppressed. It was suggested that a "nested grid" of refinement within the boundary layer was comparable to using fine resolution throughout the simulation domain. The suggested resolution criterion in these papers, however, fail to account for the non-linear turbulent evolution which proceeds the onset of instabilities. In addition, no simulations were conducted with enough resolution that the boundary layers were turbulent, and the simulations presented were even marginally resolved by the author's suggested criteria.

A related study by Alexakis (2004) investigates the entrainment and mixing at a boundary due to internal gravity wave breaking driven by a shear flow. This process may be operating in the shear mixing layers that form when large eddies impact the boundary layer. In this study, the mass entrainment rate was found to depend on the numerical resolution in a non-monotonic way, first decreasing and then increasing with finer resolution. The author concludes that low resolution models are dominated by numerical diffusion until the resolution is fine enough to resolve turbulence near the boundary, at which point the entrainment rate begins to increase and is controlled by turbulent transport. Although the asymptotic mixing rate was inconclusive and no resolution criteria was proposed, resolving the turbulence ensuing from the instability was shown to be important.

Much more work needs to be done to address the role played by both the small scale processes and the interplay with large eddies. Two complimentary numerical approaches can be taken. First, the feedback between large and small scale mixing and transport processes can be studied using large eddy simulation with a range of subgrid scale mixing efficiencies. Such a study can help develop insight into which scales control the mixing rate. Second, direct numerical sim-

ulations (DNS) which resolve the turbulent processes operating at the interface can be undertaken when sufficient computational resources are available. These studies would provide more definitive conclusions concerning the interplay between eddy scales and would provide guidance for a more general framework for future theoretical analysis. Finally, it is important to keep in mind that laboratory studies of high Reynolds number turbulent entrainment continue to provide useful constraints, and improved flow visualization techniques are allowing a more direct comparison to theory and simulation.

The "empirical" entrainment law which we discuss in this paper is constrained by only a few data points (the six 3D data points in Figure 4.26). Extending simulations to include an ever more diverse suite of stellar structures would provide an even stronger mandate, and better constrained model for incorporating this physics into stellar evolution codes.

#### 4.8 Summary And Conclusions

In this paper, I have presented the results of three-dimensional, reactive, compressible, hydrodynamic simulations of deep, efficient stellar convection zones in massive stars. Our models are unique in terms of the degree to which non-idealized physics have been used, and the evolutionary stages simulated, with fuel and ash clearly distinguished.

I find several general results regarding the basic properties of the convective flow:

- the flow is highly intermittent, but has robust statistical properties,
- the 2D vs 3D velocity scales differ by almost a factor of several, and the flow morphologies are completely different,

- stable layers interact with convection to decelerate plumes, and consequently distort these layers, which then generate waves,
- mixing is found to occur at convective boundaries in manner best described as turbulent entrainment, rather than the traditional picture of convective overshooting wherein turbulent eddies ballistically penetrate the stable layers.

I have compared our oxygen shell burning model to mixing length theory assumptions. I show that, while a reasonable representation of the super-adiabatic temperature gradient and velocity scale can be fit with a single mixing length, the values of the inferred mixing-length “constants” differ from other simulations. This was already implied in Porter, Woodward, & Jacobs (2000), who found difference for slab and spherical geometries. There may be a dependence upon the depth of the convection zone as well, and possibly upon the nature of the stable boundary regions and/or the nature of the driving process (burning or radiative loss).

Why do we care about MLT in regions of efficient convection? (1) the temperature profile can affect the burning rates, which have a stiff temperature dependence; (2) the velocity scale can affect the nucleosynthesis (such as s-process branching ratios in double shell burning AGB stars) by dictating the exposure time of the plasma to varying conditions throughout the burning region; (3) the velocity scale and the kinetic energy flux is an important input needed for calculating the mixing at convective boundaries.

I have found that the extent of mixing is better represented by an integrated Richardson number rather than the convectonal Schwarzschild or Ledoux criteria alone. This incorporates the addition physics related to the resistance of stiff boundaries to mixing. Related to the definition of boundary stiffness, we have

identified an important physical process which is missing from the standard theory of stellar evolution: turbulent entrainment. This process is well known in the meteorology and oceanographic communities, and has been extensively studied experimentally. It was shown that the rate of entrainment is well represented as a simple function of the buoyancy jump, in a manner similar to that determined experimentally.

The long term consequences of convective boundary inconsistencies such as the one illustrated by the initial transient in our simulation, and for which the conditions are common in 1D stellar models, can significantly alter the size of convective cores, and thus the subsequent explosion and nucleosynthetic yields of the resultant supernova. In subsequent work, case studies will be presented which incorporate the physical insight gained through these simulations into the TYCHO stellar evolution code. We expect to see effects in solar models, s-processing in AGB stars, stellar core formation (white dwarfs, neutron stars, and black holes), stellar nucleosynthesis yields, stellar ages, and HR diagrams.

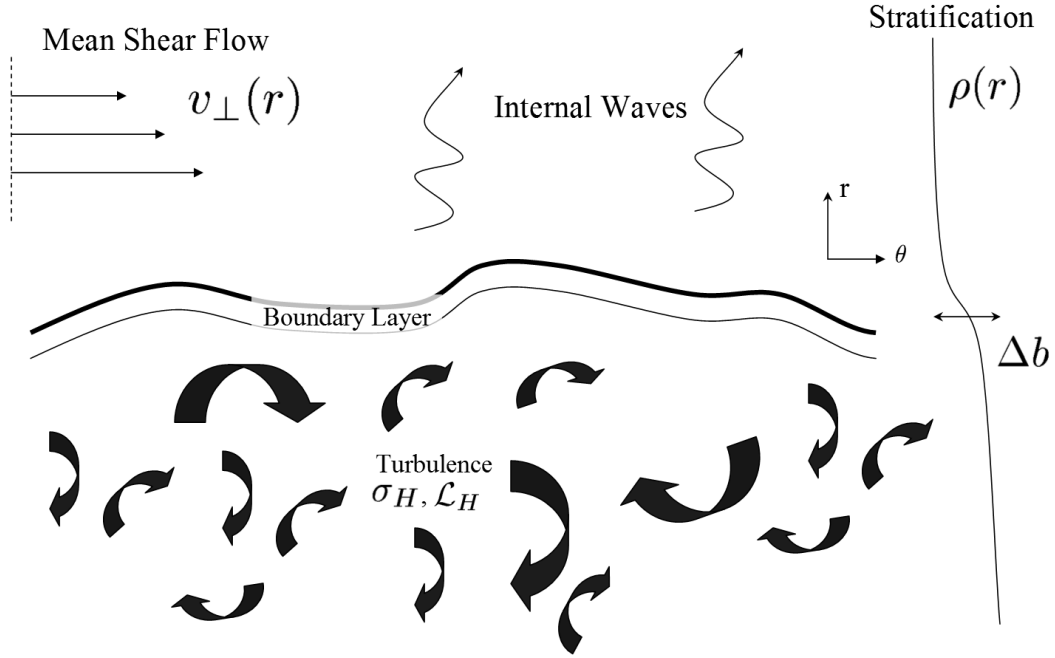


Figure 4.1: Diagram illustrating the salient features of the density and velocity field for the turbulent entrainment problem. Three layers are present: a turbulent convection zone is separated from an overlying stably stratified region by a boundary layer of thickness  $h$  and buoyancy jump  $\Delta b \sim N^2 h$ . The turbulence near the interface is characterized by integral scale and RMS velocity  $\mathcal{L}_H$  and  $\sigma_H$ , respectively. The stably stratified layer with buoyancy frequency  $N(r)$  propagates internal waves which are excited by the adjacent turbulence. A shear velocity field  $v_{\perp}(r)$ , associated with differential rotation, may also be present. After Strang & Fernando (2001).

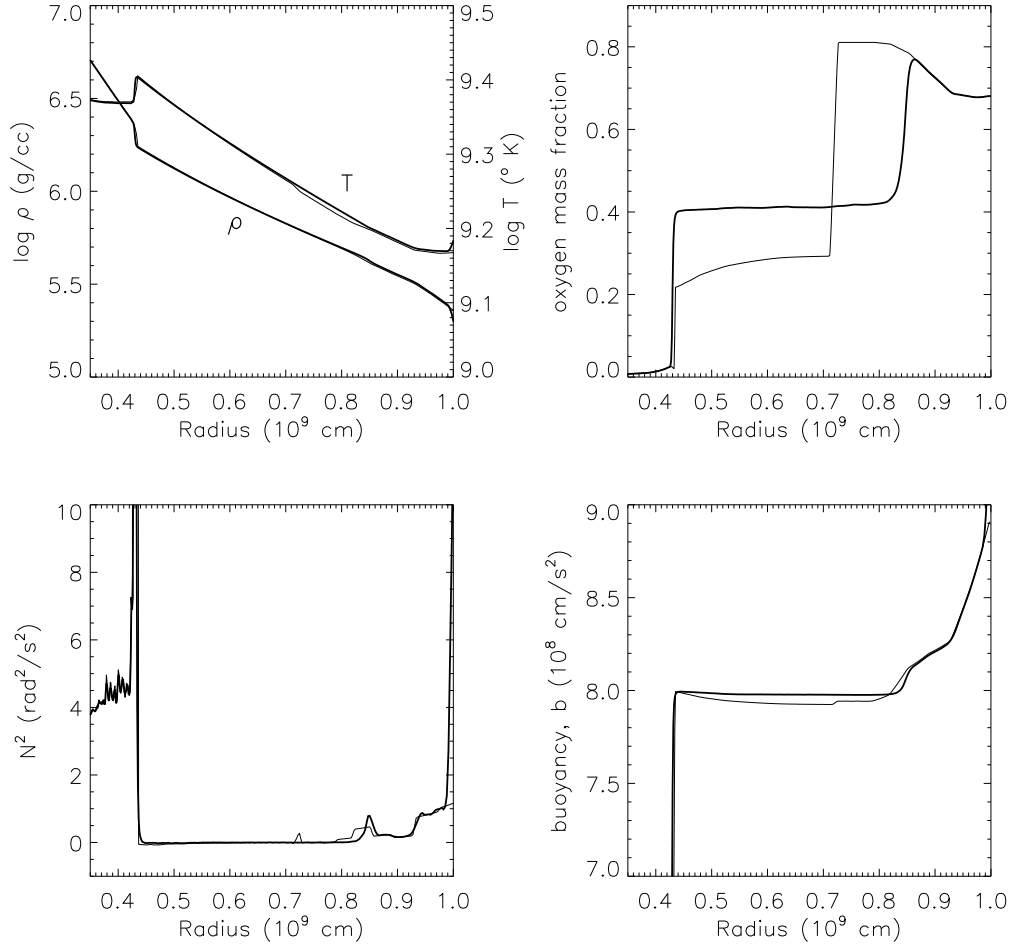


Figure 4.2: Radial profile of the simulated region for the oxygen shell burning models. The thin lines indicate the initial conditions and the thick lines indicate the 3D model at  $t = 400$  s. (top left) Temperature and density. (top right) Mass fraction of  $^{16}\text{O}$ . (bottom left) Squared buoyancy frequency. (bottom right) Buoyancy.

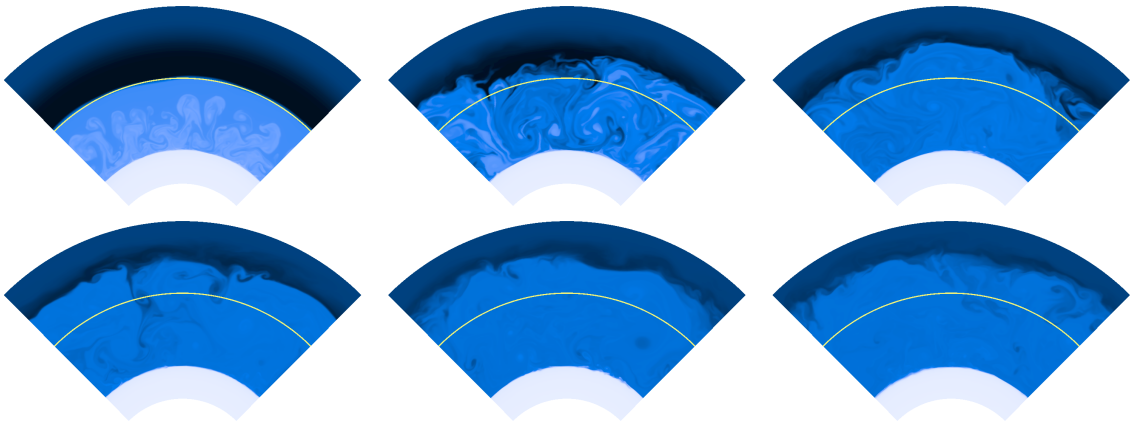


Figure 4.3: This time sequence shows the onset of convection in the oxygen shell burning model. The first 200 s of the 2D model (ob.2d.c) is shown, including the initial transient and the settling down to a new quasi-steady state. The light yellow line indicates the location of the convective boundary as defined in the 1D TYCHO stellar evolution model (Ledoux criterion), which was used as initial conditions for the simulation.



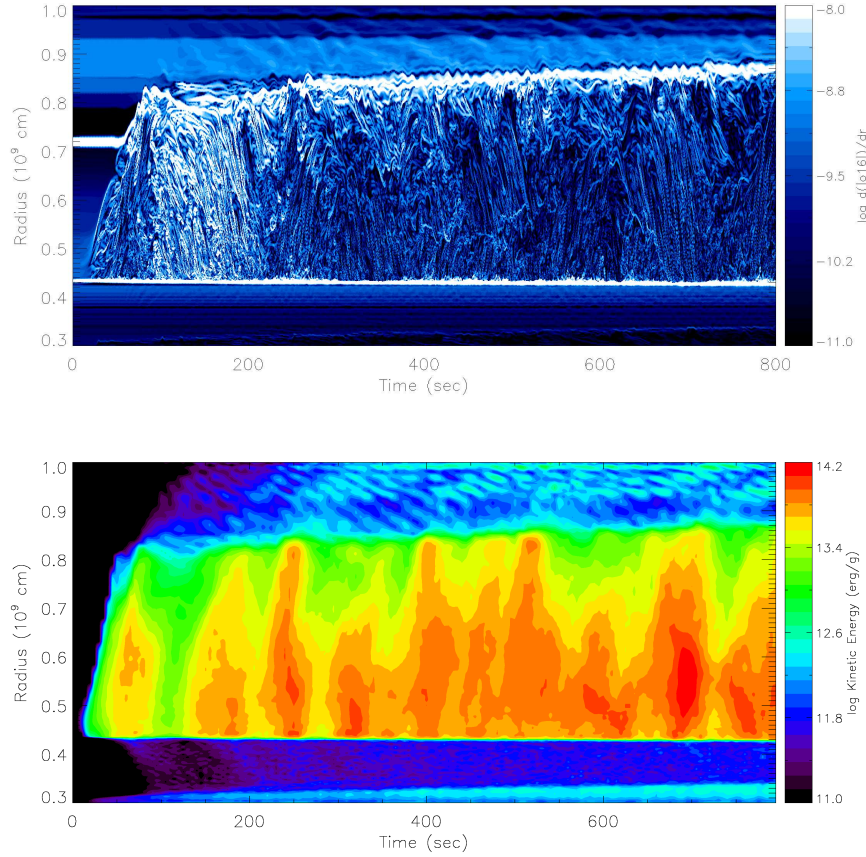


Figure 4.4: The time evolution of the 3D oxygen shell burning model. (top) The magnitude of the oxygen abundance gradient is shown and illustrates the migration of the convective boundaries into the surrounding stable layers. Interfacial oscillations are also apparent in the upper convective boundary layer ( $r \sim 0.85 \times 10^9$  cm), and internal wave motions can be seen quite clearly in the upper stable layer. (bottom) The kinetic energy density is shown, and illustrates the intermittent nature of the convective motions. The upwelling chimney-like features in the convective region are seen to excite internal wave trains in the stable layers, which propagate away from the boundaries of the convection zones. See also Fig. 4.25.

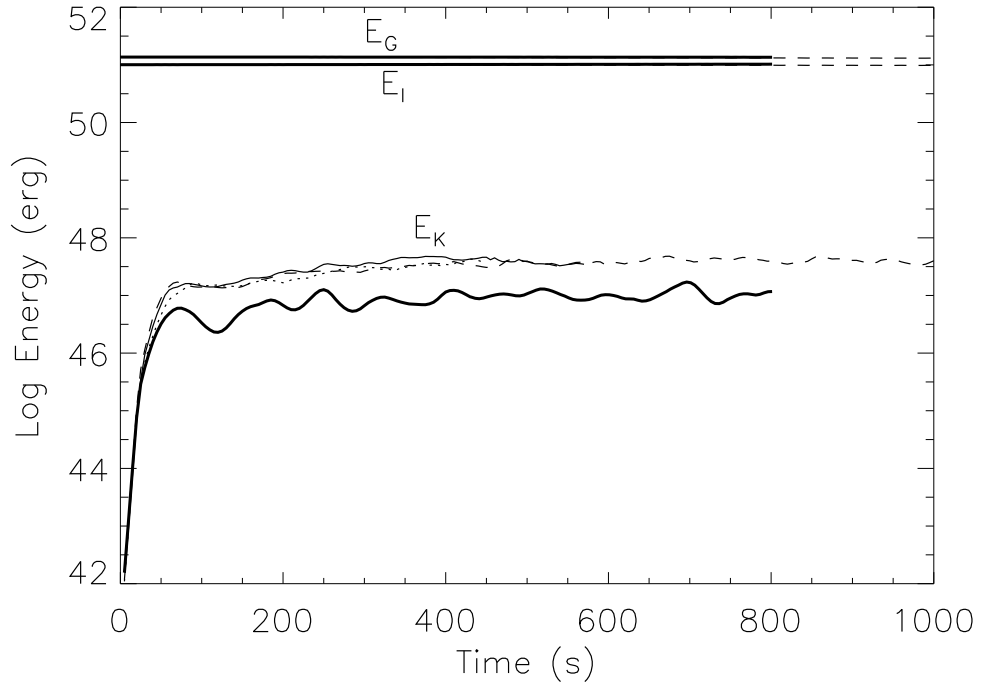


Figure 4.5: The time evolution of the energy budgets for the oxygen shell burning models: the (thick line) 3D model, and (thin lines) the three 2D models are shown, including: (thin-solid) ob.2d.c; (thin-dashed) ob.2d.e; and (thin dotted) ob.2d.C. The energy budget includes the internal energy  $E_I$ , the gravitational energy  $E_G$ , and the kinetic energy  $E_K$ . Note that the energy scale is logarithmic, so that the 3D kinetic energy is much smaller than the 2D values.

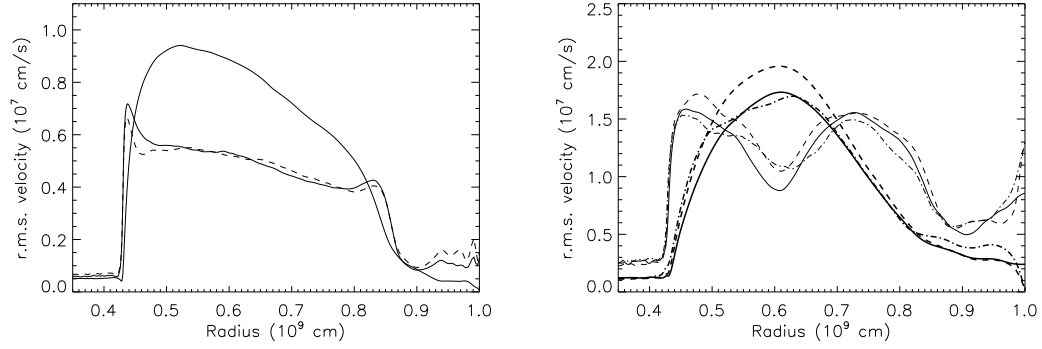


Figure 4.6: The r.m.s. velocity fluctuations for oxygen shell burning: (left) 3D model, with velocity components (thick-solid)  $v_r$ , (thin-solid)  $v_\theta$ , and (thin-dashed)  $v_\phi$ . (right) The 2D models, with velocity components (thick)  $v_r$  and (thin)  $v_\phi$  for simulations (solid) ob.2d.e, (dashed) ob.2d.c, and (dash-dot) ob.2d.C.

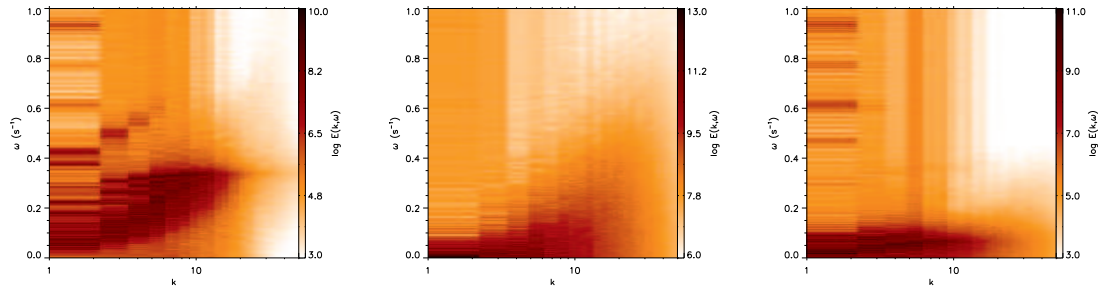


Figure 4.7: Mode diagrams for several radial positions in the oxygen shell burning model show the dominant spatial and time scales on which motions occur. The abscissa measures  $k$  which is related to the wavenumber index  $l$  of the mode by  $l = 12 \times k$ . The three locations shown here include: (left) Lower stable layer, just beneath the convective shell  $r = 0.4 \times 10^9$  cm. (middle) Middle of convective shell,  $r = 0.6 \times 10^9$ . (right) Upper stable layer, just above the convective shell  $r = 0.9 \times 10^9$  cm.

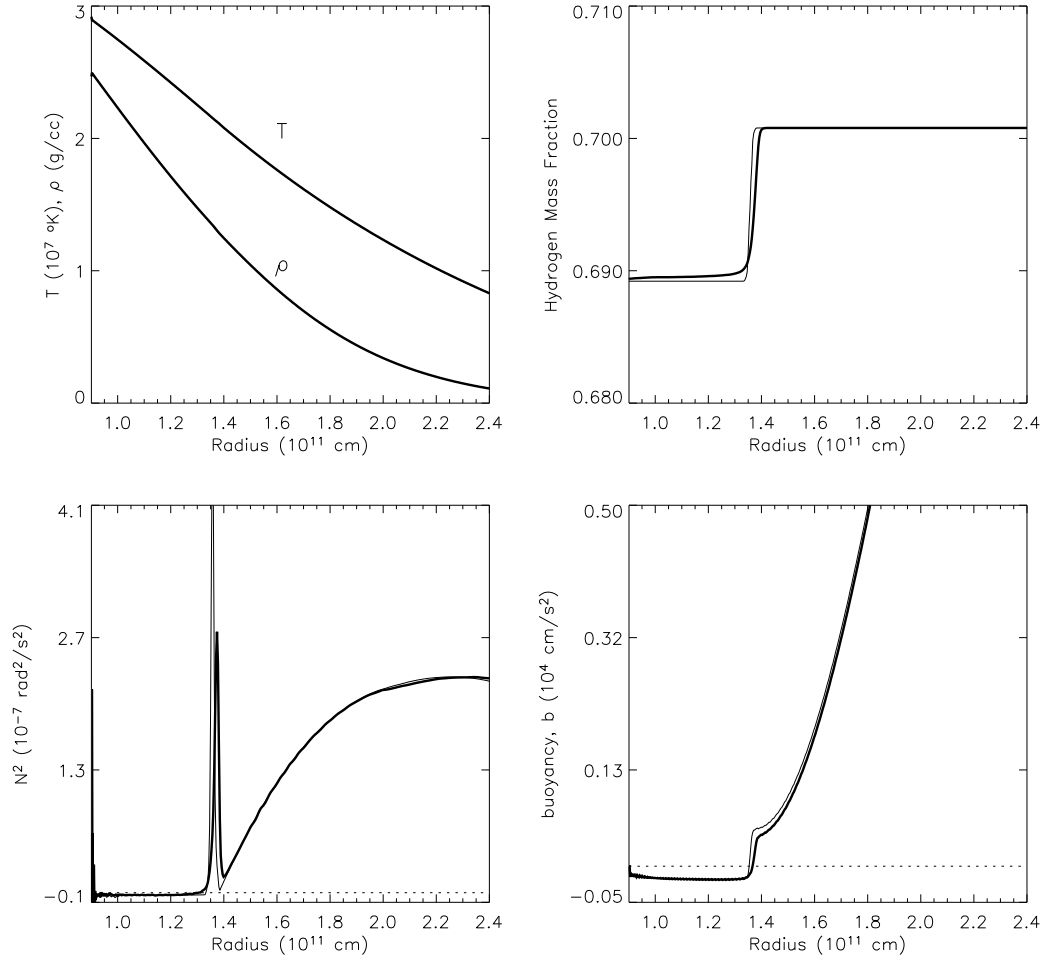


Figure 4.8: Radial profile of the simulated region for the main sequence core convection model. The thin lines show the initial conditions and the thick lines show the state of the 3D model at  $t = 10^6$  s. (top left) Temperature and density. (top right) Hydrogen abundance. (bottom left) Squared buoyancy frequency. (bottom right) Buoyancy.

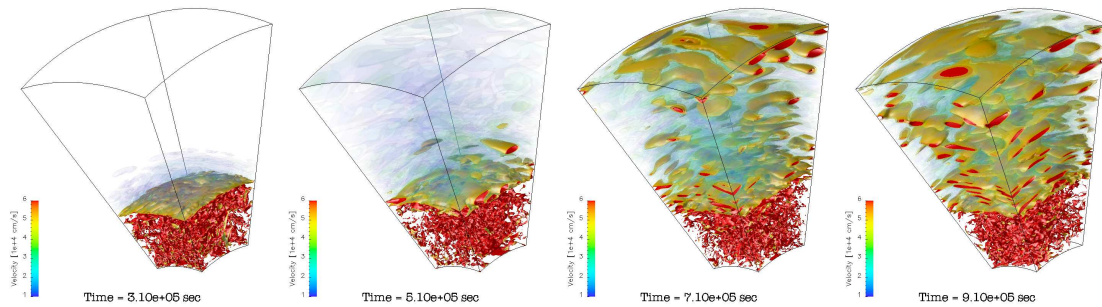


Figure 4.9: Velocity isocontours show the development of the flow in the 3D core convection model. The turbulent convective flow excites internal waves which radiate into the overlying stably stratified layer. By the end of the time sequence shown the stable layer cavity is filled with resonant modes.

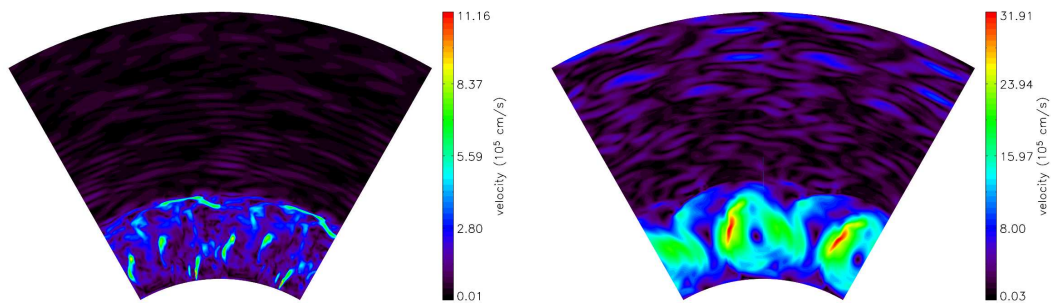


Figure 4.10: The velocity magnitude for the core convection model at  $t=10^6$  s: (left) a slice through the 3D model; and (right) the 2D model. The topology of the convective flow is significantly different between 2D and 3D models: the 3D convective flow is dominated by small plumes and eddies while the 2D flow is much more laminar, and dominated by a large vortical eddies which span the depth of the layer. The wave motions in the stable layer have similar morphology in 2D and 3D, but the velocity amplitudes are much larger in 2D. The computational domains have been tiled once in angle for presentation.

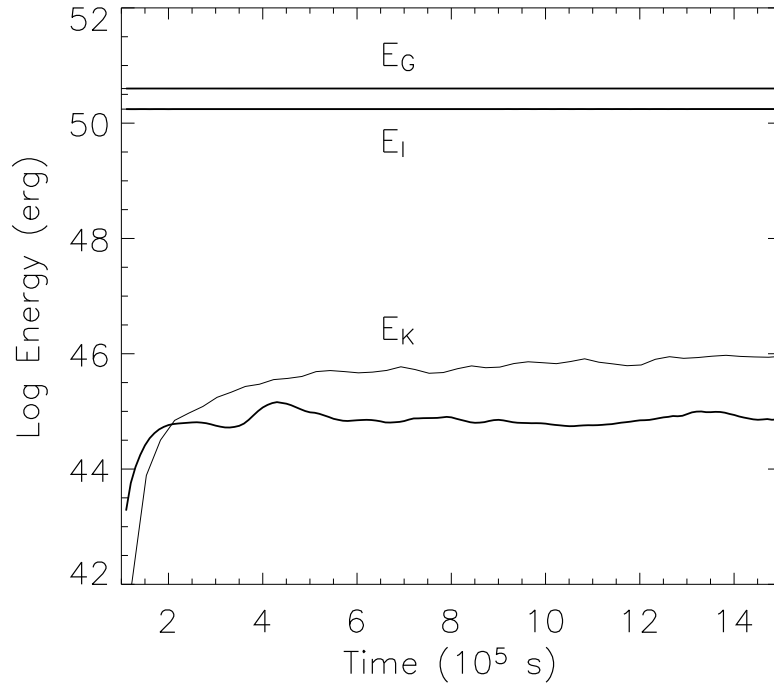


Figure 4.11: The time evolution of the energy budget for the main sequence core convection models: the (thick line) 3D model; and (thin line) the 2D model are shown. The energy budget includes the total internal energy  $E_I$ , gravitational energy  $E_G$ , and kinetic energy  $E_K$  on the computational grid.

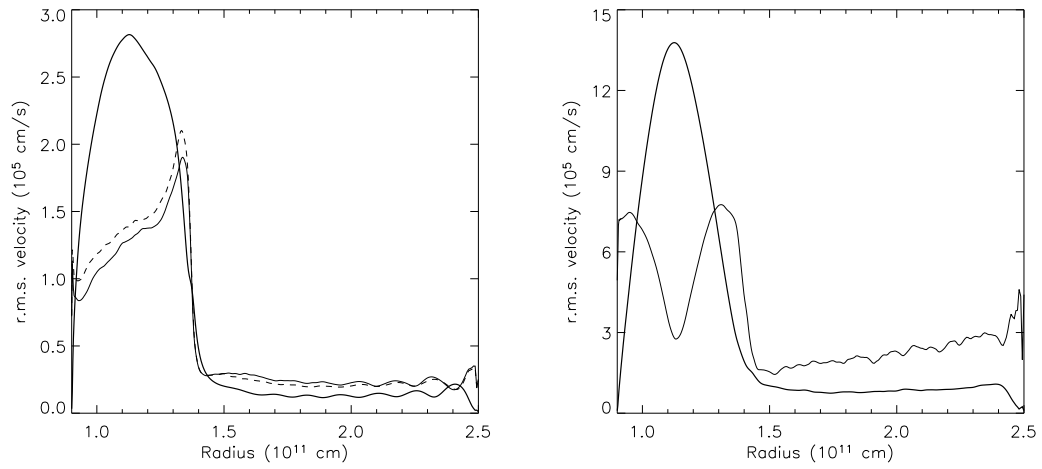


Figure 4.12: The r.m.s. velocity fluctuations for the core convection model: (left) the 3D model, and (right) the 2D model. In each plot, the thick line indicates the radial velocity component and thin line is used to indicate horizontal velocity components, with the dashed line used to show the polar angle component in the 3D model.

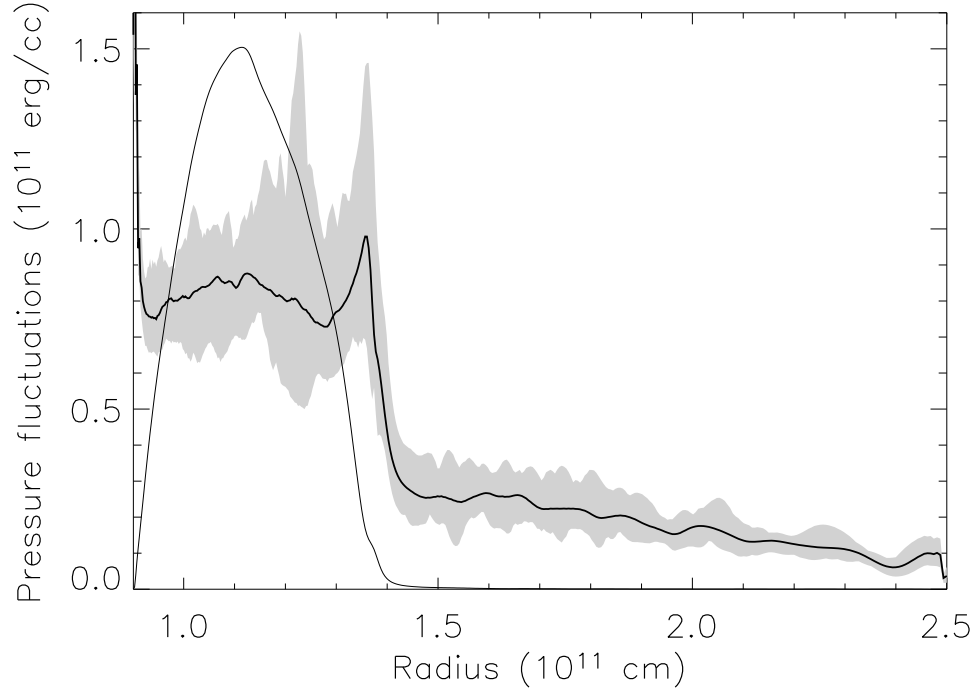


Figure 4.13: Pressure fluctuations in core convection model: The time averaged horizontal r.m.s. pressure fluctuations are shown as the thick line, with extreme values over two convective turnovers indicated by the shaded region. The thin line shows the radial component of the turbulent ram pressure  $\rho v_r^2$  averaged over a convective turnover. At the upper boundary, the curves cross at a point where the turbulent pressure is balanced by the wave induced pressure fluctuations in the stable layer. This crossing point is coincident with the location of the convective boundary. The pressure perturbations at the lower boundary are due to the input luminosity which drives the convective flow.



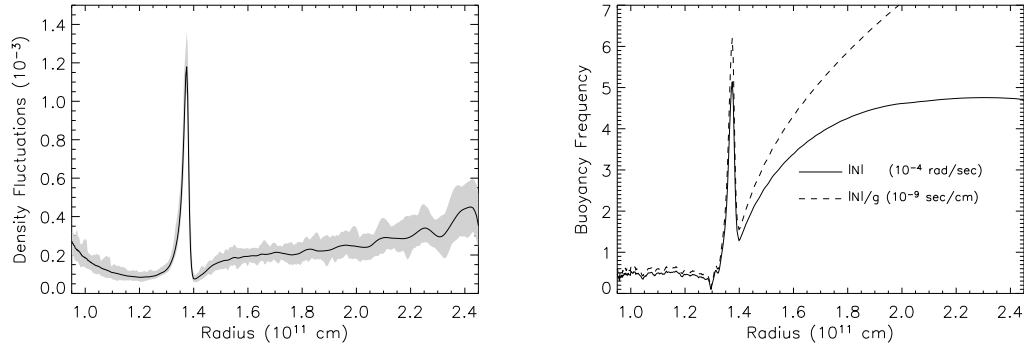


Figure 4.14: (left) Density fluctuations in the 3D core convection model: The time averaged maximum density fluctuation is shown as the thick line, with extreme values for the averaging period (two convective turnovers) shown by the shaded region. The largest fluctuations occur at the interface between the turbulent convective region and the stably stratified layer. The maximum fluctuation at the interface is  $\rho'/\langle\rho\rangle \sim 0.12\%$ . (right) The buoyancy frequency is shown in units of ( $10^{-4}$  rad/sec). Also shown by the dashed line is the buoyancy frequency normalized by the gravity which sets the scale of the density fluctuations at the convective boundary through equation 4.13. The expected density fluctuation is  $\rho'/\langle\rho\rangle \sim v_c|N|/g \sim 0.12\%$ , where a velocity scale of  $v_c \sim 2 \times 10^5$  cm/s has been used (see Figure 4.12).

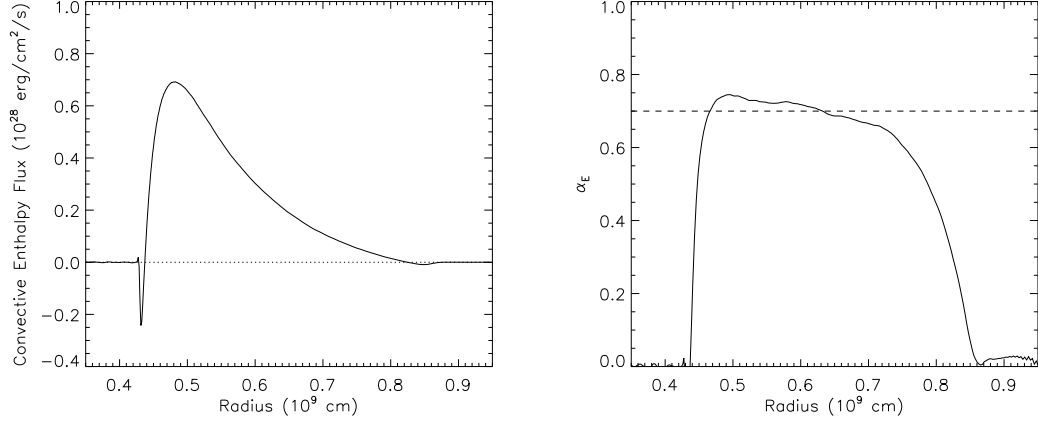


Figure 4.15: (left) Convective enthalpy flux,  $F_c = \overline{\langle \rho c_p v_r T' \rangle}$ . (right) Temperature-velocity correlation function  $\alpha_E$  calculated according to equation 4.21, with mean value  $\langle \alpha_E \rangle = 0.7$  shown by the dashed line.

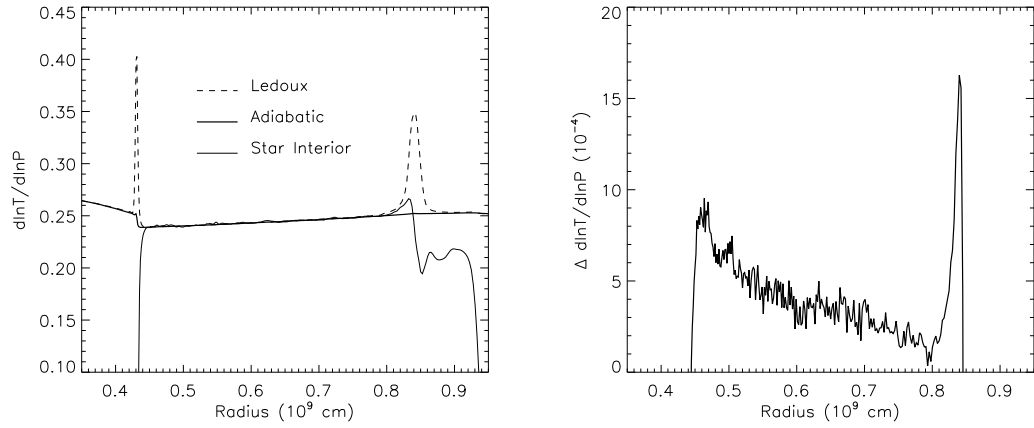


Figure 4.16: (left) Dimensionless temperature gradients: the stellar interior  $\nabla_s$ ; adiabatic  $\nabla_{ad}$ ; and Ledoux  $\nabla_{led}$  gradients are shown. (right) Super-adiabatic temperature gradient horizontally and time averaged.

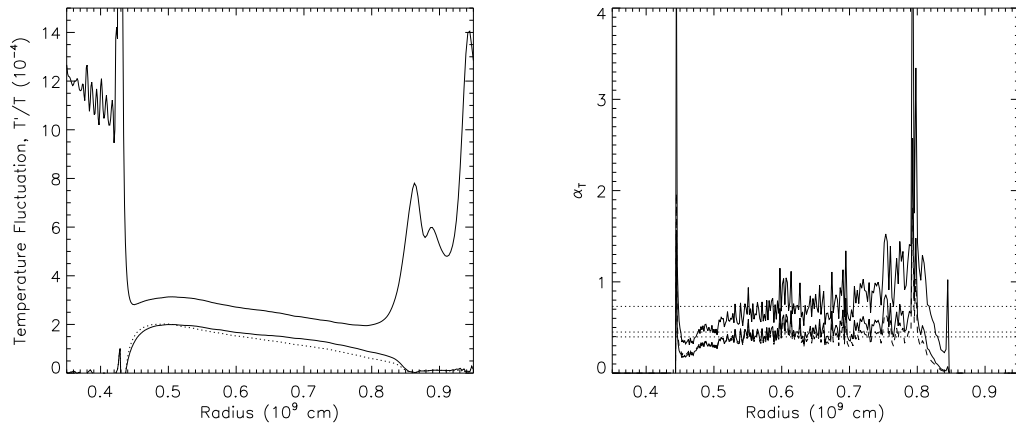


Figure 4.17: (left) Time averaged r.m.s. temperature fluctuations: (thick solid) line shows the r.m.s. fluctuations; the (thin solid) and (thin dotted) lines show the fluctuations in the upward and downward directed flow components, respectively. (right) The radial dependence of the "thermal mixing length" parameters  $\alpha_T$  defined by equation 4.22 are shown the temperature fluctuations presented in the left panel, using the same line types. The mean values, averaged over  $r \in [0.5, 0.75] \times 10^9 \text{ cm}$  are shown by the thin dotted lines.

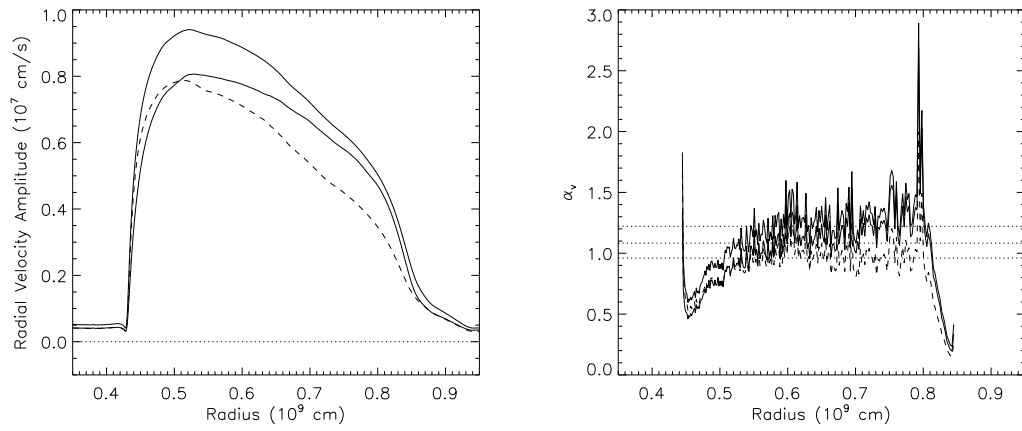


Figure 4.18: (left) Radial velocity amplitudes: (thick solid) r.m.s. value; the (thin solid) and (thin dashed) show the mean up- and down-flow velocities, respectively. (right) The radial dependance of the "velocity mixing length" parameters  $\alpha_v$  defined by equation 4.23 are shown for the velocity amplitudes presented in the left panel, using the same line types. The mean values, averaged over  $r \in [0.5, 0.75] \times 10^9$  cm are shown by the thin dotted lines.

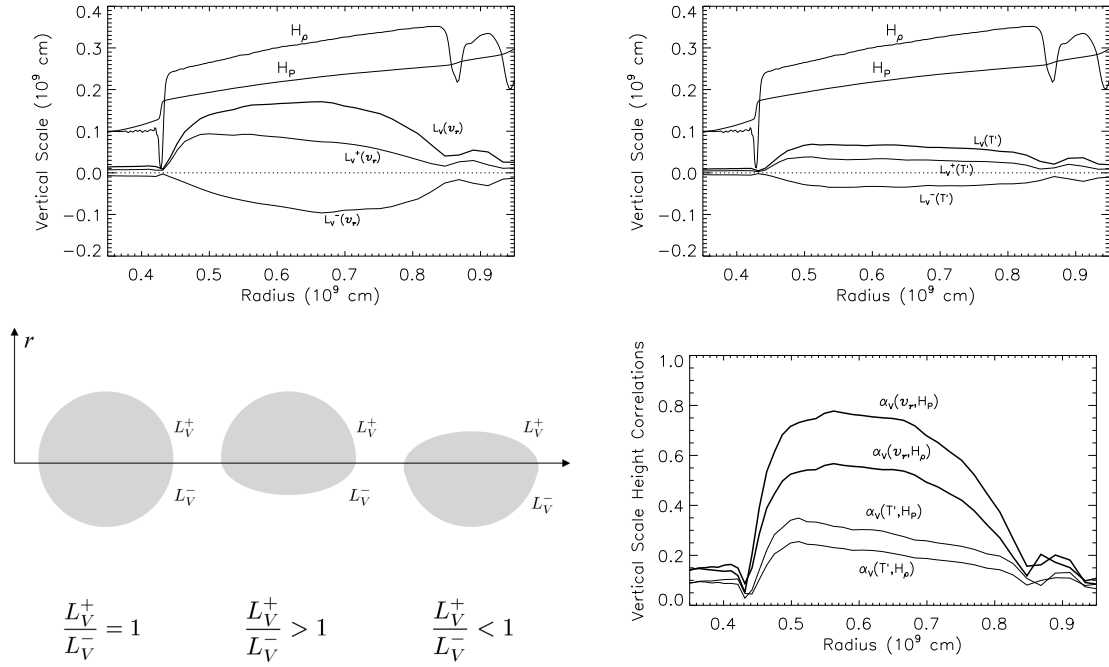


Figure 4.19: The vertical correlation length scales  $L_V$  as defined in §B. (top left)  $L_V$  for velocity fluctuations,  $v_r'$ ; (top right)  $L_V$  for temperature fluctuations,  $T'$ . The pressure scale height  $H_p$  and density scale height  $H_\rho$  are shown for comparison. (bottom left) Illustration of the relationship between eddy shape and the correlation length scales,  $L_V^+$  and  $L_V^-$ . The grey patches represent the shapes of the eddies and the  $L_V^{+/-}$  values are measured in the radial direction, away from the horizontal line. (bottom right) Correlations lengths  $L_V$  scaled to pressure and density scale heights, e.g.,  $\alpha_V(v_r, H_p) = L_V(v_r)/H_p$

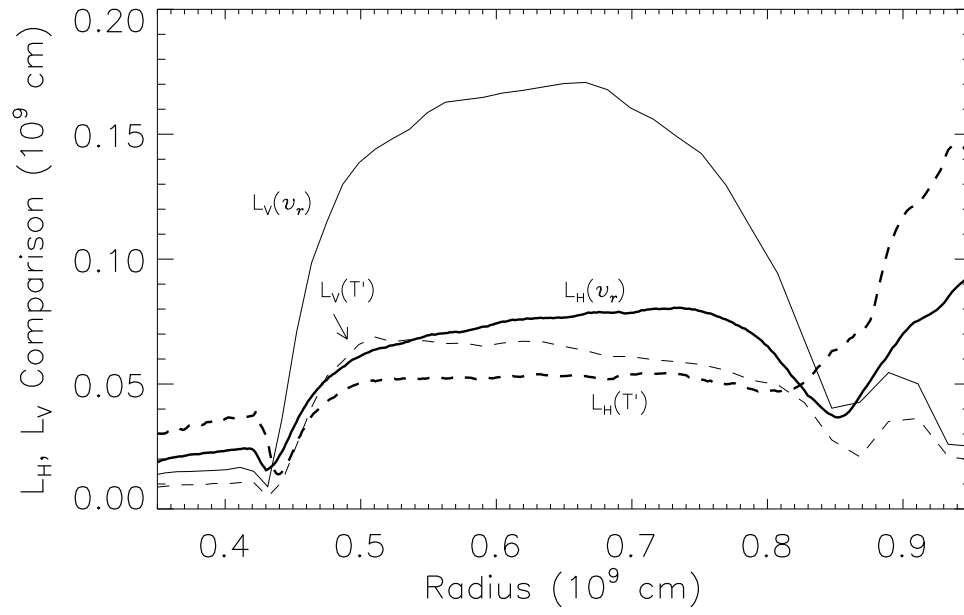


Figure 4.20: The horizontal and vertical correlation length scales,  $L_H$  (thick line) and  $L_V$  (thin line) are shown for temperature (dashed) and velocity (solid) fluctuations.

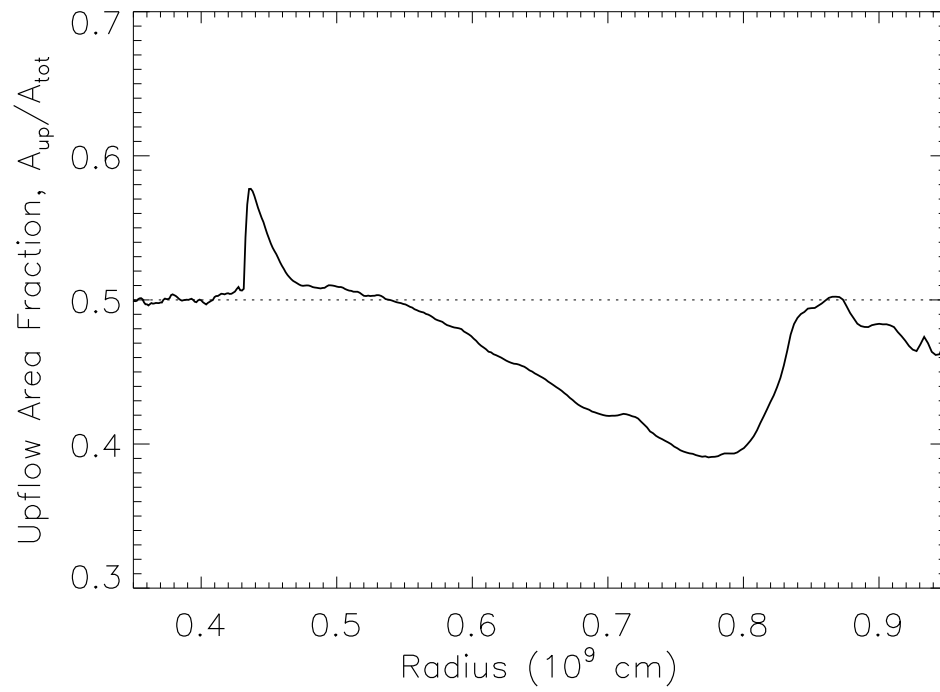


Figure 4.21: The fractional area occupied by the upward flowing material  $f_u$  is shown as a function of radial position. The downward flowing area is  $f_d = (1 - f_u)$  and the dashed line at  $1/2$  indicates up-down symmetry.

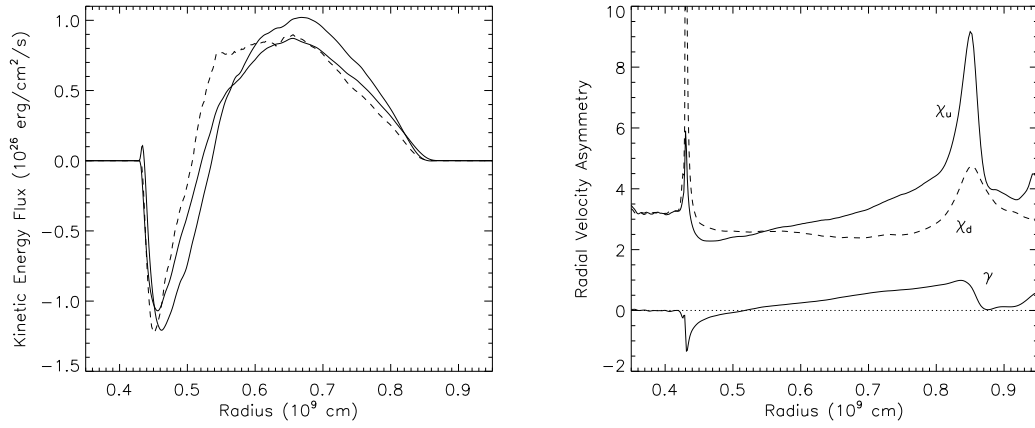


Figure 4.22: (left) Kinetic energy flux: (thick) line shows the value measured in the simulation averaged over two convective turnovers; the (thin solid) line shows  $F_K$  calculated according to equation 4.26; the (thin dashed) line shows  $F_K$  calculated according to equation 4.26 but uses  $c\langle v \rangle^3$  in place of  $\langle v^3 \rangle$ , and a correlation constant of  $c = 5$ . (right) Asymmetries in radial velocity: the (thick) line show the skewness in the velocity field,  $\gamma = \langle v^3 \rangle / \sigma_v^3$ ; the (thin solid) and (thin dashed) lines show the correlations  $\chi = \langle v^3 \rangle / \langle v \rangle^3$  where the subscripts  $u$  and  $d$  indicate up- and down-flows, respectively.



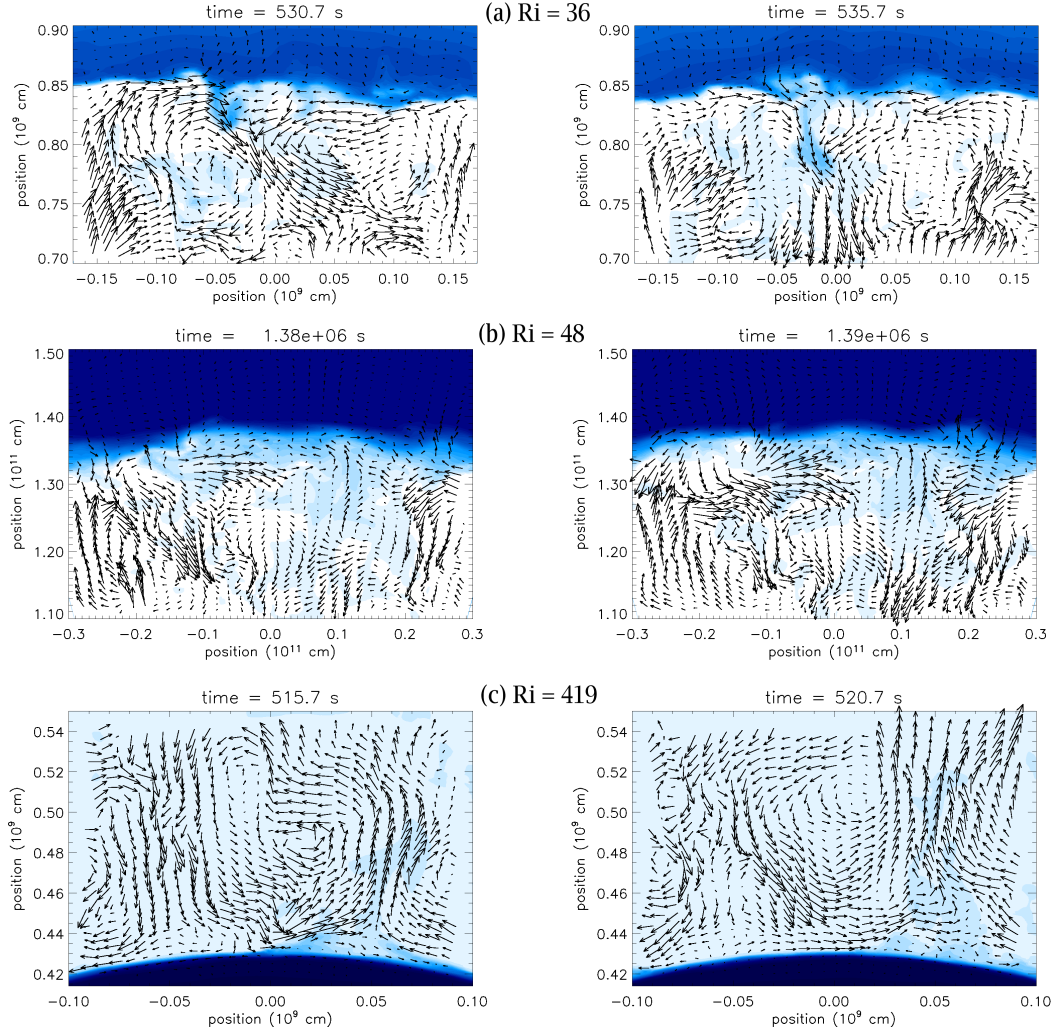


Figure 4.23: Equatorial slices showing the flow in the vicinity of the convective boundaries in the 3D simulations, ordered by relative stability: (row a) upper shell convection boundary,  $Ri_B \sim 36$ ; (row b) core convection boundary,  $Ri_B \sim 48$ ; (row c) lower shell convection boundary,  $Ri_B \sim 419$ . The colormap indicates composition abundance, where the darker tones trace stable layer material entrained across the interface. The velocity vectors have been sampled every third zone in each dimension.

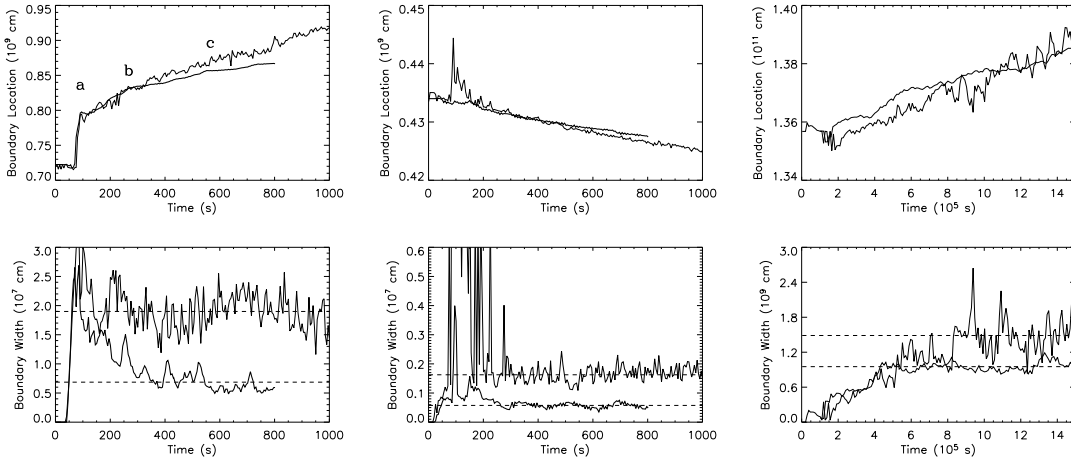


Figure 4.24: The time history of (top row) the convective boundary location, and (bottom row) the thickness of the convective interface for: (left) upper shell burning boundary; (middle) lower shell burning boundary; and (right) core convection boundary. The (thick line) identifies the 3D models, ob.3d.B and msc.3d.B; and the (thin line) identifies the 2D models, ob.2d.e and msc.2d.b. The (dashed lines) show the averaged interface thickness for  $t > 300$  s for oxygen burning, and  $t > 6.0 \times 10^5$  s for core convection. The letters (a-c) in the upper left panel mark times when the outward migration rate of the convective boundary rapidly adjusts to a new value in the 3D model.

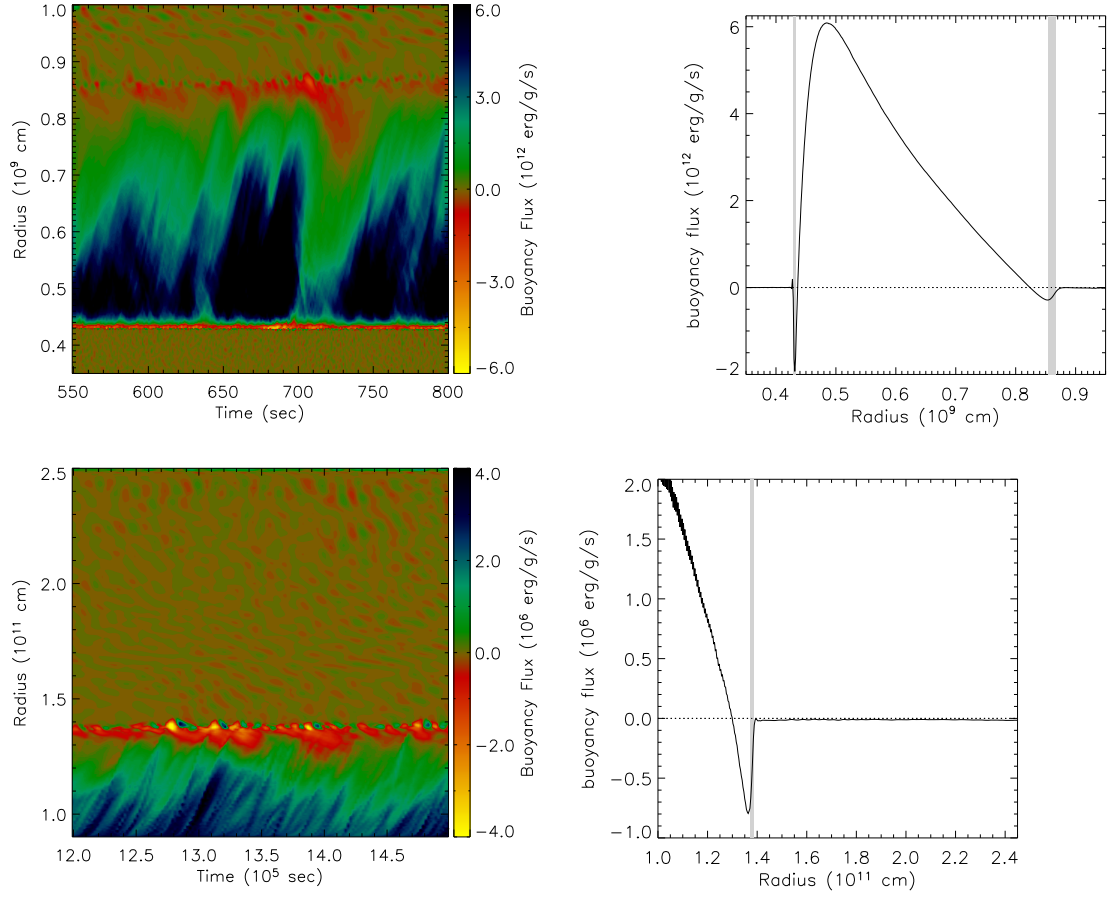


Figure 4.25: Buoyancy flux. Time-series diagrams and time-averaged radial profiles are shown for: (top-row) the 3D oxygen shell burning model; and (bottom-row) the 3D core convection model.

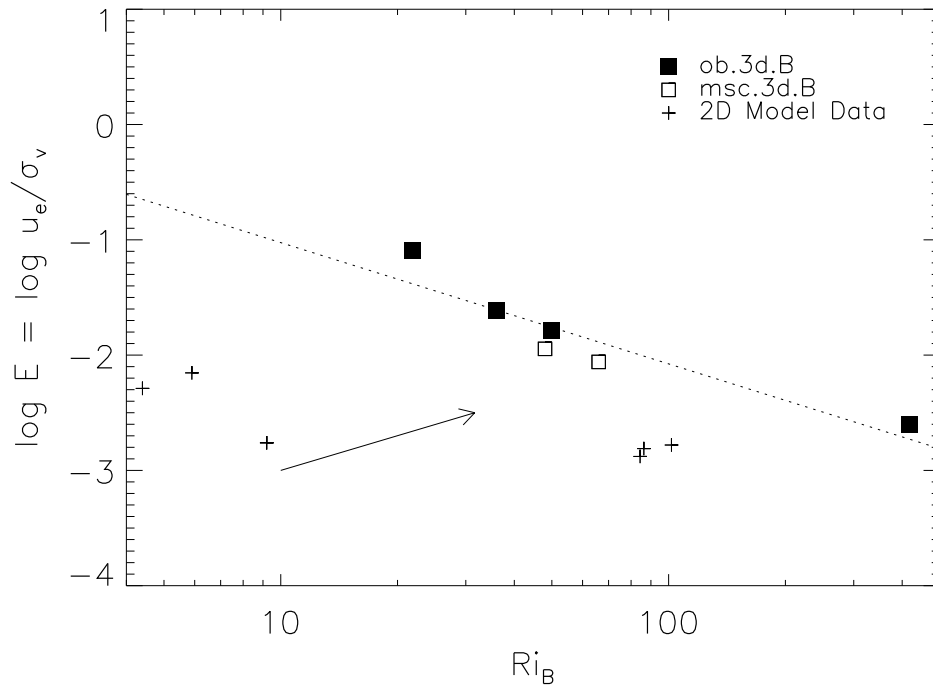


Figure 4.26: Normalized entrainment rate plotted against bulk Richardson number  $Ri_B$ . The 3D models are marked with squares, and the 2D data by plus signs. The best fit power-law to the 3D model data is shown by the dashed line. The 2D entrainment rates fall everywhere below the 3D trend. The arrow indicates the direction in the diagram that the 2D data points would move if the effective r.m.s. turbulence velocity were lower.

Table 4.1. Nuclei Included in Reduced Nuclear Reaction Network

Element	Charge	Atomic Weight
Helium . . . . .	2	4
Carbon . . . . .	6	12
Oxygen . . . . .	8	16
Neon . . . . .	10	20
Sodium . . . . .	11	23
Magnesium . . .	12	24
Silicon . . . . .	14	28
Phosphorus . . .	15	31
Sulfur . . . . .	16	32, 34
Chlorine . . . . .	17	35
Argon . . . . .	18	36, 38
Potassium . . . .	19	39
Calcium . . . . .	20	40, 42
Titanium . . . . .	22	44, 46
Chromium . . . .	24	48, 50
Iron . . . . .	26	52, 54
Nickel . . . . .	28	56

Note. — Network also includes electrons, protons, and neutrons.

Table 4.2. Summary of Oxygen Shell Burning Models

Parameter	Units	ob.3d.B	ob.2d.c	ob.2d.C	ob.2d.e
$r_{in}, r_{out}$	( $10^9$ cm)	0.3, 1.0	0.3, 1.0	0.3, 1.0	0.3, 5.0
$\Delta\theta, \Delta\phi$	(deg.)	30, 30	90, 0	90, 0	90, 0
Grid Zoning	-	$400 \times (100)^2$	$400 \times 320$	$800 \times 640$	$800 \times 320$
$t_{\max}$	(s)	800	574	450	2,400
$v_{\text{conv}}$	( $10^7$ cm/s)	0.8	2.0	1.8	1.8
$t_{\text{conv}}$	(s)	103	40	44	44
$\dot{M}_i _u$ <sup>1</sup>	( $10^{-4} M_\odot/\text{s}$ )	1.1	1.33		
$\dot{M}_i _l$	( $10^{-4} M_\odot/\text{s}$ )	-0.23	-0.52	-0.5	

<sup>1</sup>The subscripts  $u$  and  $l$  refer to the upper and lower convective shell boundary.

Table 4.3. Summary of “Core Convection” Models

Parameter	Units	msc.3d.B	msc.2d.b
$r_{in}, r_{out}$	( $10^{11}$ cm)	0.9, 2.5	0.9, 2.5
$\Delta\theta, \Delta\phi$	(deg.)	30, 30	30, 0
Grid Zoning	-	$400 \times (100)^2$	$400 \times 100$
$t_{\max}$	(s)	$2.0 \times 10^6$	$2.0 \times 10^6$
$v_{\text{conv}}$	( $10^5$ cm/s)	2.5	13
$t_{\text{conv}}$	(s)	$3.6 \times 10^5$	$6 \times 10^4$
$\dot{M}_i$	( $10^{-7} M_\odot/\text{s}$ )	2.72	4.73

Table 4.4. Assumed and Measured Convection Parameters<sup>a</sup>

Study	$\text{Pe}^b$	$\alpha_E$	$\alpha_{\Lambda,T}$	$\alpha_{\Lambda,v}$	$\alpha_\Lambda$	$L/H_p^c$	Grid Zoning
MLT	$\gg 1$	1	$\alpha$	$\alpha$	$\alpha$	...	...
This Study <sup>1</sup>	$\gtrsim 10^3$	$0.70 \pm 0.03$	0.8 - 1.4	1.35 - 1.73	0.87 - 1.31	$\sim 2(3.7)^d$	$100^2 \times 223(400)^c$
Chan-Sofia <sup>2</sup>	...	$0.81 \pm 0.03$	1.32 - 3.75	3.39 - 6.4	1.90 - 4.4	7	$20^2 \times (\lesssim 50)$
Kim <sup>3</sup>	...	$0.80 \pm 0.01$	2.96 - 4.2	1.5 - 3.4	1.4 - 3.2	6	$32^3$
Robinson <sup>4</sup>	...	0.65-0.85	...	...	...	8.5	$114^2 \times 170$
Porter-Woodward <sup>5a</sup>	$10 - 8 \times 10^4$	0.7-0.9	4.08	3.82	$2.68(3.53)^{5b}$	5	$512^2 \times 256$

<sup>a</sup>See §4.6.2 for parameter definitions:  $\alpha_{\Lambda,T} = 2 \times \alpha_T$  and  $\alpha_{\Lambda,v} = \sqrt{2} \times \alpha_v$  where  $\alpha_T$  and  $\alpha_v$  are defined by equations 4.22 and 4.23, and  $\alpha_\Lambda = \sqrt{\alpha_E \times \alpha_{\Lambda,v} \times \alpha_{\Lambda,T}}$ .

<sup>b</sup>The Péclet number is shown when provided by the author. In all cases the regions in the simulations for which parameter values are quoted were efficient convection, with  $\Delta\nabla \lesssim 10^{-2}$ , and excluded the super-adiabatic layers in the surface convection models where parameters deviate significantly from those quoted here.

<sup>c</sup>The number of pressure scale heights spanned by the convectively unstable region.

<sup>d</sup>The value in parentheses is for region spanning the entire computational domain, including the stable bounding layers with the other value referring to the convective region.

<sup>1</sup>Model ob.3d.B: additional details in Table 4.2.

<sup>2</sup>Chan & Sofia (1989): The range in  $\alpha_T$  and  $\alpha_{\Lambda,v}$  is calculated according to their Table 1 for the nearly adiabatic portion of the simulation where  $10^{-3} < \Delta\nabla < 10^{-2}$ .

<sup>3</sup>Kim et al. (1996): The coefficient  $\alpha_T$  is based on their Fig. 6. The coefficients  $\alpha_{\Lambda,v}$  and  $\alpha_\Lambda$  are plotted in their Fig. 9 and the range quoted in the table above is for values at least one pressure scale height from the boundaries.

<sup>4</sup>Robinson et al. (2004): only the correlation between radial velocity and temperature fluctuation is provided, which is a good surrogate for  $\alpha_E$ . For the solar and subgiant cases see their Figs. 7 - 9.

<sup>5</sup>(a)Porter & Woodward (2000): In this paper the values for  $\alpha_v$ ,  $\alpha_T$ , and  $\alpha_\Lambda$  are quoted using the same definitions as in this study. (b) The lower value quoted by these authors for  $\alpha_\Lambda$  is a results of subtracting the kinetic energy flux from the enthalpy flux. The value in the parentheses is the mixing length  $\alpha_\Lambda$  according to the definition in note <sup>a</sup>above.

Table 4.5. Convective Boundary Layer Properties For Oxygen Shell Burning

Models

Model	Time Interval ( $10^2$ s)	$\bar{r}_i$ ( $10^9$ cm)	$\bar{h}$ ( $10^7$ cm)	$\bar{r}_i$ ( $10^4$ cm/s)	$\overline{v_{exp}}$ ( $10^4$ cm/s)	$\sigma[v_H]^a$ ( $10^7$ cm/s)	$\Delta \bar{b}^b$ ( $10^7$ cm/s $^2$ )	$\log \bar{E}$	$\overline{Ri_B}$
ob.3d.B	[1.5, 2.7]	0.816	1.287	25.766 $\pm$ 0.869	0.6	0.313	0.574	-1.095	21.8
"	[2.7, 5.5]	0.842	0.797	8.252 $\pm$ 0.180	"	0.316	0.966	-1.616	36.0
"	[5.5, 8.0]	0.861	0.586	5.171 $\pm$ 0.179	"	0.281	1.062	-1.789	50.0
ob.2d.c	[3.5, 5.7]	0.857	0.191	10.620 $\pm$ 0.816	0.9	1.385	1.422	-2.154	5.9
ob.2d.C	[2.0, 4.0]	0.830	1.776	19.117 $\pm$ 0.988	0.5	1.436	1.010	-1.887	3.2
ob.2d.e	[3.5, 8.0]	0.868	1.900	10.021 $\pm$ 0.319	2.5	1.464	1.334	-2.289	4.4
ob.3d.B	[3.0, 8.0]	0.429	0.057	-0.700 $\pm$ 0.009	0.50	0.479	30.686	-2.601	418.6
ob.2d.c	[3.5, 5.7]	0.428	0.201	-1.686 $\pm$ 0.058	1.05	1.769	33.739	-2.811	86.3
ob.2d.C	[2.0, 4.0]	0.430	0.193	-1.625 $\pm$ 0.072	0.65	1.434	32.160	-2.780	101.7
ob.2d.e	[3.5, 8.0]	0.429	0.162	-0.975 $\pm$ 0.018	1.20	1.645	32.620	-2.879	84.4

<sup>a</sup>The rms fluctuations in the horizontal velocity at the interface location.

<sup>b</sup>The buoyancy jump across the interface.



Table 4.6. Convective Boundary Layer Properties For "Core Convection"  
Models

Model	Time Interval ( $10^5$ s)	$\bar{r}_i$ ( $10^{11}$ cm)	$\bar{h}$ ( $10^9$ cm)	$\bar{r}_i$ ( $10^3$ cm/s)	$\overline{v_{exp}}^a$ ( $10^2$ cm/s)	$\sigma[v_H]$ ( $10^5$ cm/s)	$\Delta\bar{b}$ ( $10^2$ cm/s <sup>2</sup> )	$\log \bar{E}$	$\overline{Ri_B}$
msc.3d.B	[6.0, 10.0]	1.374	0.949	$1.754 \pm 0.080$	...	2.011	6.07	-2.0594	66
"	[10.0, 12.0]	1.378	0.897	$-0.020 \pm 0.140$	...	1.878	5.83	...	72
"	[12.0, 15.0]	1.382	0.998	$2.731 \pm 0.099$	...	2.411	5.70	-1.9459	48
msc.2d.b	[6.0, 10.0]	1.369	1.319	$1.401 \pm 0.390$	...	8.070	6.43	-2.7604	9.2

<sup>a</sup>The expansion velocity in these models remains very small with  $v_{exp} < 10$  cm/s.

## CHAPTER 5

### CONCLUDING REMARKS

In this thesis a wide range of hydrodynamic behavior has been studied in the context of massive star interiors. The simulations presented are unique in terms of the epochs we have simulated, and the degree to which non-idealized physics have been used. Instead of simulating the flows for idealized problems, we have used initial conditions that are based on realistic stellar evolution models. A few of the most important results obtained during the course of this thesis research are listed here.

- The turbulent flow associated with thermal convection is found to be quantitatively and qualitatively different in 2D and 3D, with larger velocity amplitudes and larger scale flow structures in 2D. The turbulence-wave coupling is also found to be affected by the dimensionality, probably as a result of the differences in the convective flow morphology. In particular, the stable layer motions have a higher amplitude and lower temporal frequency in 2D, compared to 3D.
- Mixing length theory scaling provides a reasonable representation of the velocity scale and temperature gradient in a convective burning shell, though significant deviations are found near the convective boundaries. The mixing length which best fits our simulation data  $\sim 1.1H_p$  is not found to agree with the mixing lengths found for other 3D simulations in the literature. This strongly suggests that the mixing length is not a universal parameter, and depends on the background structure of the convection zone even for

deep efficient convection.

- We find for both our shell burning and core convection model that convective “overshooting” is not well described by the traditional “ballistic” model, wherein turbulent eddies are envisioned to penetrate into the stable layers. Instead, we find that boundary-turbulence interaction is better described as an elastic response by the boundary to impinging plumes. During this process, significant internal and interfacial wave motion is excited.
- The convective boundaries are found to be rife with internal and interfacial wave motions, and a variety of instabilities arise which induce mixing through a process best described as *turbulent entrainment*. The mixing that takes place at convective boundaries is found to depend on the bulk Richard number  $Ri_B$ , which characterizes the “stiffness” of the boundary. The mixing is found to proceed in a manner and at a rate which is similar to that found in analogous geophysical and laboratory studies of entrainment. In particular, the normalized entrainment rate  $E = u_E / \sigma_H$ , is well described by a power law dependance on the bulk Richardson number  $Ri_B = \Delta b L / \sigma_H^2$  with  $E = A Ri_B^{-n}$ . The best fit values for the parameters are  $\log A = 0.027 \pm 0.38$  and  $n = 1.05 \pm 0.21$ . Based on this physical picture, we propose the use of a *dynamic boundary condition* for one-dimensional stellar evolution codes based on  $Ri_B$  which will predict the extents of a convection zone better than purely local, static criteria like that of Ledoux or Schwarzschild.
- We find that the thermodynamic perturbations at convective boundaries can attain very large values (r.m.s. fluctuations as large as 10%), and are due to internal wave motions excited by the convective turbulence. These

perturbations may play a role in both the core-collapse explosion mechanism as well material mixing in the ejecta.

## 5.1 Related Efforts

The main motivation for the simulations carried out and studied in this thesis is improving stellar evolution models. Therefore, work is already underway to incorporate several of the main results from this thesis work into the TYCHO code, including the process of turbulent entrainment and the dynamic boundary condition described in chapter 4. In particular, it will be interesting to see what the integrated effects of these processes are on supernova progenitor models, as well as many other phases of evolution.

In addition to informing one-dimensional stellar evolution modeling, our models of the very last stages of evolution can be used as inputs to core collapse simulations. The current procedure is to use one-dimensional model profiles in core-collapse calculations. An interesting advancement would involve using a multi-D model, with a self-consistently calculated convective flow and perturbations as initial conditions. In order to do this, we need to push our modeling capabilities to the very last moments before core collapse, when silicon is burning in a convective shell around an iron core. Some progress has already been made in this direction in 2D (see Figure 5.1). Plans are being made to use these models in the core-collapse simulation efforts being led by Chris Fryer (Fryer et al., 2006) and Adam Burrows (Burrows et al., 2006).

Another unsolved problem of interest in the supernova community, on which our simulations have some bearing, is the degree to which mixing occurs in the ejected material of the supernova due to instabilities in the outgoing shock (see e.g. Arnett, Fryxell & Müller, 1989; Kifonidis et al., 2003, 2006). Some re-

cent work on Richtmyer-Meshkov and Rayleigh-Taylor instabilities suggest that multi-mode seed perturbations lead to instability growth that is significantly more efficient at mixing material than single mode growth (Miles, 2004). A novel approach taken to study this problem is the experimental effort being led by Paul Drake which uses high power lasers to create blast waves that are dynamically similar<sup>1</sup> to supernova blasts moving through stellar envelopes (Ryutov et al., 1999; Kuranz et al., 2005). An interesting advancement in this field is the inclusion of multi-mode surface perturbations at the density interfaces in the targets, which represent the composition interfaces in stellar interiors. In order to make closer contact with stellar hydrodynamic models, Paul Drake will be using a target with perturbations based on the convective boundary distortions measured in our convection simulations.

The hydrodynamics of stellar interiors studied in this thesis, although state of the art by today's standards, represent historically only a only crude beginning, and many advancements need to be made. Examples include: higher Reynolds number flow (i.e., higher resolution); larger computational domains in order to study low order modes in the flow, and rotation; the inclusion of magnetic fields; and a more diverse set of stellar interior conditions. Clearly a lifetimes worth of work remains to be done, which includes both considerable computing *and* thinking.

---

<sup>1</sup>Here, dynamical similarity is used in a technical sense, and means that the two problems being compared are described by the same dimensionless parameters, and therefore the evolution should proceed in the same way, only scaled in time and space.

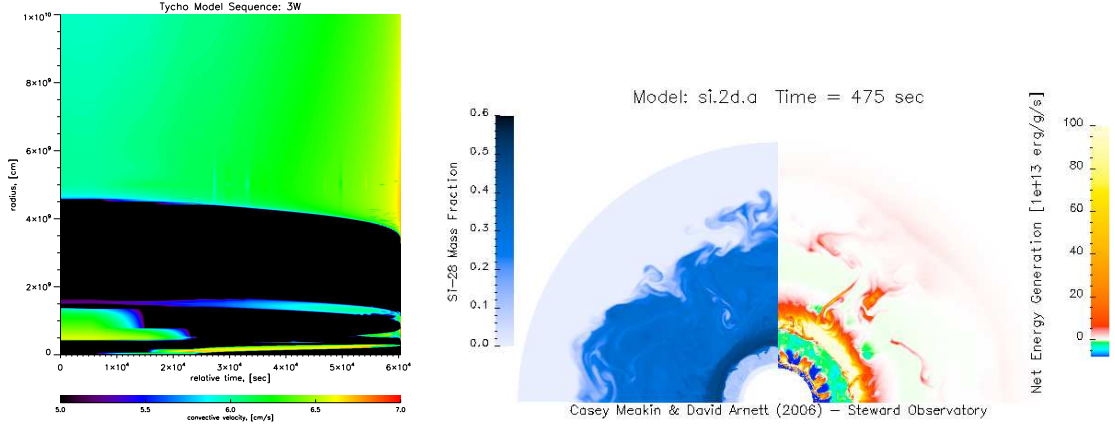


Figure 5.1: Presupernova silicon burning hydrodynamics: (left) The radial dependence of the convective velocity is shown as a function of time for a one-dimensional  $23 M_{\odot}$  stellar model as it approaches core collapse, which commences at the very end of the time-sequence shown. The innermost convection zone is due to silicon burning, and a transition from core to shell burning can be seen. The overlying convection zones are driven by oxygen, neon, and carbon burning shells. This model was evolved with the TYCHO stellar evolution code. (right) This snapshot shows the distribution of  $^{28}\text{Si}$  and net energy generation for a two dimensional hydrodynamic simulation of the TYCHO model  $\sim 1000$  s before core collapse. Silicon, oxygen, neon, and carbon are burning in concentric shells progressively further away from the iron-rich core which will soon undergo gravitational collapse. The outer boundary of the oxygen burning convection zone is strongly perturbed by the convective motions which eventually mixes the carbon, neon and oxygen burning shells together prior to core collapse.

## APPENDIX A

### TURBULENT ENERGY EQUATION

#### A.1 Total Energy

The primitive energy equation solved by PROMPI is,

$$\partial_t(\rho E) + \nabla \cdot [(\rho E + p)\mathbf{u} + \mathbf{F}_r] = \rho \mathbf{u} \cdot \mathbf{g} + \rho \epsilon_{net} \quad (\text{A.1})$$

where the total energy is composed of the internal and kinetic components,  $E = E_I + E_K$ . We decompose the velocity, density, and pressure fields into mean and fluctuating components according to,

$$\varphi = \varphi_0 + \varphi' \quad (\text{A.2})$$

where  $\langle \varphi \rangle = \varphi_0$  and  $\langle \varphi' \rangle = 0$ . The pressure-velocity correlation term is,

$$\nabla \cdot \overline{p\mathbf{u}} = \nabla \cdot \overline{p_0\mathbf{u}_0} + \nabla \cdot \overline{p_0\mathbf{u}'} + \nabla \cdot \overline{p'\mathbf{u}_0} + \nabla \cdot \overline{p'\mathbf{u}'}. \quad (\text{A.3})$$

The gravity term is,

$$\overline{\rho \mathbf{g} \cdot \mathbf{u}} = \overline{\rho_0 \mathbf{u}_0 \mathbf{g}} + \overline{\rho_0 \mathbf{u}' \mathbf{g}} + \overline{\rho' \mathbf{u}_0 \mathbf{g}} + \overline{\rho' \mathbf{u}' \mathbf{g}}. \quad (\text{A.4})$$

The averaging operator eliminates terms which are first order in fluctuations (by definition) and we have,

$$\partial_t \overline{\rho E} + \nabla \cdot \left[ \overline{\rho E \mathbf{u}_0} + \overline{\rho E \mathbf{u}'} + \overline{p_0 \mathbf{u}_0} + \overline{p' \mathbf{u}'} + \mathbf{F}_r \right] = \overline{\rho_0 \mathbf{u}_0 \mathbf{g}} + \overline{\rho' \mathbf{u}' \mathbf{g}} + \overline{\rho \epsilon_{net}}. \quad (\text{A.5})$$

We can further simplify this expression using the condition of hydrostatic equilibrium, which holds to a high degree of accuracy in the simulation ( $\nabla p_0 = \rho_0 \mathbf{g}$ ). The background velocity in this case,  $\mathbf{u}_0$ , is a slow, highly subsonic, expansion or contraction that is driven on a thermal timescale. The background velocity field has only a radial component (i.e., there is no rotation in the current model),  $\mathbf{u}_0 = (u_{0,(r)}, 0, 0)$ . The energy equation can be then simplified to read,

$$\partial_t \overline{\langle \rho E \rangle} + \nabla \cdot \overline{\langle \rho E \mathbf{u}_0 \rangle} = -\nabla \cdot \overline{\langle \mathbf{F}_p + \mathbf{F}_I + \mathbf{F}_K + \mathbf{F}_r \rangle} - \overline{\langle p_0 \nabla \cdot \mathbf{u}_0 \rangle} + \overline{\langle \mathbf{W}_b \rangle} + \overline{\langle \rho \epsilon_{net} \rangle}. \quad (\text{A.6})$$

where we have used the following definitions,

$$\mathbf{F}_I = \rho E_I \mathbf{u}' \quad (\text{A.7})$$

$$\mathbf{F}_K = \rho E_K \mathbf{u}' \quad (\text{A.8})$$

$$\mathbf{F}_p = p' \mathbf{u}' \quad (\text{A.9})$$

$$\mathbf{W}_b = \rho' \mathbf{g} \cdot \mathbf{u}'. \quad (\text{A.10})$$

## A.2 Kinetic Energy

The kinetic energy equation is derived by forming the scalar product of the velocity with the equation of motion (e.g., Shu, 1992, Ch.2). The kinetic energy equation can be written in vector form as,

$$\partial_t (\rho E_K) + \nabla \cdot (\rho E_K \mathbf{u}) = -\mathbf{u} \cdot \nabla p + \rho \mathbf{u} \cdot \mathbf{g} \quad (\text{A.11})$$

Again, we decompose the fields into mean and fluctuating components, employ the hydrostatic equilibrium condition, and perform averages. The result is,

$$\partial_t \overline{\langle \rho E_K \rangle} + \nabla \cdot \overline{\langle \rho E_K \mathbf{u}_0 \rangle} = -\nabla \cdot \overline{\langle \mathbf{F}_p + \mathbf{F}_K \rangle} + \overline{\langle p' \nabla \cdot \mathbf{u}' \rangle} + \overline{\langle \mathbf{W}_b \rangle} - \epsilon_K. \quad (\text{A.12})$$



Here,  $\varepsilon_K$  is the viscous dissipation of kinetic energy. In our simulations, this term is not modeled explicitly and arises due to numerical dissipation. The term  $p'\nabla \cdot \mathbf{u}'$  represents the compressional work done by turbulent fluctuations, and the other terms are as defined above.

## APPENDIX B

### CORRELATION LENGTH SCALES

In this section, several correlation lengths in the horizontal and vertical direction, denoted by  $\mathcal{L}_H$ ,  $L_H$ ,  $L_V$ ,  $L_V^+$ , and  $L_V^-$  are defined.

The vertical correlation of the horizontal distribution of fluctuations in a quantity  $X' = X - \langle X \rangle$  at radial position  $r$  and offset position  $r + \delta r$  is calculated according to,

$$C^V(\delta r; r) = \frac{1}{\Delta\Omega} \frac{\int X'(r, \theta, \phi) X'(r + \delta r, \theta, \phi) d\Omega}{\sigma_X(r) \sigma_X(r + \delta r)} \quad (\text{B.1})$$

where the integral is taken over the angular direction with  $d\Omega = \sin(\theta) d\theta d\phi$  and  $\Delta\Omega = \int d\Omega$ . The correlation is normalized by the product of the horizontal r.m.s. value of the quantity at the two levels being compared  $\sigma_X$ .

The horizontal correlation of fluctuations at radial position  $r$  is calculated using the autocorrelation function,

$$C^H(\delta s; r) = \frac{\langle X'(r, s) X'(r, s + \delta s) \rangle}{\sigma_X(r)^2} \quad (\text{B.2})$$

where the brackets  $\langle \cdot \rangle$  denote averaging over all horizontal locations  $s$  and fixed offset  $\delta s$ . The horizontal correlation is normalized by the variance of the quantity  $\sigma_X^2$ .

Two characteristic length scales are defined in the horizontal direction,  $\mathcal{L}_H$ , and  $L_H = 2 \times \mathcal{L}_H$ . The length scale  $\mathcal{L}_H$  is defined as the offset position where the horizontal correlation function drops to a value of 0.5. ( $\mathcal{L}_H$  provides a good approximation to the horizontal integral scale,  $\int C^H(\delta s; r) d\delta s$ .) Twice this length

is denoted by  $L_H$ , which is the full width at half maximum of the horizontal correlation function.

In the vertical direction, three length scales are defined,  $L_V^-$ ,  $L_V^+$ , and  $L_V = L_V^+ - L_V^-$ . The sign of the radial offset  $\delta r$  in the correlation function is retained, and separate length scales are defined for positive and negative offsets for which the correlation function drops to 0.5. These are denoted  $L_V^+$  and  $L_V^-$ . The full width is denoted  $L_V$  and is defined by  $L_V = L_V^+ - L_V^-$ .

## APPENDIX C

### NON-RADIAL WAVE EQUATION

In addition to the turbulence sustained in a stellar interior by e.g., thermal convection and shear instabilities, the stellar plasma can also host internal wave motions. The linear wave equation is a useful tool for analyzing stable layer motion, even when amplitudes are approaching non-linear values or the waves are propagating through turbulent regions. This is so because wave interactions occur at second or higher order in the wave equation (see e.g. Phillips, 1966, sec. 3.8), and the interactions among the lowest order internal wave modes occurs at third order (Phillips, 1966, sec. 5.4). Therefore, the general properties of waves derived from a linear wave equation are found to be quite robust, even in the presence of turbulence.

An elementary introduction to linear internal waves is presented by Turner (1980, ch.2). A more exhaustive treatment in the stellar interiors context is provided by Unno et al. (1989) and Ledoux & Walraven (1958). In this appendix, I present a brief introduction to the linear-, adiabatic-, non-radial wave equation appropriate to the geometry of the computational domains used in our hydrodynamic simulations, and I described the method used to calculate the eigenmodes which are compared to the stable layer motions observed in our simulations.

#### C.1 Non-Radial Wave Equation

The starting point for deriving the linear wave equation are the fully nonlinear Euler equations (eq. [4.5]). The developed hydrodynamic flow in our calculations

consists of turbulent convection as well as propagating internal waves. Here, we are interested in the nature of the wave modes so we decompose the velocity field into two parts  $\mathbf{u} \rightarrow \mathbf{u}_c + \mathbf{u}_o$  which represent the turbulent convection and the oscillatory modes, respectively. We write the oscillatory component of the velocity  $\mathbf{u}_o$  as  $\mathbf{v}$  and consider only the wave contribution from here on. (The interaction of turbulence and waves is a subject outside the scope of this appendix. Some aspects of this process are touched on in chapter 3, and a variety of diverse approaches to the problem can be found in the literature (Lighthill, 1952; Townsend, 1966; Press, 1981; Goldreich & Kumar, 1990)).

The internal waves are considered to produce small thermodynamic fluctuations relative to the background equilibrium state, which we take to be the non-rotating, non-magnetic star model calculated with the TYCHO code, or the horizontally averaged background profile of the hydrodynamic simulation. The small overall contraction or expansion of the star is ignored in our analysis since this occurs on a timescale much larger than the wave periods, and also occurs on a time scale that is much larger than the hydrostatic equilibration timescale (the exception is the few minutes leading up to core-collapse, where the contraction velocity reaches the sound speed).

The equations of motion for the oscillations are found by considering perturbations superimposed on the background which are small enough ( $f'/f_0 \ll 1$ ) that second and higher order terms describing them can be neglected without introducing significant errors. The perturbations can be expressed in either Eulerian or Lagrangian form which are denoted in the following way,

$$f(\mathbf{r}, t) = f_0(\mathbf{r}) + f'(\mathbf{r}, t), \quad (\text{C.1})$$

and

$$f(\mathbf{r}, t) = f_0(\mathbf{r}) + \delta f(\mathbf{r}, t), \quad (\text{C.2})$$

respectively. The Lagrangian and Eulerian perturbations are related to each other to first order through the Lagrangian displacement vector,  $\xi$ , by,

$$\delta f = f' + \xi \cdot \nabla f_0, \quad (\text{C.3})$$

with,

$$\xi \equiv \mathbf{r} - \mathbf{r}_0, \quad (\text{C.4})$$

where  $\mathbf{r}$  represents the new location of a parcel of material originally located at position  $\mathbf{r}_0$  in the equilibrium state. Using these relations, the equations of motion (eq. [4.5]) are reduced to a set of linear, homogeneous, partial differential equations with respect to time  $t$  and space coordinates  $\mathbf{r}$  for the perturbed quantities. The coefficients of the linear perturbation equations are functions solely of the equilibrium state, and hence the radial coordinate alone, which allows us to separate the time variable and take the perturbations as proportional to  $e^{i\sigma t}$ . In addition to the time and space separation, we can further separate the spatial dependence into radial and angular parts because the coefficients of these differential equations depend only on the radius,  $r$ . The adiabatic oscillation equations are reduced to the following set of ODEs,

$$\frac{1}{\rho} \left( \frac{\partial}{\partial r} + \frac{\rho g}{\Gamma_1 p} \right) p' - (\sigma^2 - \nu_B^2) \xi_r = 0 \quad (\text{C.5})$$

$$\frac{1}{r^2} \frac{\partial}{\partial r} (r^2 \xi) + \frac{1}{\Gamma_1} \frac{d \ln p}{dr} \xi_r + \left( \frac{\rho}{\Gamma_1 p} + \frac{\nabla_{\perp}^2}{\sigma^2} \right) \frac{p'}{\rho} = 0, \quad (\text{C.6})$$

where,

$$\nabla_{\perp}^2 = \frac{1}{r^2} \frac{1}{\sin^2 \theta} \left[ \sin \theta \frac{\partial}{\partial \theta} \left( \sin \theta \frac{\partial}{\partial \theta} + \frac{\partial^2}{\partial \phi^2} \right) \right]. \quad (\text{C.7})$$

Additional equations and terms describing the perturbation to the gravitational potential  $\Phi'$  have been dropped and  $\Phi' \approx 0$  is assumed. This is a good approximation for the high degree g-modes that we are interested in here because the angular perturbations in the density will add incoherently, and result in a very small  $\Phi'$ . (The  $\Phi'$  needs to be retained for very low order, and purely radial modes.)

The angular dependence, denoted  $\mathcal{Y}(\theta, \varphi)$ , must satisfy,

$$[r^2 \nabla_{\perp}^2 + \lambda^2] \mathcal{Y}(\theta, \varphi) = 0. \quad (\text{C.8})$$

When full spherical domains are considered the spherical harmonics satisfy this equation and provide a complete set of orthogonal functions, and we have  $\mathcal{Y}(\theta, \varphi) = Y_l^m(\theta, \varphi)$  and  $\lambda^2 = l(l+1)$ . If we use the thermodynamic relation,  $c^2 = \Gamma_1 p / \rho$ , and define the Lamb frequency,

$$L_l^2 = \frac{l(l+1)}{r^2} c^2, \quad (\text{C.9})$$

we now rewrite the oscillation equations (C.5) - (C.6) as the following two coupled first order ODEs for the unknown functions  $\xi_r(r)$  and  $p'(r)$  (which are functions of radius only),

$$\frac{1}{r^2} \frac{d}{dr} (r^2 \xi_r) - \frac{g}{c^2} \xi_r + \left( 1 - \frac{L_l^2}{\sigma^2} \right) \frac{p'}{\rho c^2} = 0, \quad (\text{C.10})$$

$$\frac{1}{\rho} \frac{dp'}{dr} + \frac{g}{\rho c^2} p' + (\nu_B^2 - \sigma^2) \xi_r = 0. \quad (\text{C.11})$$

### C.1.1 Dependence on Computational Domain

Our 3D computational domains are not full spheres but are wedges. Therefore, we must find a complete set of basis functions which satisfy equation (C.8) and are orthogonal over the angular extents of our computational wedge. We are able to find such a set by simplifying the angular operator  $\nabla_{\perp}^2$ . Our 3D simulation wedges cover only a small angle in co-latitude and are centered on the equatorial plane, so  $\sin(\pi/2 + \epsilon) = \cos(\epsilon) \approx 1$ . For the largest wedge which we have simulated  $\epsilon_{max} = 15^\circ$  and  $\cos \epsilon_{max} = 1.01$ , which introduces an error on the percent level. Making this approximation, the angular operator  $\nabla_{\perp}^2$  reduces to,

$$\widetilde{\nabla}_{\perp}^2 = \frac{1}{r^2} \left( \frac{\partial^2}{\partial \theta^2} + \frac{\partial^2}{\partial \varphi^2} \right), \quad (\text{C.12})$$

and the following function satisfies our needs,

$$\mathcal{Y}_{l,m}(\theta, \varphi) = c_{lm} e^{i(\kappa_l \theta + \kappa_m \varphi)}, \quad (\text{C.13})$$

with,

$$\kappa_l = \frac{2\pi}{\delta\theta} l, \text{ and } \kappa_m = \frac{2\pi}{\delta\varphi} m, \quad (\text{C.14})$$

where  $l$  and  $m$  are integers between  $-\infty, \infty$  and  $\delta\theta$  and  $\delta\varphi$  are the extents of the azimuthal and co-latitude angle in the computational wedge.

Using the basis function in equation (C.13) instead of the spherical harmonics for the angular profile of the modes changes the oscillation equations (C.10) - (C.11) only through a new definition of the Lamb frequency,

$$L_l^2 \rightarrow L_{lm}^2 = \frac{\kappa_l^2 + \kappa_m^2}{r^2} c^2. \quad (\text{C.15})$$



## C.2 Eigenmode Solutions

The oscillation equations (C.10) - (C.11) and boundary conditions pose an eigenmode problem. A nice discussion of the general properties of the eigenmodes (which consist of an eigenvalue  $\sigma$  and eigenfunction  $\{\xi(r), p'(r)\}$ ) is presented in Kippenhahn & Weigert (1990, ch. 40).

For finding eigenmode solutions, I use the same boundary conditions which are imposed on the numerical simulation, i.e., I enforce the radial component of the velocity to go to zero at the boundaries. These two boundary conditions (one at either end of the domain) fully describe the problem. The eigenvalue and the eigenfunction are calculated using the shooting method in an iterative procedure, starting the integration from the inner boundary. If the outer boundary condition is not satisfied, the eigenvalue (i.e., the modal frequency  $\sigma$ ) is adjusted and the integration is performed again. This procedure is iterated until a desired accuracy in the eigenvalue is achieved.

## APPENDIX D

### COMPUTATIONAL COSTS

The computational requirements and available computing resources play a central role in planning multi-dimensional astrophysical simulation, especially those in 3D. In this appendix I describe the main computational resources used for the calculations presented in this thesis for posterity (and perhaps to humor our future readers, who will surely note that our efforts have been eclipsed by the relentless progress known as Moore's law<sup>1</sup>).

The calculations presented in this thesis were undertaken on three computing clusters that were available on campus. The astronomy department's *GRENDDEL* cluster is outfitted with 50 nodes, each with 2 AMD Operton Processors @ 2GHz clock speeds and 4GB system ram. Of these 50 nodes we ran most of our calculations on as many as 32 processors. On the *MENDELEYEV* Beowulf cluster, a second cluster maintained by the Astronomy department, we have full time access to 32 AMD Athlon Processors @ 1.5 GHz clock speeds and 1GB ram/processor. In addition to these two Astronomy department clusters we used the AURA cluster, maintained by the University of Arizona's High Performance Computing (HPC) division. *AURA* is an HP/Compaq Alpha GS1280 system with 256 EV7 processors @ 1.15 GHz clock speeds and 320GB of system memory. We have access to a 64 processor queue on *AURA*, on which we were able to secure about 50% of the wall clock time.

The total wall clock time used for the largest three-dimensional simulation

---

<sup>1</sup>Some of the implications of Moore's law for large scale computations have been worked out in Gottbrath et al. (1999)

model that we have undertaken ( $N_{tot} = N_{time} \times N_{space} \sim 10^6 \times (4 \times 10^6) \sim 4 \times 10^{12}$  space-time zones) is equivalent to 219 days on 32 processors using the *GREND*EL cluster (19.2 processor years). This calculation was spread out over the course of about 2 years. The *MENDELEYEV* and *AURA* clusters are approximately 75% as efficient as *GREND*EL, although the slower network speed on the *MENDELEYEV* cluster decreases its efficiency when using more than  $\sim 20$  processors. Moderate resolution ( $N_{zones} = 400^2$ ) two-dimensional models of advanced burning stages can be calculated for a good fraction of the nuclear evolutionary time in a week using only 16 processors.

I have developed software to manage restarting, re-gridding, and tiling of smaller domains into larger domains, allowing us to more efficiently relax models and restart them for more expensive, higher resolution simulation after any initial transients. Having access to multiple parallel computers, in addition to a variety of single processor workstations, has allowed us to explore a variety of models simultaneously.

In addition to the cluster-computing resources, three additional workstations were used for data storage and analysis, each with dual 2GHz clock speed processors and a total of 3+ TB of storage space. We also employ a DVD writer for archiving simulation restart files, reduced simulation data, and snapshots of the most recent version of our codes. Data processing and analysis were undertaken using a combination of the open source visualization program *OpenDX* (see [opendx.org](http://opendx.org) for more information) and the proprietary package *IDL* (developed by RSI), in addition to a variety of Fortran and C-language post-processing and analysis software. The total raw data output from the simulations calculated during the course of this thesis work is of order 2+ TB.

## REFERENCES

- Abia, C., Domínguez, I., Gallino, R., Busso, M., Masera, S., Straniero, O., de Laverny, P., Plez, B., Isern, J. *ApJ*, 579, 817
- Alexakis, A., et al. 2004, *ApJ*, 602, 931
- Alexakis, A. 2004, Ph.D. Thesis, U.Chicago
- Alexander, D. R., & Ferguson, J. W. 1994, *ApJ*, 437, 879
- Almgren, A. S., Bell, J. B., Rendleman, C. A., & Zingale, M. 2006, *ApJ*, 637, 922
- Arnett, D., 1972, *ApJ*, 173, 393
- Arnett, D., 1994, *ApJ*, 427, 932
- Arnett, D. 1996, *Supernovae and Nucleosynthesis: An Investigation of the History of Matter, from the Big Bang to the Present*, by D. Arnett. Princeton: Princeton University Press, 1996
- Arnett, D., Bahcall, J. Kirshner, R. Woosley, S. *ARA&A*, 27, 629
- Arnett, D., Fryxell, B., & Müller 1989, *ApJL*, 341, 63
- Arnett, W. D., & Thielemann, F.-K. 1985, *ApJ*, 295, 589
- Asida, S. M., & Arnett, D. 2000, *ApJ*, 545, 435
- Asplund, M., Grevesse, N., & Sauval, A. J. 2005, in *ASP Conf. Ser. 336, Cosmic Abundances as Records of Stellar Evolution and Nucleosynthesis*, ed. T. G. Barnes III & F. N. Bash (San Francisco: ASP), in press (astro-ph/0410214)
- Aufderheide, M. B. 1993, *ApJ*, 411, 813

- Bahcall, J. N., Serenelli, A. M., & Basu, S. 2006, *ApJS*, 165, 400
- Baltrusaitis, R. M., Gittings, M. L., Weaver, R. P., Benjamin, R. F., & Budzinski, J. M. 1996, *Physics of Fluids*, 8, 2471
- Basu, S. 1997, *MNRAS*, 288, 572
- Bazan, G., & Arnett, D. 1998, *ApJ*, 496, 316
- Beaudet, G., Petrosian, V., & Salpeter, E. E. 1967, *ApJ*, 150, 979
- Belkacem, K., Samadi, R., Goupil, M. -, & Kupka, F. 2006, *ArXiv Astrophysics e-prints*, arXiv:astro-ph/0607568
- Biello, J. 2001, PhD Thesis, U.Chicago
- Blöcker, T., Holweger, H., Freytag, B., Herwig, F., Ludwig, H.-G., Steffen, M. 1998, *Solar Composition and Its Evolution – From Core to Corona*, Proceedings of an ISSI Workshop, Bern, Switzerland, Kluwer Academic Publishers, Dordrecht/Boston/London, p. 105
- Böhm-Vitense, E. 1992, *Introduction to Stellar Astrophysics*, by Erika Böhm-Vitense, pp. 301. ISBN 05 21348714. Cambridge, UK: Cambridge University Press, January 1992.
- Böhm-Vitense, E., 1958, *ZAp*, 46, 108
- Bretherton, C. et al. 1999, *Quart. J. Roy. Meteor. Soc.*, 125, 391
- Browning, M., Brun, A., & Juri, T. 2004, *ApJ*, 601, 512
- Brummell, N. H., Clune, T. L., & Toomre, J. 2002, *ApJ*, 570, 825
- Burrows, A., Livne, E., Dessart, L., Ott, C. D., & Murphy, J. 2006, *ApJ*, 640, 878

- Buzasi, D. 2000, in Proc. Third MONS Workshop, ed. T. C. Teixeira & T. R. Bedding (Aarhus: Aarhus Univ.)
- Cabezón, R. M., García-Senz, D., & Bravo, E. 2004, *ApJS*, 151, 345
- Canuto, V. M., & Dubovikov, M. 1998, *ApJ*, 493, 834
- Carruthers, D. J., & Hunt, J. C. R. 1986, *Journal of Fluid Mechanics*, 165, 475
- Cattaneo, F., Brummell, N. H., Toomre, J., Malagoli, A., & Hurlburt, N. E. 1991, *ApJ*, 370, 282
- Cescutti, G., Francois, P., Matteucci, F., Cayrel, R., & Spite, M. 2006, *A&A*, 448, 557
- Chan, K. L., & Sofia, S. 1987, *Science*, 235, 465
- Chan, K. L., & Sofia, S. 1989, *ApJ*, 336, 1022
- Chan, K. L., & Sofia, S. 1996, *ApJ*, 466, 372
- Charbonnel, C., & Talon, S. 1999, *A&A*, 351, 635
- Clayton, D. D. 1983, *Principles of Stellar Evolution and Nucleosynthesis*, University of Chicago Press, Chicago
- Colella, P., & Glaz, H. M. 1985, *Journal of Computational Physics*, 59, 264
- Colella, P., & Woodward, P., 1984, *J. Chem. Phys.*, 54, 174
- Cox, J. P., & Guili, R. T., 1968, *Principles of Stellar Structure*, New York: Gordon & Breach
- Dearborn, D. S. P., Lattanzio, J. C., & Eggleton, P. P. 2006, *ApJ*, 639, 405

- Dearborn, D. S. P., Eggleton, P. . P. ., & Lattanzio, J. 2006, IAU Symposium, 239
- Deardorff, J. W. 1979, Journal of Atmospheric Sciences, 36, 424
- Deardorff, J. W. 1980, Journal of Atmospheric Sciences, 37, 131
- Demarque, P., Woo, J.-H., Kim, Y.-C., Yi, S. 2004, ApJ, 155, 667
- Denissenkov, P. A., & Tout, C. A. 2003, MNRAS, 340, 722
- Dessart, L., Burrows, A., Livne, E., & Ott, C. D. 2006, ApJ, 645, 534
- Dintrans, B. & Brandenburg, A. 2004, A&A, 421, 775
- Dintrans, B. & Brandenburg, A. 2005, astro-ph/0502138
- Drake, R., Robey, H., Hurricane, O., Zhang, Y., Remington, B., Knauer, J., Glimm, J., Arnett, D., Kane, J., Budil, K., Grove, J. 2002, ApJ, 564, 896
- Dunkerton, T. J., & Fritts, D. C. 1984, Journal of Atmospheric Sciences, 41, 992
- El Eid, M. F. 1995, MNRAS, 275, 983
- Fedorovich, E. E., & Mironov, D. V. 1995, Journal of Atmospheric Sciences, 52, 83
- Fedorovich, E. E., Conzemius, R., & Mironov, D. V. 2004, Journal of Atmospheric Sciences, 61, 281
- Fernando, H. J. S., & Hunt, J. C. R. 1997, Journal of Fluid Mechanics, 347, 197
- Fernando, H. J. S. 1991, Annual Review of Fluid Mechanics, 23, 455
- Ferraro, F. R., Valenti, E., Straniero, O., and Origlia, L., 2006, ApJ, 642, 225
- Fluery, M. Mory, M., Hopfinger, E. & Auchere, D. 1991, J. of Fluid Mech., 223, 165

- Fryer, C. L., Rockefeller, G., & Warren, M. S. 2006, *ApJ*, 643, 292
- Freytag, B., Ludwig, H.-G., & Steffan, M., 1996, *A&A*, 313, 497
- Fryxell, B., et al. 2000, *ApJS*, 131, 273
- Fryxell, B., Müller, E., & Arnett, D. 1989 MPA Preprint 449 (Garching: Max-Planck-Institut für Astrophysik)
- García López, R. J. & Spruit, H. C. 1991, *ApJ*, 377, 268
- Glatzmaier, G. A., & Roberts, P. H., 1995, *Nature*, 377, 203
- Glatzmaier, G. A., 1984, *J. Chem. Phys.*, 55, 461
- Goldreich, P. & Kumar, P. 1990, *ApJ*, 363, 694
- Gottbrath, C, Bailin, J, Meakin, C, Thompson, T, & Charfman, J. J. 1999, *ArXiv Astrophysics e-prints*, arXiv:astro-ph/9912202
- Gough, D. O. 1969, *Journal of Atmospheric Sciences*, 26, 448
- Grevesse, N. & Sauval, A. J., 1998, *Space Science Reviews*, 85, 161
- Grossman, S. A., Narayan, R., & Arnett, D. 1993, *ApJ*, 407, 284
- Hansen, C. J., & Kawaler, S. D., 1994, *Stellar Interiors*, Springer-Verlag
- Heger, A., Langer, N., & Woosley, S. E. 2000, *ApJ*, 528, 368
- Heger, A., Woosley, S. E., & Spruit, H. C. 2005, *ApJ*, 626, 350
- Herant, M., & Benz, W. 1991, *ApJL*, 370, L81
- Herwig, F., Bloeker, T., Schoenberner, D., & El Eid, M. 1997, *A&A*, 324, L81



- Herwig, F., Freytag, B., Hueckstaedt, R. M., & Timmes, F. X. 2006, *ApJ*, 642, 1057
- Hossain, M., & Mullan, D. J. 1993, *ApJ*, 416, 733
- Hoyle, F. 1946, *MNRAS*, 106, 343
- Hurlburt, N. E., Toomre, J., & Massaguer, J. M., *ApJ*, 311, 563
- Iglesias, C. & Rogers, F. J. 1996, *ApJ*, 464, 943
- Itoh, N., Adachi, T., Nakagawa, M., Kohyama, Y., & Munakata, H. 1989, *ApJ*, 339, 354
- Itoh, N., Hayashi, H., Nishikawa, A., & Kohyama, Y. 1996, *ApJS*, 102, 411
- Kantha, L. H., Phillips, O. M., & Azad, R. S. 1977, *Journal of Fluid Mechanics*, 79, 753
- Kato, S 1966, *PASJ*, 18, 374
- Kuhfuss, R. 1986, *A&A*, 160, 116
- Kifonidis, K., Plewa, T., Janka, H.-T., Müller, E. 2003, *A&A*, 408, 621
- Kifonidis, K., Plewa, T., Scheck, L., Janka, H.-T., Müller, E. 2006, *A&A*, 453, 661
- Kim, Y.-C., Fox, P. A., Sofia, S., & Demarque, P. 1995, *ApJ*, 442, 422
- Kim, Y.-C., Fox, P. A., Demarque, P., & Sofia, S. 1996, *ApJ*, 461, 499
- Kippenhahn, R. & Weigert, A. 1990, *Stellar Structure and Evolution*, Springer-Verlag
- Knobloch, E., & Merryfield, W. J. 1992, *ApJ*, 401, 196

- Kuhlen, M., Woosley, S. E., & Glatzmaier, G., *3D Stellar Evolution*, ed., Turcotte, S., Keller, S. C., & Cavallo, R. M., A.S.P. Conf. Series 293
- Kumar, P., & Quataert, E. J., 1997, *ApJ*, 475, L143
- Kumar, P., Talon, S., & Zahn, J.-P. 1999, *ApJ*, 520, 859
- Kunz, R., Fey, M., Jaeger, M., Mayer, A., Hammer, J. W., Staudt, G., Harissopulos, S., & Paradellis, T. 2002, *ApJ*, 567, 643
- Kuranz, C. C., et al. 2005, *Ap&SS*, 298, 9
- Langer, N., Fricke, K. J., & Sugimoto, D. 1983, *A&A*, 126, 207
- Lattanzio, J. C., & Lugaro, M. A. 2005, *Nuclear Physics A*, 758, 477
- Ledoux, P., & Walraven, T. 1958, *Handbuch der Physik*, 51, 353
- Lesaffre, P., Podsiadlowski, P., & Tout, C. A. 2005, *MNRAS*, 356, 131
- Levy, M., & Fernando, H. 2002, *J. of Fluid Mech.*, 467, 19
- Lewellen, D. C., & Lewellen, W. S. 1998, *Journal of Atmospheric Sciences*, 55, 2645
- Lighthill, M. J. 1952, *Royal Society of London Proceedings Series A*, 211, 564
- Lighthill, J. 1978, *Waves in Fluids* (Cambridge: Cambridge University Press)
- Lin, D. J., Bayliss, A., & Taam, R. E. 2006, *ArXiv Astrophysics e-prints*, arXiv:astro-ph/0606207
- Linden, P.F. 1973, *J. of Fluid Mech.*, 49, 611
- Linden, P. F. 1975, *Journal of Fluid Mechanics*, 71, 385

- Lindl, J. D., 1998, *Inertial Confinement Fusion*, Springer-Verlag, Berlin Heidelberg New York.
- Livne, E., 1993, *ApJ*, 406, 17
- Lugaro, M., Davis, A., Gallino, R., Pellin, M., Straniero, O., Käppeler, F. 2003, *ApJ*, 593, 486
- McGrath, J. L., Fernando, H. J. S., & Hunt, J. C. R. 1997, *Journal of Fluid Mechanics*, 347, 235
- Meakin, C. A., & Arnett, D. 2006, *ApJL*, 637, L53
- Merryfield, W. J. 1995, *ApJ*, 444, 318
- Miles, A. 2004, PhD Thesis, U. Maryland
- Montalban, J. 1994, *A&A*, 281, 421
- Mueller, E. 1986, *A&A*, 162, 103
- Murphy, J. W., Burrows, A., & Heger, A. 2004, *ApJ*, 615, 460
- Nomoto, K., Hashimoto, M., Tsujimoto, T., Thielemann, F.-K., Kishimoto, N., Kubo, Y., & Nakasato, N. 1997, *Nuclear Physics A*, 616, 79
- Ober, W. W., El Eid, M. F., & Fricke, K. J. 1982, *NATO ASIC Proc. 90: Supernovae: A Survey of Current Research*, 293
- Odrzywolek, A., Misiaszek, M., & Kutschera, M. 2004, *Acta Physica Polonica B*, 35, 1981
- Orlanski, I. & Bryan, K. 1969, *J. of Geophysical Research*, 74, 6975

- Pasquini, L., Bonifacio, P., Randich, S., Galli, D., & Gratton, R. G. 2004, *A&A*, 426, 651
- Pellacani, C., & Lupini, R. 1975, *Boundary-Layer Meteorology*, 9, 205
- Peltier, W. R. 2003, *Annual Review of Fluid Mechanics*, 35, 135
- Phillips, O. M. 1966, *The Dynamics of the Upper Ocean*, Cambridge University Press. N.Y.
- Pinsonneault, M. H., Kawaler, S. D., Sofia, S., & Demarque, P. 1989, *ApJ*, 338, 424
- Porter, D. & Woodward, P. 1993, *ApJS*, 93, 309
- Porter, D. H., & Woodward, P. R. 2000, *ApJS*, 127, 159
- Porter, D. H., Woodward, P. R., & Jacobs M. L., in *Astrophysical Turbulence and Convection*, Ann. N. Y. Acad. Sci., 898
- Press, W. H. & Rybicki, G. 1981, *ApJ*, 248, 751
- Press, W. H. 1981, *ApJ*, 245, 286
- Rauscher, T., & Thielemann, K.-F., 2000, *Atomic Data Nuclear Data Tables*, 75, 1
- Rempel, M. 2004, *ApJ*, 607, 1046
- Ribas, I. 2006, *Astronomical Society of the Pacific Conference Series*, 349, 55
- Robinson, F. J., Demarque, P., Li, L. H., Sofia, S., Kim, Y.-C., Chan, K. L., & Guenther, D. B. 2003, *MNRAS*, 340, 923
- Robinson, F. J., Demarque, P., Li, L. H., Sofia, S., Kim, Y.-C., Chan, K. L., & Guenther, D. B. 2004, *MNRAS*, 347, 1208

- Robinson, F. J., Demarque, P., Guenther, D. B., Kim, Y.-C., & Chan, K. L. 2005, MNRAS, 362, 1031
- Rogers, T. M., & Glatzmaier, G. A., ApJ, 620, 432
- Rogers, T. M., & Glatzmaier, G. A. 2006, ArXiv Astrophysics e-prints, arXiv:astro-ph/0601668
- Ronchi, C., Iacono, R., Paolucci, P. 1996, J. Comp. Phys., 124, 93
- Ryutov, D., Drake, R., Kane, J., Liang, E., Remington, B., Wood-Vasey, W. 1999, ApJ, 518, 821
- Schatzman, E. 1993, A&A, 279, 431
- Schmitt, J. H. M. M., Rosner, R., & Bohn, H. U. 1984, ApJ, 282, 316
- Schneider, T., Botta, N., Geratz, K. J., & Klein, R. 1999, Journal of Computational Physics, 155, 248
- Schwarzschild, M., Härm, R. 1958, ApJ, 128, 348
- Smagorinsky, J. S., 1963, Mon. Weather Rev., 91, 99
- Sorbjan, Z. 1996, Journal of Atmospheric Sciences, 53, 101
- Spruit, H. C. 1992, A&A, 253, 131
- Spruit, H. C. 2002, A&A, 381, 923
- Staquet, C., & Sommeria, J. 2002, Annual Review of Fluid Mechanics, 34, 559
- Stein, R.F. 1967, Solar Physics, 2, 385
- Stein, R. F., & Nordlund, A. 1989, ApJL, 342, L95

- Stevens, B. 2002, *Quarterly Journal of the Royal Meteorological Society*, 128, 2663
- Stevens, D. E., & Bretherton, C. S. 1999, *Quarterly Journal of the Royal Meteorological Society*, 125, 425
- Stevenson, D. J. 1979, *MNRAS*, 187, 129
- Strang, E. J., & Fernando, H. J. S. 2001, *Journal of Fluid Mechanics*, 428, 349
- Straniero, O., Chieffi, A., Limongi, M., Busso, M., Gallino, R., Arlandini, C. 1997, *ApJ*, 478, 332
- Straniero, O., 2005, *astro-ph/0501405*
- Stull, R. B. 1973, *Journal of Atmospheric Sciences*, 30, 1092
- Stull, R. B. 1976, *Journal of Atmospheric Sciences*, 33, 1260
- Stull, R. B. 1976, *Journal of Atmospheric Sciences*, 33, 1268
- Styne, I., Porter, D. H., Woodward, P. R., Hodson, S. H., Winkler, K. H., 2000, *J. Chem. Phys.* 118, 225
- Talon, S., & Charbonnel, C. 2003, *A&A*, 405, 1025
- Talon, S., & Charbonnel, C., 2005, *A&A*, 440, 981.
- Tennekes, H. 1974, *Journal of Atmospheric Sciences*, 30, 558
- Thielemann, F. K., & Arnett, W. D. 1985, *ApJ*, 295, 604
- Timmes, F. X. & Swesty, F. D. 2000, *ApJS*, 126, 501
- Townsend, A. A. 1966, *Journal of Fluid Mechanics*, 24, 307

- Turner, J. S., 1973, *Buoyancy Effects in Fluids* (Cambridge University, Cambridge, England).
- Turner, J. S. 1980, *Buoyancy Effects in Fluids*, by J. S. Turner, pp. 382. ISBN 0521297265. Cambridge, UK: Cambridge University Press, January 1980
- Umezu, M., Saio, H. 2000, *MNRAS*, 316, 307
- Unno, W., Osaki, Y., Ando, H., Saio, H., & Shibahashi, H. 1989, *Nonradial oscillations of stars*, Tokyo: University of Tokyo Press, 1989, 2nd ed.,
- van den Hoek, L. B., & Groenewegen, M. A. T. 1997, *A&AS*, 123, 305
- Walker, G., et al. 2003, *PASP*, 115, 1023
- Weaver, T. A., Zimmerman, G. B., & Woosley, S. E. 1978, *ApJ*, 225, 1021
- Woosley, S. E., Heger, A., & Weaver, T. A. 2002, *Reviews of Modern Physics*, 74, 1015
- Woosley, S. E., & Weaver, T. A. 1988, *Phys. Rep.*, 163, 79
- Woosley, S. E., & Weaver, T. A. 1995, *ApJS*, 101, 181
- Yi, S. K. 2003, *ApJ*, 582, 202
- Young, P. A. & Arnett, D. 2005, *ApJ*, 618, 908
- Young, P. A., Knierman, K. A., Rigby, J. R., & Arnett, D. 2003, *ApJ*, 595, 1114
- Young, P. A., Meakin, C., Arnett, D., Fryer, C., 2006, *ApJ*, 629, L101
- Young, P. A., Fryer, C., Hungerford, A., Arnett, D., Rockefeller, G., Timmes, F. X., Voit, B., Meakin, C., Eriksen, K. A., 2006, *ApJ*, 640, 891

Zahn, J.-P. 1991, *A&A*, 252, 179

Zingale, M., et al., 2002, *ApJS*, 143, 539